UNIVERSITY OF CALIFORNIA,
IRVINE

When Galaxies Go Quiet: Elucidating the Drivers of Environmental Quenching Across Cosmic Time

DISSERTATION

submitted in partial satisfaction of the requirements
for the degree of

DOCTOR OF PHILOSOPHY

in Physics

by

Devontae Cortez Baxter

Dissertation Committee:
Professor Michael C. Cooper, Chair
Professor James S. Bullock
Professor David P. Kirkby

2023

DEDICATION

To

Ash

I am forever grateful to your unconditional love and undying support throughout this journey

and

Sol Diana

for being a constant reminder of the beauty of this existence.

"This is the real secret of life – to be completely engaged with what you are doing in the here and now. And instead of calling it work, realize it is play."

– Alan Watts

TABLE OF CONTENTS

LIST OF FIGURES

LIST OF TABLES

ACKNOWLEDGMENTS

I would like to begin by expressing my deepest appreciation to my amazing wife, Ashley, who has been a constant source of support and encouragement throughout this journey. For well over a decade, your unwavering belief in me and continual encouragement to pursue my dreams have been a source of deep gratitude. Your selfless acts of love, from preparing nourishing meals to single-handedly taking care of household chores, during the demanding final months, have not gone unnoticed. Thank you for being the most incredible companion that this Doctor could ask for.

A special thanks to my advisor, Mike Cooper. Your support, mentorship, and guidance have played a pivotal role in my overall professional and scientific development. Above all, I appreciate you for always recognizing the humanity in the students that you advise. You, my sir, are a gem, and I am lucky to have had you as an advisor and mentor.

To my beautiful bundle of sunshine, Sol Diana Baxter. You have been the most wonderful addition to our family. It has been an absolute joy to watch you grow and blossom into a curious little scientist and "exploradora". Every day, I eagerly anticipate hearing your infectious laugh and witnessing all the amazing things you have learned. Te agradezco mucho por haberme enseñado lo bonito que es ser padre, especialmente a una niña tan preciosa y curiosa como tú. Te amo con todo mi corazón.

I am immensely grateful to my committee members, James Bullock and David Kirkby, for their invaluable advice, genuine interest, and expert guidance during my time in graduate school. I would like to thank my collaborators Sean Fillingham, Katy Rodriguez-Wimberly, Michael Balogh, Greg Rudnick, Tim Carleton and all of the members of the GOGREEN collaboration that assisted in improving the quality of this work.

I would like to express my appreciation to Dr. Arianna Long and Dr. Katy Rodriguez-Wimberly for providing me with valuable insights on how to thrive as a researcher while simultaneously making a broader impact through leadership and outreach endeavors.

A special thanks to all of the graduate students that have made this an incredibly memorable journey. Some of these people include, but are not limited to, Francisco Mercado, Manuel Pasqual, Alex Lazar, Freida Rivera, Jack Lubin, Kyle Kabarsares, Arianna Long, Katy Rodriguez-Wimberly, Beverly Quan, Stephanie Stawinski, Anna Yu, Matthew Portman, Christian Rodriguez, Andreia Carrillo, Corey Beard, Ivan Martinez, Tami McTaggart, Sarah Maxel, Diego Aleman, Alex Chao, Daniel Jaimes, Andrew Brandel and Scott Locke. Additionally, I would like to extend my heartfelt thanks to all of my friends and family, outside of graduate school, who have supported me throughout this significant chapter in my life. This includes individuals such as Dani Baxter, James Brewer, Ben McEwen, Jonathan Ruiz, José Hernandez, Corey Landers and many others who have played a vital role in my journey.

Additionally, I would like to express my gratitude to Dr. John Wise for providing me with

invaluable guidance and mentorship during my final year at Georgia Tech. His suggestion to apply to the graduate program at UCI has had a profound impact on my personal, academic and professional journey. I am also grateful to Professor Martin Okafor, my first physics teacher, who ignited my passion for the subject and recognized my potential as a future physicist. His dedication and enthusiasm as an instructor has been instrumental in shaping my trajectory.

A very special thanks to all of the teachers and staff at UCI Infant Toddler Center, especially teachers Diana, Kandi, Lizzie, Neli and Sherri. Thank you all for being such passionate instructors and providing Sol with an enriching early childhood education.

Finally, I want to dedicate this work to the memory of my late friend, José Flores-Velázquez. You were a shining light that was extinguished far too soon. Thanks for all of the wonderful memories. Rest in Power.

Much of this dissertation has been published in the Oxford University Press. Chapter 2 was published in the Monthly Notices of the Royal Astronomical Society (MNRAS)503 1636 (Baxter et al., 2021), and chapter 3 in MNRAS 515 5479 (Baxter et al., 2022). Chapter 4 has been submitted to the MNRAS and is under review at the time of this submission with publication expected late 2023. This work was supported in part by NSF grants AST-1815475, AST-1716690, AST-1814159 and AST-1518257. Additional support was provided by NASA through grant AR-14289 from the Space Telescope Science Institute, which is operated by the Association of Universities for Research in Astronomy, Inc., under NASA contract NAS 5-26555. Furthermore, I want to acknowledge support from the Eugene Cota Robles Fellowship and thank the LSSTC Data Science Fellowship Program, which is funded by LSSTC, NSF Cybertraining Grant #1829740, the Brinson Foundation, and the Moore Foundation; participation in the program has greatly benefited this work.

This work has made use of the Sloan Digital Sky Survey (SDSS, http://www.sdss.org/) database. Funding for the SDSS and SDSS-II has been provided by the Alfred P. Sloan Foundation, the Participating Institutions, the National Science Foundation, the U.S. Department of Energy, the National Aeronautics and Space Administration, the Japanese Monbukagakusho, the Max Planck Society, and the Higher Education Funding Council for England. This work has also made use of the Gemini CLuster Astrophysics Spectroscopic Survey (GCLASS) and the Gemini Observations of Galaxies in Rich Early ENvironments (GOGREEN) surveys (http://gogreensurvey.ca). This data was [in part] gathered with the Gemini Observatory, which is operated by the Association of Universities for Research in Astronomy, Inc., under a cooperative agreement with the NSF on behalf of the Gemini partnership. Additionally, this work has made use of observations taken by the CANDELS Multi-Cycle Treasury Program with the NASA/ESA HST, which is operated by the Association of Universities for Research in Astronomy, Inc., under NASA contract NAS5-26555. This research made extensive use of `Astropy`, a community-developed core Python package for Astronomy (Astropy Collaboration et al., 2013, 2018). Additionally, the Python packages `NumPy` (Van Der Walt et al., 2011), `iPython` (Pérez & Granger, 2007), `SciPy` (Virtanen et al., 2020), `Scikit-learn` (Pedregosa et al., 2011), `Keras` (Chollet et al., 2015), and `matplotlib`

(Hunter, 2007) were utilized for our data analysis and presentation. Lastly, this research has made use of NASA's Astrophysics Data System Bibliographic Services.

CURRICULUM VITAE

Devontae Cortez Baxter

EDUCATION

Doctor of Philosophy in Physics **2023**
University of California, Irvine *Irvine, CA*

Master of Science in Physics **2019**
University of California, Irvine *Irvine, CA*

Bachelor of Science in Physics **2017**
Georgia Institute of Technology *Atlanta, GA*

Associate of Science in Physics **2015**
Georgia Perimeter College *Clarkston, GA*

RESEARCH EXPERIENCE

Graduate Student Researcher **2019–2023**
University of California, Irvine *Irvine, California*

Eugene Cota-Robles Fellow **2017–2021**
University of California, Irvine *Irvine, California*

TEACHING EXPERIENCE

Teaching Assistant **2018–2019**
University of California, Irvine *Irvine, CA*

FIRST AUTHOR REFEREED JOURNAL PUBLICATIONS

A Machine Learning Approach to Measuring the Quenched Fraction of Low-Mass Satellites Beyond the Local Group **2021**
MNRAS 503 1636

The GOGREEN Survey: Constraining the Satellite Quenching Time-scale in Massive Clusters at $z \sim 1$ **2022**
MNRAS 515 5479

When the Well Runs Dry: Modeling Environmental Quenching in Massive Clusters at $z \sim 1$ **2023**
MNRAS under review

CONTRIBUTING AUTHOR REFEREED JOURNAL PUBLICATIONS

Reverse Janssen Effect in Narrow Granular Columns **2020**
PRL 124 128002

Sizing from the Smallest scales: the Mass of the Milky Way **2022**
MNRAS 513 4968

GOGREEN: A critical assessment of environmental trends in cosmological hydrodynamical simulations at $z \approx 1$ **2023**
MNRAS 518 4782

ABSTRACT OF THE DISSERTATION

When Galaxies Go Quiet: Elucidating the Drivers of Environmental Quenching Across Cosmic Time

By

Devontae Cortez Baxter

Doctor of Philosophy in Physics

University of California, Irvine, 2023

Professor Michael C. Cooper, Chair

It has long been discovered that environment plays a major role in galaxy evolution, with galaxies in dense regions of the cosmos more likely to have their star formation suppressed or "quenched" relative to their more isolated counterparts. Despite this remarkable discovery, our current understanding of the physical processes responsible for the suppression (or "quenching") of star formation remains woefully incomplete. This is especially true for galaxies that are members of massive galaxy groups and clusters – i.e. "satellite" galaxies – given that our best cosmological models struggle to reproduce key observations, such as the satellite quenched fraction. This dissertation aims to advance our knowledge in the areas of environmental quenching that are poorly understood, focusing on the quenching of low-mass dwarf satellite galaxies and satellite populations at intermediate and high redshifts. Observational studies of low-mass satellite quenching have been limited by their inability to robustly characterize the local environment and star-formation activity of faint systems. This work overcomes these limitations by combining supervised machine learning and statistical background subtraction techniques to constrain the satellite quenched fraction of group populations ($M_{\rm halo} = 10^{13-14}$ $\rm M_{\odot}$) down to a satellite stellar mass limit of $\sim 10^{7}$ $\rm M_{\odot}$. This approach successfully reproduces the established quenched fraction trends at high-masses while finding that ram-pressure stripping – the rapid removal of cold gas from

the interstellar medium of satellites as they move through the hot and dense intra-group or intracluster medium permeating the host halo – is the likely dominant quenching mechanism responsible for shutting down star formation in the low-mass regime. The importance of investigating intermediate and high redshift is that the vast majority of environmental quenching studies are limited to the very local Universe ($z \lesssim 0.1$). This work addresses this shortcoming by combining multi-wavelength spectroscopic observations of massive clusters ($M_{\rm halo} = 10^{14-15}$ M$_\odot$) at $z \gtrsim 1$ with the infall histories of analogs from N-body simulations to model satellite quenching at this poorly studied epoch. The quenching timescales derived from this study indicate that "starvation" – the slow depletion of cold gas in the absence of cosmological accretion after a satellite becomes a member of a more massive host – is the dominant driver of environmental quenching at this epoch. However, this study lends support to the scenario where ram-pressure stripping potentially acts as a secondary quenching mechanism in massive clusters at this epoch. Overall, this work provides valuable insights into the quenching timescales and underlying mechanisms of satellite galaxies in massive clusters at $z \gtrsim 1$, while introducing an impactful methodology that combines supervised machine learning and statistical background subtraction to study the quenching of low-mass satellites beyond the Local Group.

Chapter 1

Introduction

Es más fuerte, si es vieja la verde encina; más bello el sol parece cuando declina; y esto se infiere porque ama uno la vida cuando se muere.

– Rosalía de Castro

Prior to the early 1920s, the prevailing view held that the Milky Way, our home galaxy, represented the entirety of the known Universe. However, this all changed in the year 1923 when the astronomer Edwin Hubble made a monumental discovery that shattered this notion, revealing that the Milky Way is just one of countless galaxies dispersed across the vast expanse of space and time.

In the subsequent years, astronomers observed and studied various properties of galaxies, including their morphology, size, color, and star formation activity. These observations led to the emergence of the field of galaxy formation and evolution as a distinct scientific discipline.

A major milestone in this field was the discovery of strong correlations between various galaxy properties and their surrounding environment. Notably, the morphology-density relation (Dressler, 1980) highlighted the higher prevalence of elliptical galaxies in densely pop-

ulated regions. Additionally, the star formation rate (SFR)-density relation (Dressler, 1984) revealed that local clusters tend to host galaxies with no ongoing star formation, commonly referred to as "quenched" or "quiescent" galaxies.

Advancements in observational techniques and technology, exemplified by large-scale galaxy surveys like the Sloan Digital Sky Survey (SDSS), have played a pivotal role in further revolutionizing our understanding of the interplay between galaxy properties and their environment. These surveys generated vast amounts of data, enabling statistical analyses that unveiled critical trends and patterns in galaxy populations. One important discovery was the revelation that over the past $7 - 10$ Gyr the population of quiescent galaxies has increased by more than a factor of two such that these systems represent the bulk of the stellar mass budget at $z \sim 0$ (Bell et al., 2004; Bundy et al., 2006; Faber et al., 2007).

Despite this remarkable discovery, our current understanding of the physical processes responsible for the suppression (or "quenching") of star formation remains woefully incomplete. This is especially evident for galaxies that are members of dense galaxy groups and clusters, known as "satellite" galaxies, given that current state-of-the-art semi-analytic and cosmological models struggle to reproduce the observed fractions of quenched satellites, especially at low-masses ($M_\star < 10^{10}$ $M_\odot$) and beyond the local Universe ($z > 0.1$) (Kimm et al., 2009; Weinmann et al., 2012; Hirschmann et al., 2014; Donnari et al., 2021). These discrepancies highlight the incomplete nature of our current prescriptions for environmental quenching and underscore the necessity for further investigations into the underlying drivers of this phenomenon.

1.1 The Impact of Environment on Galaxy Quenching

Environmental quenching, analogous to a dying flame, is the process by which the star formation in satellite galaxies is extinguished as a result of the interactions and influences of their surrounding environment. Although our understanding is limited, it is widely acknowledged that environmental quenching involves either i) the depletion of gas without replenishment or ii) the stripping and removal of cold gas, which serves as fuel for star formation. Two prominent candidates for environmental quenching that satisfy these conditions are: i) "starvation" (Larson et al., 1980; Kawata & Mulchaey, 2008), characterized by the *slow* depletion of cold gas in satellite galaxies after they become part of a more massive host, in the absence of cosmological accretion; and ii) "ram-pressure stripping" (RPS Gunn & Gott, 1972; Poggianti et al., 2017), involving the *rapid* removal of cold gas from the interstellar medium of satellites as they traverse the hot and dense intra-group or intracluster medium within the host halo. There are several other mechanisms that may contribute to the quenching of satellite galaxies. These include gravitationally-driven processes such as tidal stripping (Merritt, 1983; Moore et al., 1999; Gnedin, 2003), galaxy mergers (Lavery & Henry, 1988; Makino & Hut, 1997; Gottlöber et al., 2001), and galaxy harassment via high-speed impulsive encounters (Farouki & Shapiro, 1981; Moore et al., 1996, 1998).

1.2 Environmental Quenching Across Cosmic Time

A primary distinguishing feature of the aforementioned environmental quenching mechanisms is the *efficiency* at which they shut down star formation – i.e. the timescale upon which satellite quenching proceeds, denoted $\tau_{\rm quench}$. Several environmental quenching studies, largely limited to the very local Universe ($z < 0.05$), have successfully constrained $\tau_{\rm quench}$ as a function of satellite and host halo mass (e.g. Wetzel et al., 2013; Wheeler et al., 2014;

Fillingham et al., 2015). These investigations provide important constraints on the dominant drivers of environmental quenching, playing a critical role in refining the prescriptions used in hydrodynamical cosmological simulations and semi-analytic models.

This work builds upon the aforementioned studies by employing innovative techniques to enhance our understanding of satellite quenching in two distinct cosmic epochs: the present-day local Universe and a time when the Universe was only half its current age. In order to overcome the limitations imposed by current astronomical datasets, Chapter 2 introduces a novel approach that I developed, utilizing supervised learning and statistical background subtraction, to measure the quiescent fraction of dwarf satellites ($M_\star \sim 10^{6-9}$ $\mathrm{M}_\odot$) beyond the Local Group (< 3 Mpc), which includes galaxies like the Milky Way and Andromeda. Shifting the focus to the cosmic epoch when the Universe was about half its current age, Chapter 3 explores satellite quenching in massive clusters at $z \sim 1$, aiming to constrain the quenching timescale for galaxies in this environment. Lastly, Chapter 4 presents an environmental model that not only determines the timescale of environmental quenching but also identifies the host-centric radius where this process initiates, offering robust constraints on the dominant quenching mechanism operating during this critical epoch. Together, this work contributes to a more comprehensive understanding of satellite quenching and provides valuable insights into the underlying mechanisms shaping galaxy evolution across cosmic time.

Chapter 2

A Supervised Learning Approach for Exploring Low-Mass Satellite Quenching Beyond the Local Group

By seeking and blundering we learn.

– Johann Wolfgang von Goethe

2.1 Introduction

The recent generation of large-scale galaxy surveys have revealed that the population of non-star-forming (i.e. "quiescent" or "quenched") galaxies increased by more than a factor of two in the past $7-10$ Gyr, such that quenched systems, as opposed to their star-forming counterparts, comprise the majority of the stellar mass budget at $z \sim 0$ (Bell et al., 2004; Bundy et al., 2006; Faber et al., 2007). While the growth of the global quenched population

is relatively well measured at late cosmic time, our current understanding of the physical processes responsible for the suppression (or "quenching") of star-formation remains woefully incomplete as evidenced by many models of galaxy formation overestimating the observed satellite quenched fraction (Kimm et al., 2009; Weinmann et al., 2012; Hirschmann et al., 2014). Nevertheless, a wide assortment of physical processes have been put forth to explain how galaxies transition from star forming to quiescent. In general, these processes are split into two distinct categories, namely, internal and environmental quenching. The former, which acts independent of local environment (i.e. on both central and satellite systems), refers to any quenching process that suppresses star formation from within a galaxy. Examples of internal quenching mechanisms include feedback from star formation (Oppenheimer & Davé, 2006; Ceverino & Klypin, 2009) and active galactic nuclei (AGN, Di Matteo et al., 2005; Hopkins et al., 2005; Croton et al., 2006). On the other hand, environmental quenching, which typically applies to low-mass satellites ($\lesssim 10^{10}$ $M_\odot$), refers to a range of quenching mechanisms that suppress star formation due to environmental factors – e.g. ram-pressure stripping (Gunn & Gott, 1972; Abadi et al., 1999), tidal stripping (Merritt, 1983; Moore et al., 1999; Gnedin, 2003), strangulation or starvation (Larson et al., 1980; Kawata & Mulchaey, 2008), and harassment (Moore et al., 1996, 1998). In general, environmental quenching mechanisms suppress star formation by either preventing satellites from accreting gas (e.g. strangulation) or by removing pre-existing gas reservoirs through galaxy-galaxy interactions (i.e. harassment), gravitational tidal forces (e.g. tidal stripping), or interaction with the circumgalactic medium of the host (e.g. ram-pressure stripping).

At $z \sim 0$, galaxy surveys find that satellites, not centrals, comprise the largest fraction of passive systems over a wide range of stellar masses ($\lesssim 10^{10.7}$ $M_\odot$, Wetzel et al. 2013). Furthermore, observations of low-mass ($\lesssim 10^{9}$ $M_\odot$) galaxies in the local Universe have demonstrated that nearly all field galaxies are star forming, signaling that environmental quenching is primarily responsible for suppressing star formation in the low-mass regime (Haines et al., 2008; Geha et al., 2012). Altogether, these observations demonstrate the importance and

ubiquity of satellite quenching at late times and especially low satellite masses. Yet, hydrodynamic and semi-analytic models, which successfully predict the fraction of quiescent centrals, continue to significantly overpredict the relative number of passive satellites, especially at low-masses (Kimm et al. 2009; Hirschmann et al. 2014; Wang et al. 2014, but see also Henriques et al. 2017). This discrepancy between theoretical predictions and observations is driven by a failure to properly model the physical processes responsible for satellite quenching. This lack of agreement between observations and theoretical models further emphasizes that understanding the details of satellite quenching is tantamount to advancing our understanding of galaxy formation.

Our current understanding of satellite quenching at low masses is largely derived from studies of dwarf galaxies ($M_\star \sim 10^6 - 10^8$ M$_\odot$) in the very local Universe, including our own Local Group. First and foremost, a range of observations demonstrate that the vast majority of low-mass satellites are gas-poor and passive, in contrast to their gas-rich, star-forming counterparts in the field (e.g. Grcevich & Putman, 2009; Spekkens et al., 2014; Weisz et al., 2014a,b). Furthermore, studies of the accretion history of these systems using N-body simulations demonstrate that quenching is highly efficient, such that the typical timescale over which quenching occurs is ~ 2 Gyr at $M_\star \lesssim 10^8$ M$_\odot$ (likely driven by an increase in the efficacy of ram-pressure stripping, Fillingham et al. 2015, 2016, 2018; Wetzel et al. 2015; Weisz et al. 2015). On the other hand, studies of the more massive satellites ($M_\star \gtrsim 10^8$ M$_\odot$) in the Local Group and nearby groups/clusters find that these systems have significantly longer quenching timescales ($\gtrsim 5$ Gyr), consistent with starvation acting as the dominant quenching mechanism (De Lucia et al., 2012; Wetzel et al., 2013; Wheeler et al., 2014). Taken together, this implies that a transition in the dominant quenching mechanism occurs at $M_\star \sim 10^8$ M$_\odot$ (at least within Milky Way-like host halos, $M_{\rm halo} \sim 10^{12}$ M$_\odot$, Fillingham et al., 2016; Rodriguez Wimberly et al., 2019a).

A major step towards increasing our understanding of satellite quenching involves determin-

ing if the aforementioned results extend beyond the Local Group. Is a similar increase in the quenched fraction observed at low masses outside of the Local Group (and/or in more massive host halos), indicating a corresponding increase in the efficiency of environmental (or satellite) quenching at this mass range? Unfortunately, the current generation of spectroscopic surveys lack the necessary combination of depth, area, and/or completeness to reliably probe this mass regime. For example, at the magnitude limit of the main spectroscopic survey, the Sloan Digital Sky Survey (SDSS, York et al., 2000) can only probe galaxies with stellar masses less than 10^8 $M_\odot$ at $z < 0.01$. While more recent surveys push fainter, including the Galaxy and Mass Assembly (GAMA) (GAMA, Driver et al., 2009, 2011) survey, the corresponding area of sky mapped is significantly smaller, again limiting the number of nearby hosts around which we can study their satellites. In contrast to spectroscopic data sets, wide and deep imaging programs are able to probe both star-forming and passive galaxies down to stellar masses of $\sim 10^7$ $M_\odot$ at $z \lesssim 0.1$, covering significant areas on the sky.

Herein, we present a method for measuring the satellite quenched fraction down to $M_\star \sim 10^7$ $M_\odot$ by applying machine learning and statistical background subtraction techniques to wide and deep photometric data sets, pushing beyond the limits of current spectroscopic samples. In §2.2, we describe the spectroscopic and photometric data sets utilized in our analysis. In §2.3, we discuss the training, testing, and performance of our neural network classifier (NNC) as well as our use of the trained model to classify galaxies in our photometric sample as star forming or quenched. In §2.4, we describe our statistical background subtraction technique and use it to measure the satellite quenched fraction around nearby groups. Lastly, in §2.5, we discuss and summarize our results. When necessary, we adopt a flat ΛCDM cosmology with $H_0 = 70$ km s^{-1} Mpc^{-1} and $\Omega_m = 0.3$. All magnitudes are on the AB system (Oke & Gunn, 1983).

2.2 Data

2.2.1 Photometric Sample

Our analysis utilizes the co-added images and photometry from the Sloan Digital Sky Survey, focusing on the deeper Stripe 82 data set (S82, Annis et al., 2014; Bundy et al., 2015). Stripe 82 is centered on the Celestial Equator and is comprised of an area of $\sim$ 300 deg^2 that spans between $-50^\circ < \alpha < 60^\circ$ and $-1.25^\circ < \delta < +1.25^\circ$. The co-added images in S82 reach a depth ~ 2 magnitudes deeper in *ugriz* relative to the SDSS single-pass data. Overall, the wide area and impressive depth ($r \sim 22.4$, 95% complete for galaxies) of Stripe 82 make it well-suited for studying the properties of low-mass galaxies in the local Universe. For the purpose of our analysis, we limit the S82 sample to only include galaxies (defined using the SDSS `TYPE` parameter) with $13 < r < 21.5$. This apparent r-band magnitude cut is applied to ensure that galaxies in our sample are below the SDSS saturation limit and above the 95% completeness limit for galaxies in the *gri* passbands.

We exclude the shallower and less complete u and z bands throughout our analysis. Furthermore, as discussed in Bundy et al. (2015), the `TYPE`-based galaxy classification is contaminated with a non-negligible fraction of stars ($\sim 10\%$), which is attributed to PSF characterization issues in the co-added images. Based on visual inspections, we find that the fraction of stars misclassified as galaxies is higher and more pronounced at brighter magnitudes. To eliminate stars from the photometric sample, we remove sources at $15 < r < 18$ that are classified as stars in the corresponding single-pass SDSS images. At the very brightest magnitudes ($r < 15$), where number counts are lower, we remove stars based on a visual inspection of the single-pass SDSS images. Combined, these two procedures remove $\sim 6\%$ of sources at $r < 18$ from our sample, such that our final catalog includes 1,293,392 galaxies with non-extinction-corrected *gri* photometry in S82. Accounting for Galactic extinction does not change our qualitative results, in part due to the low extinction in the S82 field

(Schlegel et al., 1998).

2.2.2 Spectroscopic Training Set

To train our classification scheme, which aims to identify galaxies as star forming or quenched, we use spectroscopic data products from the Max Planck Institute for Astrophysics and Johns Hopkins University DR7 catalog (MPA-JHU, Kauffmann et al., 2003; Brinchmann et al., 2004) along with photometry from SDSS Data Release 7 (Aihara et al., 2011). The MPA-JHU catalog is a value-added data set derived from the spectroscopic SDSS DR7, containing stellar mass and star formation rate (SFR) estimates for nearly a million galaxies up to $z \sim 0.3$. When available, the SFRs are derived using the extinction-corrected Hα emission line luminosities. For galaxies that lack emission lines, the SFRs are estimated using a relationship between SFR and the 4000Å-break index (D_{4000}, Bruzual A., 1983; Hamilton, 1985; Brinchmann et al., 2004). Likewise, the stellar masses are computed using model fits to the broad-band *ugriz* photometry (Kauffmann et al., 2003).

We match galaxies in the MPA-JHU and SDSS DR7 catalogs using their unique MJD, plate ID, and fiber ID to construct a cross-matched catalog that includes both photometric and spectroscopic galaxy properties. These properties include *gri* model magnitudes, specific star-formation rates (sSFR; SFR divided by stellar mass), redshifts, and stellar masses. Furthermore, we limit our cross-matched catalog to only include galaxies in which CLEAN = 1, RELIABLE $\neq$ 0. The former is a photometric flag that removes sources suffering from saturation, deblending, and/or interpolation issues. The latter is a spectroscopic flag that omits galaxies with unreliable line profiles and physical parameters. Overall, these cuts remove roughly 3% of galaxies from the original MPA-JHU catalog. Finally, we limit our sample to only include galaxies at $z < 0.1$ and $M_\star > 10^{6.5}$ $M_\odot$, with measured specific star formation rates. Overall, our final sample includes $\sim$ 240,000 galaxies, with a median

redshift of 0.07, median stellar mass of 2.7×10^{10} $M_\odot$, and median r-band magnitude of 17.

2.2.3 Host Sample

Our spectroscopically-confirmed host sample is selected from the group catalog of Yang et al. (2007). We select groups within the Stripe 82 footprint at $z < 0.1$ and $10^{13} < M_{\rm halo}\, h^{-1}\, M_\odot < 10^{14}$, excluding groups that are located within 0.5 degrees of the edges of the Stripe 82 field. Our final sample consists of 110 hosts, with a median redshift of 0.077 and a median halo mass of 1.6×10^{13} $M_\odot$. The central galaxies in these groups have a median stellar mass of 1.3×10^{11} $M_\odot$.

2.3 Neural Network Classifier

2.3.1 Feature Selection and Pre-Processing

The first step in constructing our training set for supervised machine learning involves selecting the appropriate features that will enable our machine learning model to accurately classify galaxies as either star forming or quenched. Moreover, we can only include photometric features since we ultimately seek to apply our neural network classifier (NNC) to galaxies without spectra. To that end, we construct a heatmap to visualize the degree of correlation, as measured by the Pearson correlation coefficient, between the specific star formation rate of the MPA-JHU galaxies and their photometric properties. As shown in Figure 2.1, we find a relatively strong negative correlation between the optical colors of the galaxies and their specific star formation rates, which implies that optically blue (red) galaxies tend to have higher (lower) specific star formation rates. With this correlation in mind, we construct our training set using only the $g-r$, $r-i$, and $g-i$ observed colors as features. The inclusion of

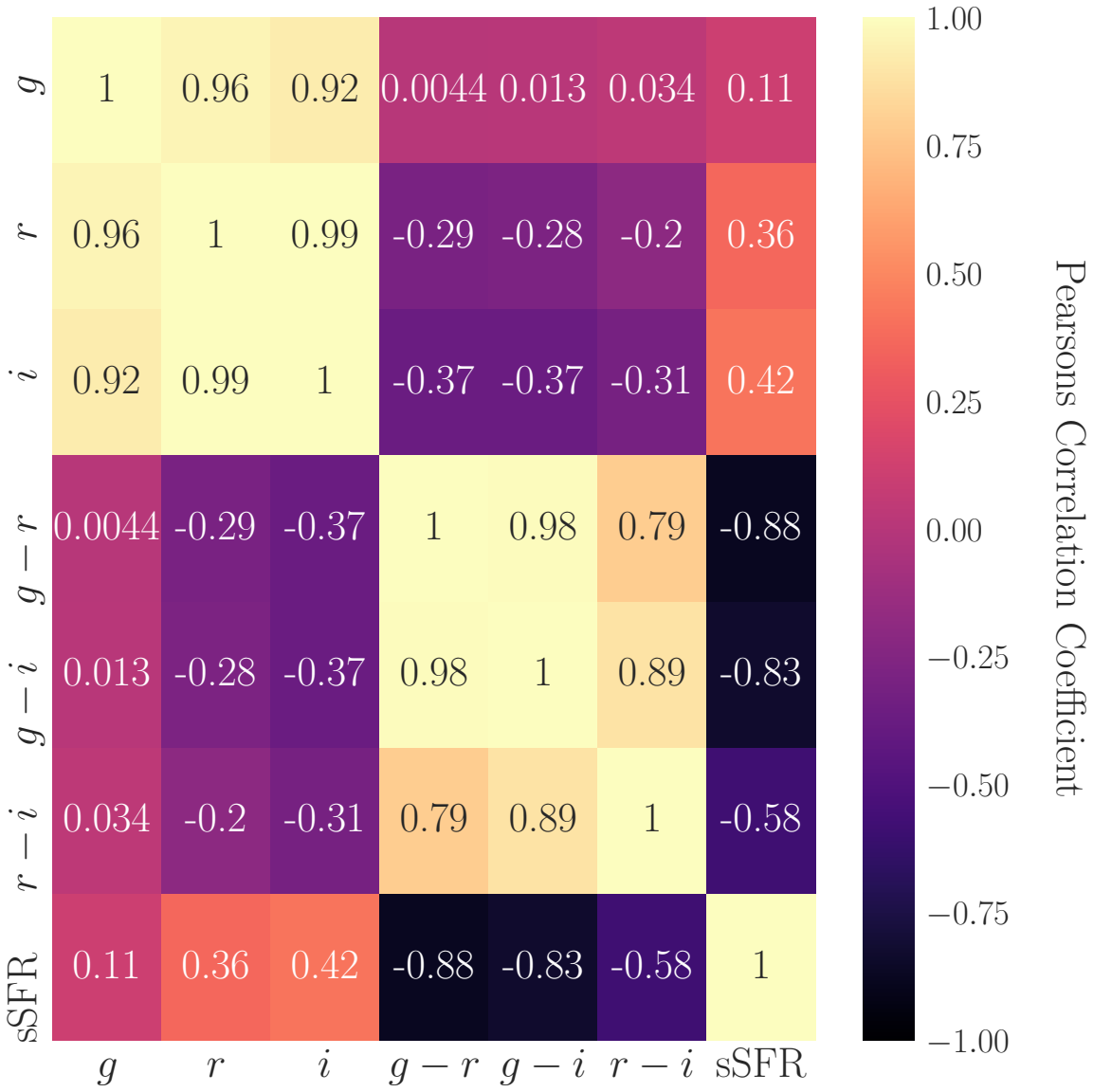

Figure 2.1: A heatmap displaying the correlation between observed colors, apparent magnitudes, and specific star-formation rates for galaxies in our spectroscopic training set. In general, supervised neural network classifiers rely heavily on an existing correlation between input features and target variables (i.e. quenched or star-forming label). For our sample, we detect a relatively strong correlation between observed color and sSFR.

magnitude information (i.e. apparent *gri* magnitudes) has a negligible effect on the resulting classifications, and as such was not utilized in the final configuration.

The second important step in constructing our training set for supervised machine learning involves systematically labeling galaxies as either star forming or quenched. We achieve this by taking advantage of the strong bimodality in sSFR-$M_\star$ space, which for our MPA-JHU sample is illustrated if Figure 2.2. In particular, we adopt a cut of sSFR = 10^{-11} yr^{-1} as our quenching threshold, such that galaxies above (below) this threshold are labeled as star forming (quenched). This results in a balanced training set where 49% (51%) of galaxies are classified as quenched (star forming). This is important because imbalanced training sets can result in uninformative models that naively overpredict the majority class and underpredict the minority class. Furthermore, we standardize the features of our training set to have a mean of zero and standard deviation of one according to $X_{\rm st} = (X - \mu)/\sigma$, where X, μ, and σ are the input feature, mean, and standard deviation of the sample, respectively. This pre-processing procedure is implemented to optimize the performance and stability of the neural network classifier, which assumes that the inputs are standardized.

Lastly, to construct our validation set, we remove 6600 out of the $\sim$ 240,000 galaxies in our training set. The validation set is composed of a subset of those galaxies cross-matched between the MPA-JHU and the S82 photometric catalogs using a search radius of $1''$. We omit these galaxies from the training and testing process, so that they can ultimately be used to evaluate the performance of the resultant NNC.

2.3.2 Supervised Neural Network Classifier

The supervised neural network classifier is a machine learning model that is trained using labeled observations in order to learn a mapping function between input features and output targets. The utility of these models is that once they are trained they can be readily

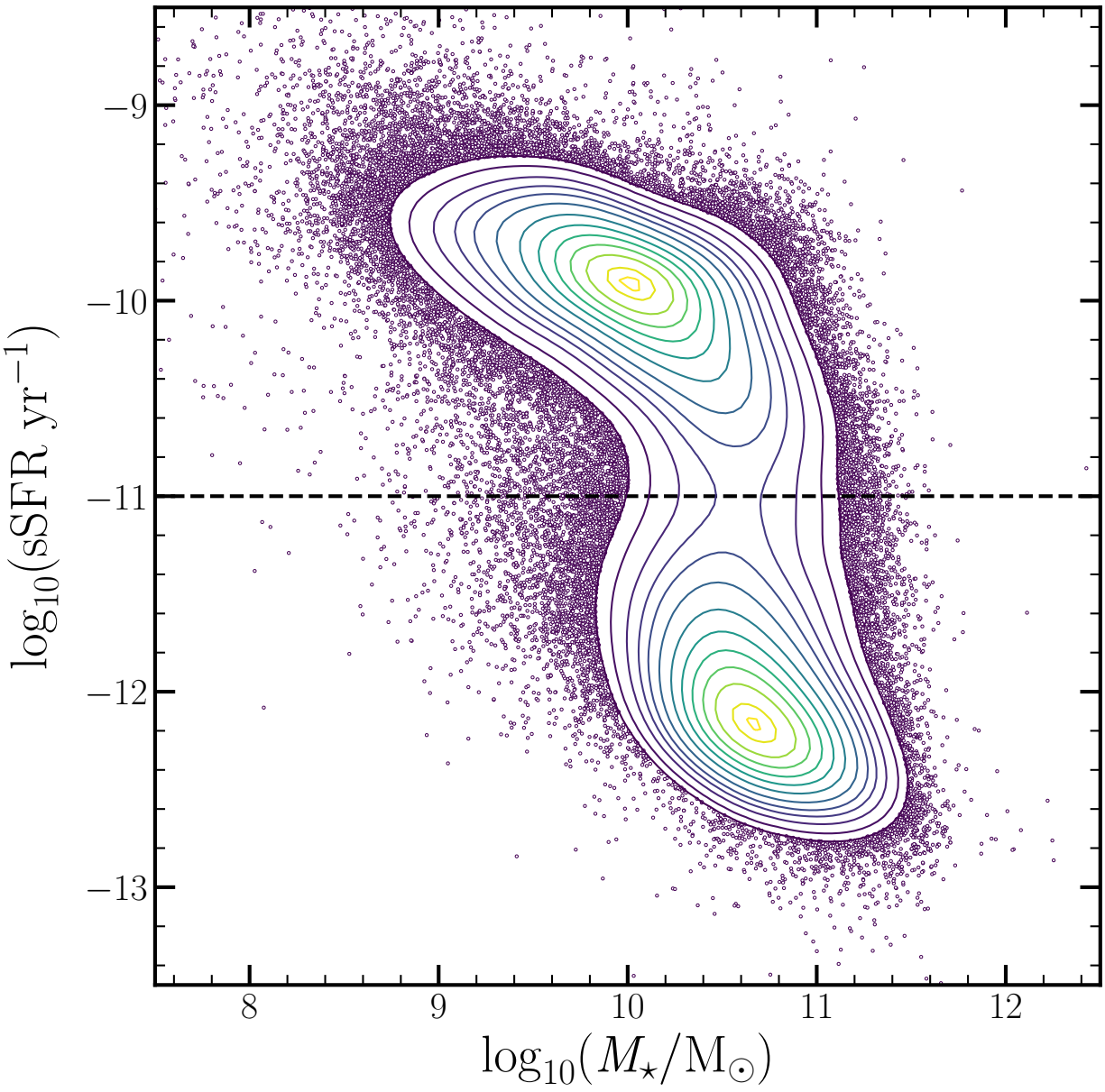

Figure 2.2: Specific star formation rate versus stellar mass for galaxies in our spectroscopic training set. The contours highlight the star-forming and quenched galaxy population within our sample. We divide the galaxy sample at sSFR = 10^{-11} yr^{-1}, such that galaxies above this threshold are labeled as star forming and galaxies below this threshold are labeled as quenched.

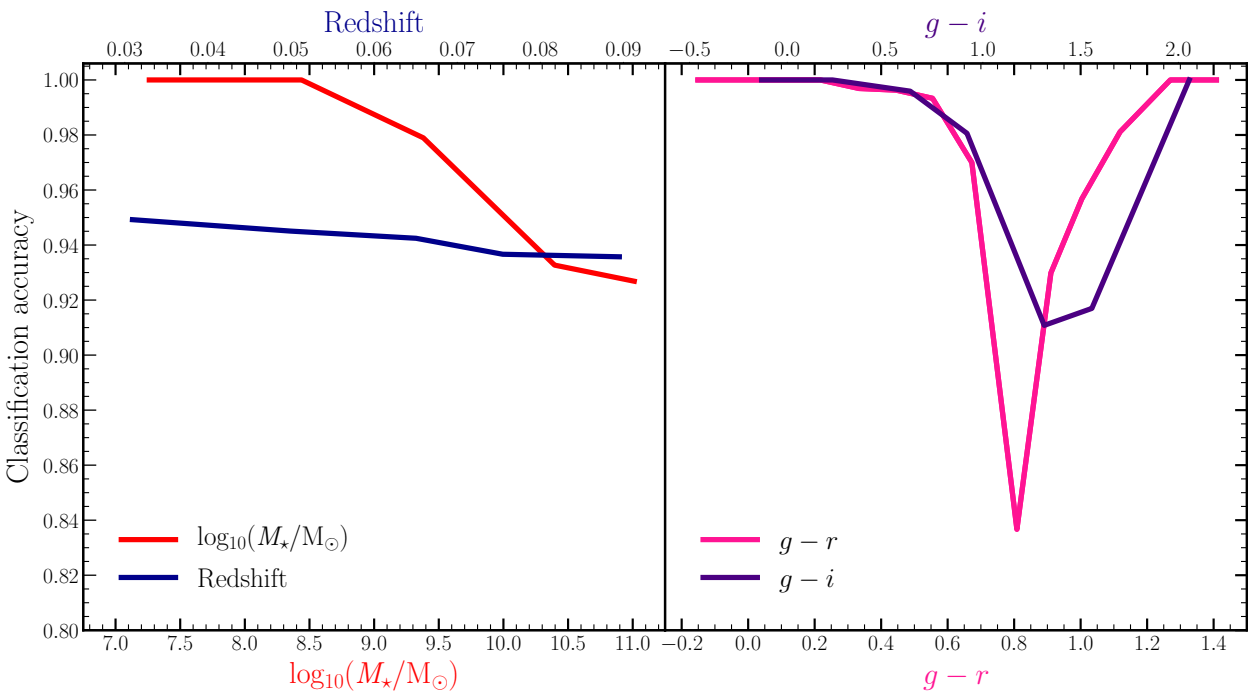

Figure 2.3: Classification accuracy in the validation set as a function of redshift and stellar mass (*left*) along with observed $g-r$ and $g-i$ color (*right*). The accuracy of the NNC is largely independent of host halo redshift and weakly dependent on stellar mass, with high-mass galaxies more likely to be incorrectly classified. Despite the training set being largely composed of high-mass galaxies ($\sim 90\%$ of the training set has $M_\star > 10^{9.5}$ $\mathrm{M}_\odot$), we find that the overall classification accuracy as well as our primary satellite quenched results remain qualitatively unchanged when high-mass systems are omitted from the training set. As expected, the NNC is less reliable at classifying galaxies at intermediate colors (i.e. in the "green valley" of the color bimodality) precisely due to the binary nature of the classification scheme.

used to classify unlabeled observations. Moreover, neural network classifiers are constructed using a variety of hyperparameters that influence the overall performance of the machine learning model. The optimal hyperparameters for our NNC are obtained using a K-fold cross-validation grid search. The names and values of these hyperparameters are as follows: (i) the number of hidden layers is two; (ii) the number of nodes in the first and second hidden layer are 8 and 4, respectively; (iii) the batch size is 64; (iv) the number of epochs is 10; (v) the dropout is 20%. As is standard for binary classification, we use the rectified linear unit (ReLU) activation function for the input and hidden layers, while the sigmoid activation function is used for the output layer. Our model is compiled using a binary cross-entropy loss function and stochastic gradient descent with a learning rate of 0.01. Lastly, we use a stratified K-fold cross validation procedure with k=5 to determine the average accuracy and logarithmic loss of our model.

2.3.3 Performance of Neural Network Classifier

The K-fold cross validation yields an average classification accuracy of 0.94 and logarithmic loss of 0.17. Here, the accuracy measures the fraction of galaxies that are correctly classified during the training/testing process, while the logarithmic loss measures the uncertainty of the predictions made by the NNC. Therefore, the high average classification accuracy and low logarithmic loss suggest that our NNC returns both accurate and precise classifications. Another diagnostic for determining the reliability of the NNC involves applying the trained model to labeled data that was not utilized during the training or testing process. In our case, we use our validation set that is composed of a subset of the galaxies cross-matched between our spectroscopic training set and the S82 photometric sample. Upon applying the NNC to our validation set, we find that 93% of galaxies in the validation set are correctly classified as quenched, and 95% of star forming galaxies in the validation set are correctly classified as star forming. Moreover, we find that the true quenched fraction for the validation set

is reproduced by the NNC with an average percent error of $\sim 2\%$, largely independent of stellar mass.

In addition to classifying the galaxies in the validation set, the NNC also provides a classification probability (CP) between 0 and 1 for each prediction such that the CP equals 0 (1) when the model is 100 percent certain that a given galaxy is quenched (star forming). With this information, we define the classification confidence to be equal to the classification probability when CP > 0.5 and equal to $1 - \mathrm{CP}$ when CP < 0.5. The mean and median classification confidence are 0.927 and 0.98, respectively. Overall, these results provide further confidence in the reliability and accuracy of the predictions made by the neural network classifier.

Using the validation set, we also explore how the classification accuracy varies with galaxy properties. As shown in Figure 2.3, we find that the classification accuracy remains relatively constant across our specified redshift range, such that host halos at slightly lower redshift are not biased relative to their higher-z counterparts within the sample. We do find, however, a modest correlation between classification accuracy and stellar mass, such that the NNC achieves higher levels of accuracy when classifying lower-mass galaxies ($M_\star \lesssim 10^9$ $\mathrm{M}_\odot$). While the spectroscopic training set is dominated by more massive galaxies ($\sim 90\%$ of the spectroscopic training set has $M_\star > 10^{9.5}$ $\mathrm{M}_\odot$), the classification accuracy – and our primary results regarding the satellite quenched fraction – are qualitatively unchanged when limiting the spectroscopic training set to systems with $10^{6.5}$ $\mathrm{M}_\odot < M_\star < 10^{9.5}$ $\mathrm{M}_\odot$.

As suggested in Figure 2.1, $g-r$ and $g-i$ color are the most informative features with respect to predicting whether a galaxy is star forming or quenched. In Figure 2.3, we explore the relationship between the classification accuracy and these two features. As expected, the classification accuracy is highest for very blue and red galaxies, with a modest decrease for galaxies residing in the green valley. This is in part due to the binary nature of our classification scheme (i.e. the lack of a transitory phase between star forming and quenched)

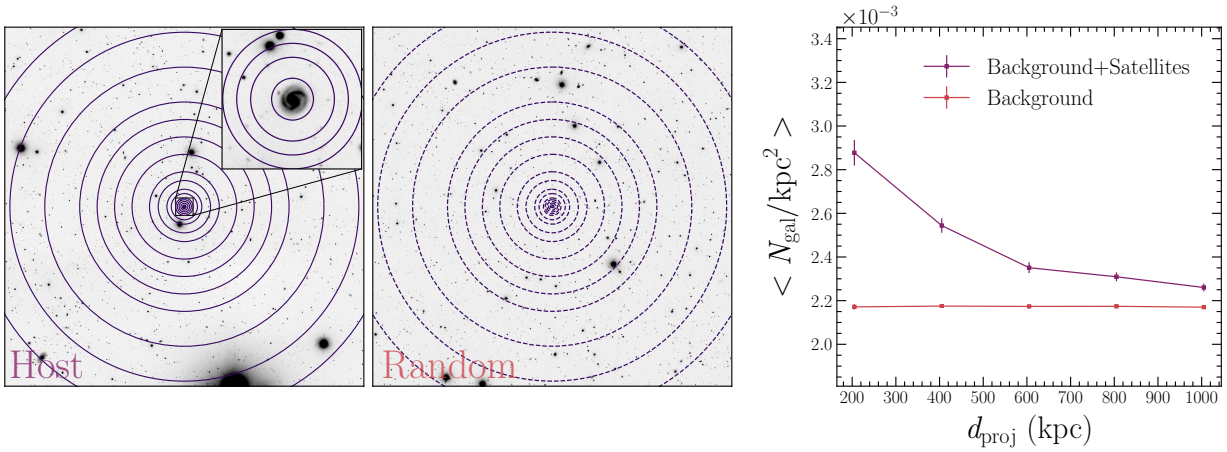

Figure 2.4: An illustration of our background subtraction technique, in which we measure the radial number density of galaxies around our host galaxies (*left*) and in randomly-selected background fields (*middle*). Using the photometric sample, we compute the mean number density profile as a function of projected radial distance, averaged over our sample of hosts and 6×10^4 background fields (*right*). The error bars for both radial profiles correspond to 1-σ Poisson errors in the measured surface density of galaxies.

along with the overlap between dusty star-forming galaxies and quiescent systems in rest-frame optical color (e.g. Yan et al., 2006; Maller et al., 2009; Williams et al., 2009).

2.3.4 Classification of Galaxies in Stripe 82

Using the hyperparameters discussed in §2.3.1, we train our NNC on the entirety of the spectroscopic training set (§2.2.2). Next, we standardize the apparent $g-r$, $g-i$, and $r-i$ colors of the galaxies in our S82 photometric sample to have a mean of zero and standard deviation of one using the same procedure outlined in §2.3.1. Classifying our photometric sample using the trained NNC, we find that 66% of the galaxies in our photometric sample are classified as quenched while 34% are classified as star forming. We recognize that the fraction of passive galaxies in our photometric sample is biased high due to the inevitable inclusion of high-z galaxies. Many of these high-z sources have red apparent colors, and are more likely to be classified as quenched. Ultimately, the success of our approach relies on correctly classifying the low-z sources (i.e. the satellites of our targeted group sample). With

that objective, the next step in our analysis involves combining the classification results with a statistical background subtraction technique to ultimately determine the satellite quenched fraction of our low-z host sample.

2.4 Analysis of the S82 Sample

2.4.1 Statistical Background Subtraction

While deep imaging allows the satellite population around nearby hosts to be detected and our NNC is able to robustly classify sources as star forming or quenched, identifying the true satellites amongst the sea of background sources remains a challenge. This is primarily due to the lack of highly-complete line-of-sight velocity information for our photometric sample, which is required to cleanly determine if a particular source is truly a satellite of a given host. However, instead of identifying properties of individual satellites, we employ a statistically-driven background subtraction technique that enables us to robustly measure the average properties of the satellite population. Figure 2.4 illustrates our methodology, by which we compare the radial distribution of galaxies around nearby hosts to that measured in random positions on the sky. By subtracting the random background, we are able to measure the average properties (e.g. radial profile, rest-frame color distribution, quenched fraction) of the underlying satellite population.

This statistical approach has proven effective in previous studies of satellites at intermediate redshift (Tal et al., 2013; Kawinwanichakij et al., 2014; Nierenberg et al., 2011, 2012). In general, the background subtraction procedure utilized in these studies involves measuring the radial distribution of galaxies around spectroscopically-confirmed hosts and subtracting the contribution from the background/foreground galaxies. For our analysis, we utilize the 110 centrals from the Yang et al. (2007) group catalog that overlap with the S82 footprint as

our sample of spectroscopically-confirmed host galaxies. As stated in §2.2.3, our host sample is situated at $z < 0.1$ and have halo masses between 10^{13} and 10^{14} h^{-1} $M_{\odot}$.

Our technique for estimating the contribution from background galaxies involves measuring the radial distribution of galaxies at random positions within the S82 footprint. In particular, we generate 10^6 random positions within Stripe 82, assigning each a corresponding redshift between $0.02 < z < 0.1$ as randomly drawn from a uniform distribution. As was done for the host sample, the random positions are also required to be less than 0.5 degrees from the edges of the S82 field. We have also considered requiring the random points to be sufficiently far away from the spectroscopic hosts (e.g. $d_{\rm proj} > 1 - 2$ Mpc). However, we ultimately omitted this constraint since both scenarios return qualitatively similar results.

We partition our hosts and random positions into six evenly-spaced redshift bins between $0.02 < z < 0.1$. For a given redshift bin, we count the number of quenched and star-forming galaxies in annuli centered on the hosts in bins of r-band magnitude. This procedure is repeated at the location of the background pointings, for which we count the number of quenched and star-forming galaxies in bins of r-band magnitude within annuli centered on 100 random positions. Specifically, the photometric sample is partitioned into seven r-band magnitude bins between $13 < r < 21.5$ and the galaxies are counted in five annuli between 15 and 1000 kpc. For each r-band magnitude and redshift combination, we calculate the average number of quenched and star-forming galaxies per annuli for both the background and the spectroscopically-confirmed centrals. Moreover, for each individual host/random position, we calculate the 1-σ Poisson error associated with our measurement and propagate this error in the calculation of the average number of galaxies per annuli. Increasing the number of random pointings used to determine the background (i.e. > 100) yields no significant change in our results.

The galaxies are counted in the manner outlined above because it allows us to robustly estimate stellar masses for our statistical satellite population by capitalizing on the strong

correlation between apparent r-band magnitude and stellar mass at fixed redshift. To determine this mapping from r and z to stellar mass, we fit the following relation to galaxies in the MPA-JHU catalog

$$M_{\star}(r, z) = \gamma * r + b(z) \ , \tag{2.1}$$

where γ and $b(z)$ correspond to the slope and y-intercept of the fit in a given redshift bin. In particular, we fit this relation in redshift bins (with typical width of $\Delta z = 0.005$), such that the statistically-inferred galaxy counts as a function of r-band magnitude (following background subtraction) can be mapped to stellar mass based on the redshift of the host system. In Figure 2.5, we compare the stellar masses estimated using our best-fit parameters for Equation 2.1 to the corresponding stellar masses from the MPA-JHU catalog, which are based on fitting the multi-band photometry to model spectral energy distributions. Our stellar mass estimates, inferred solely from the observed r-band magnitude, are relatively accurate with a median difference of -0.030 dex and a 1σ scatter of 0.22 dex. There is a slight bias towards our method under- and over-predicting the masses of high-mass and low-mass galaxies, respectively. Not surprisingly, the fits to Equation 2.1 are best at intermediate stellar masses, where the spectroscopic training set is more abundant. Tuning our fits to better reproduce the stellar masses of low-mass systems does not yield a significant change in our results, with our measurements of the satellite quenched fraction computed in bins of stellar mass that exceed the typical measurement uncertainty.

Altogether, the statistical background procedure provides us with a measure of the average number of quenched and star-forming galaxies as a function of projected distance and stellar mass at the location of both the spectroscopically-confirmed host galaxies and the random background positions. With these galaxy counts and classifications, we compute the average number of quenched and star-forming satellites as a function of stellar mass and projected

distance according to

$$\bar{N}_{\rm sats}(d_{\rm proj}, M_\star) = \sum(\bar{N}_{\rm back+sats} - \bar{N}_{\rm back}) \ , \tag{2.2}$$

where $\bar{N}_{\rm back+sats}$ and $\bar{N}_{\rm back}$ are the average number of galaxies measured in annuli centered on the spectroscopically-confirmed centrals and random positions, respectively.

In Figure 2.6, we show the resulting average number of satellites as a function of stellar mass and projected host-centric distance. We adopt 400 kpc as the outer extent of our groups (roughly R_{200}) based upon a comparison to similar halos in the IllustrisTNG project (Nelson et al., 2018, 2019; Naiman et al., 2018a; Marinacci et al., 2018; Springel et al., 2018; Pillepich et al., 2018). For host halos at $z = 0$ and 10^{13} h^{-1} M$_\odot$ $< M_{200} <$ 10^{14} h^{-1} M$_\odot$ within the TNG300 simulation, a sample of > 2000 halos with a median mass of $M_{200} \sim 1.85 \times 10^{13}$ h^{-1} M$_\odot$, the median R_{200} is 430 h^{-1} kpc with a 1σ scatter of 97 h^{-1} kpc. Given that our measurements are made in projection, we limit our selection of the satellite population to projected distances of < 400 kpc. While this excludes a subset of satellites at host-centric distances of 400 kpc $< R < R_{200}$, it also reduces contamination from objects in the surrounding infall regions ($R \sim$ 1-2 R_{200}). As discussed in §2.4.2, our results are qualitatively unchanged when including satellites out to projected distances of 600 kpc or 800 kpc.

Selecting satellites within 400 kpc, we find excellent agreement between our inferred satellite stellar mass function and that measured for the IllustrisTNG hosts. As shown in Figure 2.7, our integrated satellite counts are very tightly bracketed by the corresponding predicted counts in the TNG100 and TNG300 simulations, where we select satellites at projected distances of < 400 kpc for hosts with $M_{200} = 10^{13-14}$ h^{-1} M$_\odot$. In addition, we compare to the observed satellite mass function from Yang et al. (2008, 2009), based on a sample of spectroscopically-confirmed satellites in $\sim$ 300,000 low-z groups (see also Vázquez-Mata

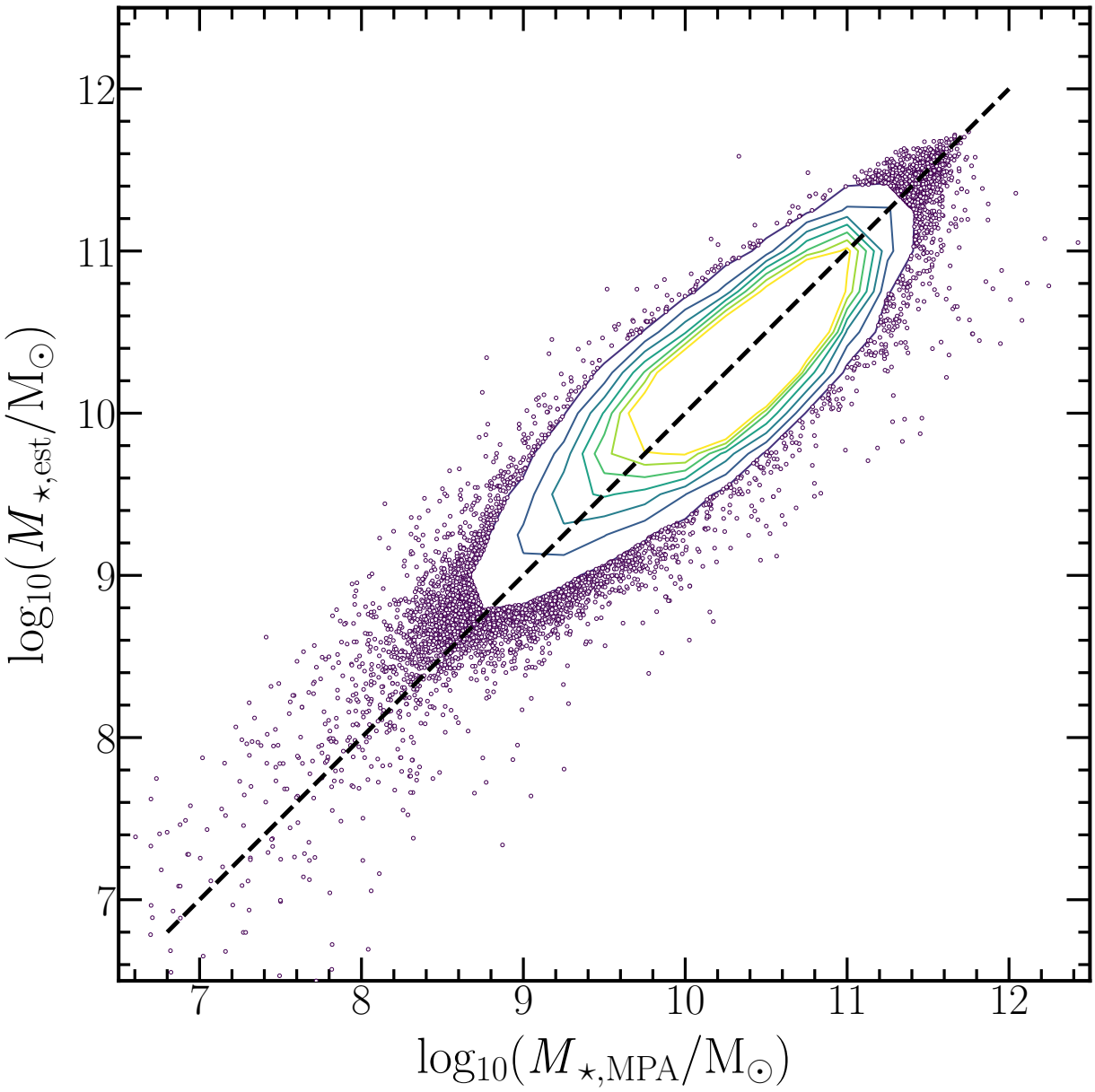

Figure 2.5: Comparison between our estimated stellar masses and those provided by the MPA-JHU catalog. Our stellar mass estimator, which we infer by fitting galaxies in the MPA-JHU catalog using Equation 2.1, provides robust mass measurements in the absence of multi-band photometry. In comparison to the MPA-JHU measurements, the median stellar mass difference is -0.030 dex with a standard deviation of 0.22 dex.

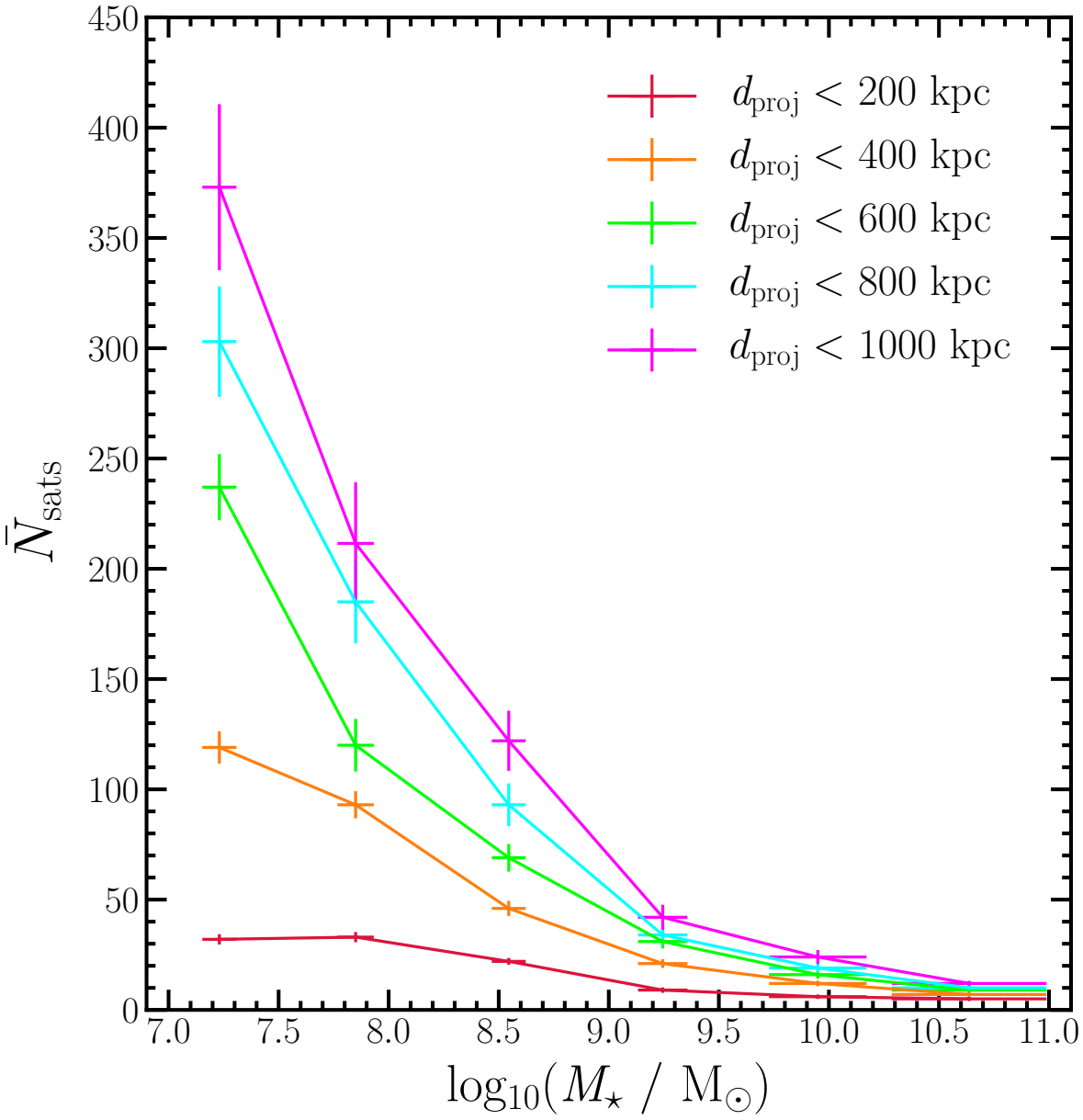

Figure 2.6: The average number of satellites as a function of stellar mass in projected distance bins. The vertical error bars gives the standard deviation in the distribution of the number of satellites after repeating the background subtraction procedure 100 times, whereas the horizontal error bars represent the standard deviation within the stellar mass bin. For our analysis, we limit our satellite population to systems at $d_{\rm proj} < 400$ kpc.

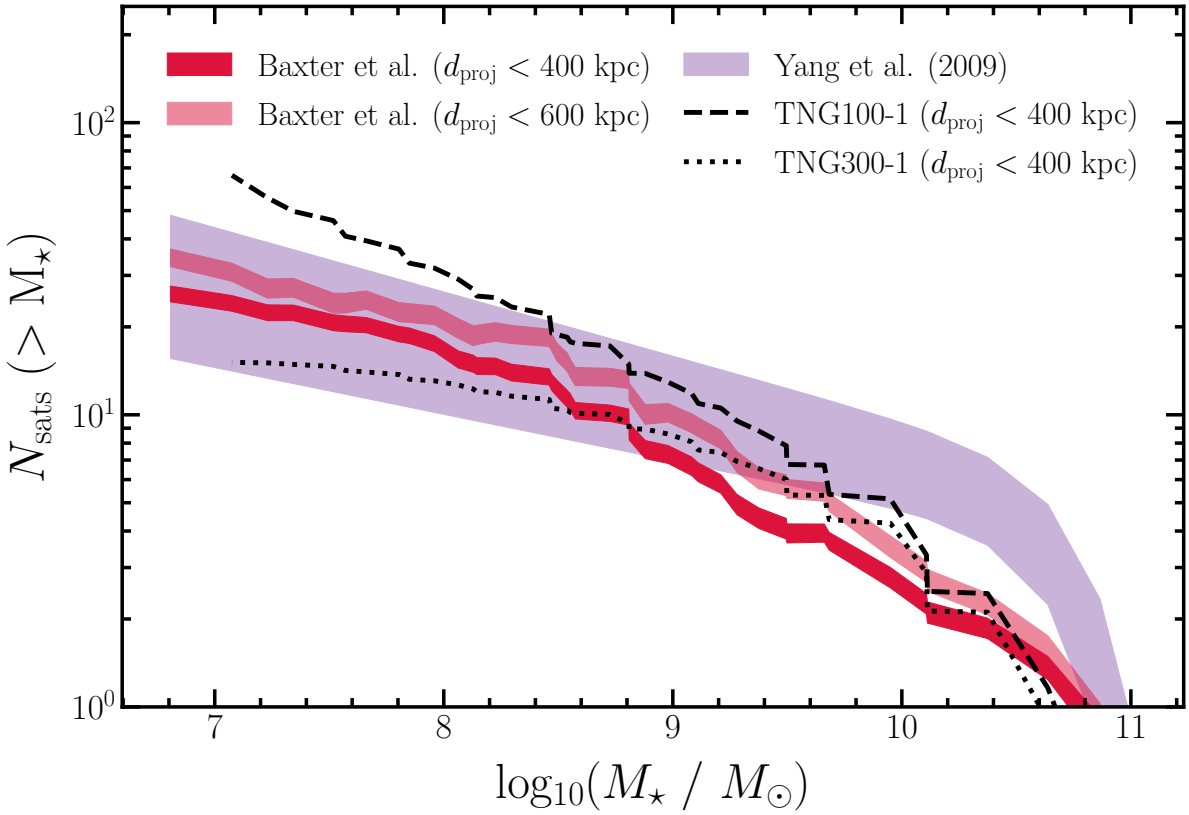

Figure 2.7: The cumulative satellite stellar mass function based on our statistical background subtraction technique in comparison to that from spectroscopic observations and simulations. The dark and light crimson bands show our satellite counts (per group) at $R < 400$ kpc and $R < 600$ kpc, respectively. The purple band corresponds to the satellite stellar mass function for groups with $M_{\rm halo} = 10^{13.2-13.8}\ h^{-1}\ {\rm M}_\odot$ from Yang et al. (2009), while the black dashed and dotted lines denote the satellite counts for host halos with $M_{200} = 10^{13-14}\ h^{-1}\ {\rm M}_\odot$ and satellites at projected distances of < 400 kpc within the TNG100 and TNG300 simulations, respectively. We find excellent agreement between our inferred satellite counts and those based on simulations and shallower spectroscopic samples.

et al., 2020). Overall, our measured satellite mass function is in remarkably good agreement, especially at low masses (or faint magnitudes). While our background-subtraction technique is unable to identify individual satellite galaxies, it is quite robust at indirectly identifying the satellite population, such that its properties may be characterized.

2.4.2 Measuring the Satellite Quenched Fraction

As a benchmark for comparison, we measure the quenched fraction as a function of satellite stellar mass for the spectroscopically-confirmed satellites in the Yang et al. (2007) group catalog. We limit our sample of host halos to those with $10^{13}\ h^{-1}\ \mathrm{M}_{\odot} < M_{\mathrm{halo}} < 10^{14}\ h^{-1}\ \mathrm{M}_{\odot}$, identifying satellites as quenched according to the sSFR cut of 10^{-11} yr^{-1} described in §2.3.1. Unlike our photometric analysis, however, we include groups across the entire SDSS spectroscopic footprint — i.e. both within and beyond the Stripe 82 footprint. From this parent population, we then select two subsamples at $z < 0.06$ and at $z < 0.1$. The lower-z ($z < 0.06$) sample includes $\sim$ 1500 groups with $\sim$ 14,000 satellite galaxies, complete down to a stellar mass of $\sim 10^{10}$ $\mathrm{M}_{\odot}$. The higher-z sample includes more host systems ($\sim$ 8000 groups with $\sim$ 40,000 satellites), but only probes down to $\sim 10^{10.5}$ $\mathrm{M}_{\odot}$. In agreement with many previous studies of satellite properties at $z \sim 0$ (e.g. Baldry et al., 2006; Wetzel et al., 2013; Woo et al., 2013; Hirschmann et al., 2014; Omand et al., 2014), we find that the satellite quenched fraction decreases with decreasing satellite stellar mass, such that nearly all satellites are quenched at $> 10^{11}$ $\mathrm{M}_{\odot}$ with a quenched fraction of $< 50\%$ at $\sim 10^{10}$ $\mathrm{M}_{\odot}$.

In an effort to push measurements of the satellite quenched fraction to lower masses (i.e. $< 10^{10}$ $\mathrm{M}_{\odot}$), we use the background subtraction technique described in §2.4.1 as applied to our photometric sample in Stripe 82. Accordingly, we compute the satellite quenched fraction as a function of stellar mass as

$$f_q^{sats}(d_{\mathrm{proj}}, M_{\star}) = \frac{\bar{N}_{\mathrm{sats,q}}}{\bar{N}_{\mathrm{sats,q}} + \bar{N}_{\mathrm{sats,sf}}} \ , \tag{2.3}$$

where $\bar{N}_{\mathrm{sats,sf}}$ and $\bar{N}_{\mathrm{sats,q}}$ are the average number of star-forming and quenched satellites detected at $d_{\mathrm{proj}} < 400$ kpc, respectively. As discussed in §2.4.1, we adopt 400 kpc as the outer extent of ours groups based upon a comparison to comparable halos in the IllustrisTNG simulation suite. Our resulting satellite quenched fraction, however, remains qualitatively

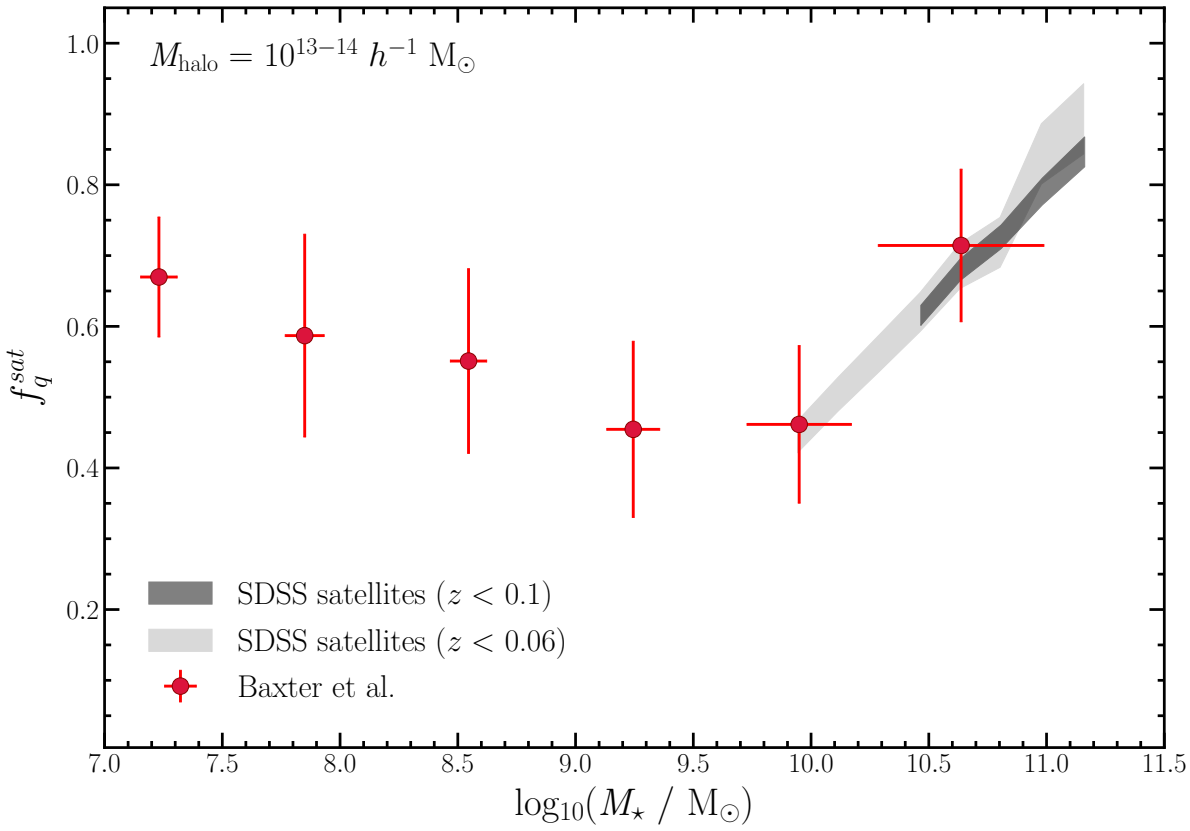

Figure 2.8: The satellite quenched fraction as a function of stellar mass for group environments with $M_{\rm halo} = 10^{13-14}\ h^{-1}\ {\rm M}_\odot$. The solid red points represent the median quenched fraction for our statistically-derived satellite population. The vertical error bars correspond to the 1σ Poisson error in the quenched fraction, while the horizontal error bars denote the standard deviation of the binned stellar masses. The shaded grey (light-grey) band represents the quenched fraction for the spectroscopic members of the Yang et al. (2007) groups at $z < 0.1$ ($z < 0.06$). Our statistically-driven approach using S82 photometry successfully reproduces the satellite quenched fraction results at high masses ($> 10^{10}$ ${\rm M}_\odot$), and pushes beyond previous studies to probe satellite quenching down to 10^7 ${\rm M}_\odot$. We find an increase in the quenched fraction at low masses ($\lesssim 10^9$ ${\rm M}_\odot$), potentially indicating an increase in the efficiency of quenching in the low-mass regime.

unchanged when integrating satellite counts out to 600 kpc or 800 kpc.

Figure 2.8 shows the measured satellite quenched fraction as a function of satellite stellar mass using the spectroscopic group membership and our photometric analysis. For the stellar mass range at which both approaches overlap (i.e. $M_\star > 10^{10}$ $M_\odot$), we find excellent agreement between the independent measurements. This serves as a strong validation of the background-subtraction technique and our classification model.

Using the deeper photometry in Stripe 82, we are able to push our measurements of the satellite quenched fraction down to $\sim 10^7$ $M_\odot$, probing satellite quenching in group environments across four orders of magnitude in satellite stellar mass. In contrast to measurements in the high-mass regime ($> 10^{10}$ $M_\odot$), we find that the satellite quenched fraction in $M_{\rm halo} \sim 10^{13-14}$ h^{-1} $M_\odot$ groups increases below satellite stellar masses of $\sim 10^9$ $M_\odot$. This transition in the quenched fraction suggests a change in the quenching efficiency (and possibly dominant quenching mechanism), such that the suppression of star formation in low-mass satellites is increasingly efficient at $M_\star \lesssim 10^9$ $M_\odot$.

2.5 Summary and Discussion

We have utilized a combination of supervised machine learning and statistical background subtraction to measure the satellite quenched fraction in group environments across four orders of magnitude in satellite stellar mass ranging from $M_\star \sim 10^{7-11}$ $M_\odot$. Our analysis utilizes a neural network classifier trained on a spectroscopic training set to label galaxies in the co-added Stripe 82 photometric catalog as either star forming or quenched based solely on their $g-r$, $g-i$, and $r-i$ colors. The results from this procedure were subsequently used to statistically identify the quenched and star-forming satellite populations around spectroscopically-confirmed hosts within Stripe 82 with halo masses between 10^{13-14} h^{-1} $M_\odot$.

The main results from this analysis are as follows:

1. Using our photometric approach, we successfully reproduce the measured satellite quenched fraction at $M_\star \gtrsim 10^{10}$ $M_\odot$, as derived from spectroscopic studies in the local Universe. We find that the satellite quenched fraction increases with increasing satellite mass at $M_\star \gtrsim 10^{10}$ $M_\odot$.

2. We measure the satellite quenched fraction down to $M_\star \sim 10^7$ $M_\odot$, pushing measurements of satellite quenching in $\sim 10^{13-14}$ h^{-1} $M_\odot$ halos to a new regime that is not readily probed outside of the Local Group.

3. We find that the satellite quenched fraction increases towards lower satellite masses below $\sim 10^9$ $M_\odot$.

4. The increase in satellite quenching at low masses potentially indicates a change in the dominant quenching mechanism at $\sim 10^9$ $M_\odot$, where ram-pressure stripping begins to become increasingly effective (see discussion that follows).

Given that low-mass field galaxies are almost entirely star forming as a population, the increase in the satellite quenched fraction at $< 10^9$ $M_\odot$ can be interpreted as a corresponding increase in the satellite quenching efficiency within 10^{13-14} h^{-1} $M_\odot$ halos. This increase is similar to that observed in the Local Group, where there is an apparent transition in the dominant quenching mechanism at $\sim 10^8$ $M_\odot$ with lower-mass satellites quenched more efficiently following infall. Both hydrodynamic simulations and analytical modeling of the satellite population find that ram-pressure stripping is much more efficient below 10^8 $M_\odot$ within Milky Way-like galaxies (Mayer et al., 2007; Fillingham et al., 2016; Simpson et al.,

2018; Akins et al., 2020), while more massive satellites are primarily quenched via starvation (Fillingham et al., 2015). Given that our host sample is more massive ($M_{\rm halo} = 10^{13-14}$ M$_\odot$) relative to Milky Way-like halos, it is expected that an increase in infall velocities and the density of the circumgalactic medium would cause this transition mass to increase, such that starvation is the primary driver of satellite quenching above $\sim 10^{9.5}$ M$_\odot$ and ram-pressure stripping becoming increasingly important in the low-mass regime. A more detailed study of the potential quenching mechanisms at play requires further analysis of the timescales on which the observed satellites are quenched following infall to the host halos. In future work (Baxter et al. in prep), we aim to bridge this gap by combining the measured satellite quenched fractions from this work with the accretion and orbital histories determined using high-resolution cosmological simulations, to estimate the typical quenching timescale as a function of satellite mass.

The satellite quenched fractions that we obtain at low-masses ($M_\star < 10^9$ M$_\odot$) are generally lower than what have been reported in studies of dwarf galaxies in more massive nearby clusters. For example, Weinmann et al. (2011) studied the satellite galaxy population in the nearby Virgo ($M_{\rm halo} \sim 1.4$–4×10^{14} M$_\odot$), Coma ($M_{\rm halo} \sim 1.3 \times 10^{15}$ M$_\odot$), and Perseus ($M_{\rm halo} \sim 6.7 \times 10^{14}$ M$_\odot$) clusters, finding red fractions between $70-80\%$ at stellar masses of $\sim 10^{8-10}$ M$_\odot$ (see also Boselli et al. 2016a). At slightly higher redshift ($z \sim 0.2$), analysis of the satellite population in Abell 209 ($M_{\rm halo} \sim 10^{15}$ M$_\odot$) by Annunziatella et al. (2016) also finds an elevated quenched fraction relative to our results in less massive halos. Interestingly, while the study of Annunziatella et al. (2016) only probes down to $\sim 10^{8.6}$ M$_\odot$ in satellite stellar mass, the results show a quenched fraction that decreases from near unity ($\sim 95\%$) at $M_\star \sim 10^{10.5}$ M$_\odot$ to $\sim 75\%$ at $M_\star \sim 10^9$ M$_\odot$ (see also Sarrouh et al. in prep). Naively, if there is a transition in the dominant quenching mechanism (or efficiency) in these massive clusters similar to that found in the Local Group and our group sample, we would expect the transition scale to occur at higher satellite masses (e.g. $\gtrsim 10^{9.5}$ M$_\odot$) as ram-pressure stripping (and other cluster-specific processes) should be increasingly effective in hosts with

$M_{\rm halo} \sim 10^{15}$ M$_\odot$. Extrapolations of the mass functions from Annunziatella et al. (2016), however, do not support this picture.

Finally, we report satellite quenched fractions in the low-mass regime ($< 10^8$ M$_\odot$) that are potentially lower than expected when compared to studies of satellite quenching in the Local Group, where $\sim 90\%$ of satellites with $M_\star < 10^8$ M$_\odot$ are passive. As discussed above, environmental quenching mechanisms are expected to be more efficient in our more-massive host halos relative to the Local Group. Of course, our results are based on a study of ~ 100 groups, whereas studies of the Local Group satellites sample only two host halos. While observations of the nearby M81 group yield a satellite quenched fraction comparable to that measured for the Local Group (Kaisin & Karachentsev, 2013; Karachentsev et al., 2013), various studies also indicate that the Local Group satellites may be outliers relative to the cosmic mean (e.g. Boylan-Kolchin et al., 2010; Busha et al., 2011; Tollerud et al., 2011; Ibata et al., 2013; Pawlowski & Kroupa, 2020). Moreover, recent results from the Satellites Around Galactic Analogs (SAGA) Survey (Geha et al., 2017; Mao et al., 2020) find lower satellite quenched fractions ($\sim 20\%$) around hosts with halo masses comparable to those of the Milky Way and M31. We contend that the application of the methodology presented in this work to Milky Way-like hosts is an intriguing way to better place the Local Group into a cosmological context and constrain the quenching of satellites around hosts with $M_{\rm halo} \sim 10^{12}$ M$_\odot$.

Chapter 3

Constraining the Satellite Quenching Timescale in Massive Clusters at $z \gtrsim 1$

The lifetime of a human being is measured by decades, the lifetime of the Sun is a hundred million times longer. Compared to a star, we are like mayflies, fleeting ephemeral creatures who live out their lives in the course of a single day.

– Carl Sagan

3.1 Introduction

Observations of galaxies in the local Universe have long shown that various galaxy properties are strongly correlated with the local environment (i.e. the local galaxy density). For example, satellite galaxies that reside in high-density groups and clusters are more likely to have

older stellar populations, exhibit elliptical or spheroidal morphologies, and have depressed rates of star formation relative to their counterparts that reside (primarily as central galaxies) in the lower-density field (Oemler, 1974; Dressler, 1980; Balogh et al., 1997; Gómez et al., 2003; Blanton et al., 2005; Cooper et al., 2010a). More recent studies suggest that these environmental trends extend out to $z \sim 3$, with passive galaxies already favoring higher-density regions at earlier cosmic times (Cooper et al., 2006, 2007, 2010b; Muzzin et al., 2012; Darvish et al., 2016; Lee-Brown et al., 2017; Lemaux et al., 2019; McConachie et al., 2021). This distinction between central galaxies that reside in the low-density field and satellite galaxies that reside in high-density groups and clusters may be partially due to the latter population being unable to accrete cold gas after crossing into the virialized region of a group or cluster through a process known as 'starvation' or 'strangulation' (Larson et al., 1980; Kawata & Mulchaey, 2008). However, this is far from the only proposed environmentally-driven mechanism for suppressing (or "quenching") star formation; other competing mechanisms include ram-pressure stripping (Gunn & Gott, 1972; Abadi et al., 1999), tidal stripping (Merritt, 1983; Moore et al., 1999; Gnedin, 2003), harassment (Farouki & Shapiro, 1981; Moore et al., 1996, 1998), and feedback-related processes such as overconsumption (McGee et al., 2014; Balogh et al., 2016). Despite the vast number of proposed environmental quenching scenarios, the exact physical mechanism(s) responsible for the aforementioned trends observed in groups and clusters and how they evolve throughout cosmic time remain poorly understood.

A common goal of many studies of environmental (or satellite) quenching is to determine the efficiency with which the local environment suppresses star formation – i.e. the timescale upon which satellite quenching operates. For that reason, a frequently employed method for understanding quenching efficiency, and potentially isolating the dominant physical mechanism(s) responsible for quenching star formation in dense environments, involves combining observations of groups and clusters with simple quenching models applied to N-body simulations to infer the satellite quenching timescale ($\tau_{\rm quench}$), which is typically defined as the time required for a galaxy to transition from star forming to quiescent after becoming a

satellite (i.e. after infall onto its host system). A general assumption of this technique is that galaxy quenching can largely be divided into two regimes: [*i*] internal quenching that acts in all environments (or at least within the field population) with increasing efficiency at higher stellar masses and [*ii*] environmental quenching that operates in massive halos or high-density environments (i.e. groups and clusters) with efficiency that likely depends on local environmental density as well as the mass of the satellite and that of the host halo – a scenario that is supported by observations at low and intermediate redshift (e.g. Baldry et al., 2006; Peng et al., 2010; Woo et al., 2013; Reeves et al., 2021). To a large extent, the application of this methodology has primarily been dominated by studies of satellite quenching in the local Universe. In fact, numerous analyses of low-redshift groups and clusters, spanning a broad range in host halo mass, have utilized high-resolution, cosmological simulations to infer the typical satellite quenching timescale down to the ultra-faint dwarf regime (De Lucia et al., 2012; Wetzel et al., 2013; Hirschmann et al., 2014; Wheeler et al., 2014; Fillingham et al., 2015; Davies et al., 2016; Pallero et al., 2019; Rodriguez Wimberly et al., 2019b).

Herein, we aim to extend the aforementioned studies of the satellite quenching timescale at low redshift to $z \sim 1$ by performing a similar analysis utilizing observations of satellite galaxies residing in clusters at $0.8 < z < 1.4$. In §3.2, we describe our observed galaxy cluster data set, including a discussion of cluster membership criteria and completeness corrections. In §3.3, we detail the high-resolution, cosmological simulation data utilized in our analysis and explain how we construct our simulated sample of cluster galaxies. We describe our satellite quenching model and present the results from implementing said model in §3.4 and §3.5, respectively. Finally, in §3.6, we discuss variations of our model and how our results relate to similar analyses as a function of cosmic time, before summarizing our results in §3.7. When necessary, we adopt a flat ΛCDM cosmology with $H_0 = 70$ km s^{-1} Mpc^{-1} and $\Omega_m = 0.3$. All magnitudes are on the AB system (Oke & Gunn, 1983).

Name	M_{200} [10^{14} $M_\odot$]	R_{200} [cMpc]	z	$N_{\rm members}$
SpARCS0034	0.6	1.08	0.867	23
SpARCS0035	3.8	2.17	1.335	18
SpARCS0036	3.6	2.09	0.869	45
SpARCS0215	2.4	1.70	1.004	34
SpARCS0335	1.8	1.59	1.368	7
SpARCS1047	2.5	1.78	0.956	26
SpARCS1051	2.2	1.80	1.035	26
SpARCS1613	11.1	2.97	0.871	68
SpARCS1616	3.3	1.98	1.156	39
SpARCS1634	2.7	1.85	1.177	34
SpARCS1638	1.7	1.56	1.196	20
SPT0205	3.1	1.77	1.323	19
SPT0546	5.8	2.42	1.067	27
SPT2106	7.3	2.62	1.131	30

Table 3.1: Properties of our GOGREEN cluster sample, including M_{200}, R_{200}, cluster redshift, and the number of spectroscopic members (with $M_\star > 10^{10}$ $M_\odot$). The values in the R_{200} and M_{200} columns were obtained using the MAMPOSSt method (Mamon et al., 2013) as outlined in Biviano et al. (2021). Details regarding the cluster membership criteria are discussed in Sec. 3.2.2.

3.2 Observed Cluster Sample

3.2.1 GOGREEN and GCLASS Cluster Sample

Our cluster sample is drawn from the Gemini CLuster Astrophysics Spectroscopic Survey (GCLASS) and the Gemini Observations of Galaxies in Rich Early ENvironments (GOGREEN) survey (Muzzin et al., 2012; Balogh et al., 2017, 2021).[1] These surveys combine deep, multi-wavelength photometry with extensive Gemini/GMOS (Hook et al., 2004) spectroscopy of galaxies in 26 overdense systems over a redshift range of $0.867 < z < 1.461$, with the primary objective of studying galaxy evolution in high-density environments. The sample utilized in our analysis consists of 14 clusters with halo masses in the range from $10^{13.8-15}$ $M_\odot$ and spectroscopic redshifts of $0.867 < z < 1.368$. Eleven of these clusters

[1] http://gogreensurvey.ca/data-releases/data-packages/gogreen-and-gclass-first-data-release/

were selected from the Spitzer Adaptation of the Red-sequence Cluster Survey (SpARCS, Wilson et al., 2009; Muzzin et al., 2009; Demarco et al., 2010), where they were detected in shallow z' and IRAC 3.6μm images due to their overdensity of red-sequence galaxies (Gladders & Yee, 2000). The remaining three clusters were drawn from the South Pole Telescope (SPT) survey (Brodwin et al., 2010; Foley et al., 2011; Stalder et al., 2013) and were initially detected via their Sunyaev-Zeldovich (Sunyaev & Zeldovich, 1970) signature and later spectroscopically confirmed. In Table 3.1, we provide properties of our cluster sample including halo mass (M_{200}) and radial scale (R_{200}) – which are both obtained using the MAMPOSSt method (Mamon et al., 2013) as outlined in Biviano et al. (2021) – along with redshift and the number of spectroscopic cluster members with $M_\star > 10^{10}$ M$_\odot$.

We also utilize data from the deep, multi-wavelength imaging of each GOGREEN system (van der Burg et al., 2013, 2020). From the photometric catalogs, we employ photometric redshift and stellar mass measurements as well as rest-frame $U-V$ and $V-J$ colors, which are used to determine cluster membership and classify galaxies as either star forming or quenched (see §3.2.2). As described in van der Burg et al. (2020), the photometric redshifts were estimated using the `EAZY` code (Version May 2015, Brammer et al. 2008) by fitting the multi-wavelength photometry to spectral energy distribution templates from the PEGASE model library (Fioc & Rocca-Volmerange, 1997) along with a red galaxy template from Maraston (2005). Furthermore, the stellar masses were estimated by fitting the photometry to stellar population synthesis models (Bruzual & Charlot, 2003) using the `FAST` code (Kriek et al., 2009), assuming solar metallicity, a Chabrier (2003) initial mass function, and the dust law from Calzetti et al. (2000).

3.2.2 GOGREEN Cluster Membership and Classification

We determine cluster membership for our observational sample by first measuring the comoving projected radial cluster-centric distance, $R_{\rm proj}$, for all objects – excluding the centrals – in the field of the 14 clusters that comprise our sample. We then exclude all objects that are not within R_{200} of the cluster, which is defined as the comoving radius of a sphere centered at the position of the central within which the mean density is 200 times the critical density of the Universe. We further restrict our satellite sample to only include objects with $M_\star > 10^{10}$ M$_\odot$, which is slightly above the $\sim 80\%$ stellar mass completeness limit for the sample (van der Burg et al., 2020). From here, we apply the following cluster membership selection criteria to the subsample of objects with high-quality spectroscopic redshifts. Namely, we only include objects with secure spectroscopic redshifts (Redshift_Quality = 3,4) and $|z_{\rm spec} - z_{\rm cluster}| \leq 0.02(1 + z_{\rm spec})$.[2] Likewise, for the subsample of objects without high-quality spectroscopic redshifts, we identify membership based on objects with STAR $\neq 1$ and $|z_{\rm phot} - z_{\rm cluster}| \leq 0.08(1 + z_{\rm phot})$, where the STAR flag is the GOGREEN star/galaxy classification based on color selection, as described in van der Burg et al. (2020). The choice to only include galaxies with $|z_{\rm phot} - z_{\rm cluster}| \leq 0.08(1 + z_{\rm phot})$ was informed by our knowledge that the photometric-redshift uncertainty for galaxies more massive than 10^{10} M$_\odot$ is $0.048(1 + z)$. Nevertheless, we find that if we subsequently characterize and account for interlopers and incompleteness, as described in §3.2.3, the results of our analysis do not depend on the

Δz threshold adopted as part of this particular membership criterion. Altogether, these membership selection criteria yield a total of 1072 cluster members (416 spectroscopic/656 photometric). Lastly, we classify the quiescent members of our cluster population using the following rest-frame UVJ color-color cuts defined by Whitaker et al. (2011, see also Williams

[2]Please refer to Balogh et al. (2021) for a description of the redshift quality flags and the assignment process.

et al. 2009):

$$\begin{aligned} &(\mathrm{U}-\mathrm{V}) > 1.3 \ \cap \ (\mathrm{V}-\mathrm{J}) < 1.6 \ \cap \\ &\quad (\mathrm{U}-\mathrm{V}) > 0.88 \times (\mathrm{V}-\mathrm{J}) + 0.59 \ . \end{aligned} \tag{3.1}$$

3.2.3 Completeness Correction

In order to obtain an accurate measurement of the satellite quenched fraction, we must account for incompleteness and interlopers that inevitably contaminate our photometric sample. This is accomplished following the methodology utilized in van der Burg et al. (2013, 2020) that accounts for completeness in the cluster sample by computing a membership correction factor using the sample of galaxies with both multi-band photometry and z_{spec} measurements and then applying that factor to the photometric sample. The membership correction factor (Eqn. 3.2) is defined as the sum of the number of galaxies that are either secure cluster members or false negatives divided by the sum of secure cluster members and false positives,

$$C_{\mathrm{factor}} = \frac{N(\text{secure cluster}) + N(\text{false negative})}{N(\text{secure cluster}) + N(\text{false positive})} \ . \tag{3.2}$$

Here, secure cluster members are defined as objects identified as cluster members based on their spectroscopic redshift *and* with photometric redshifts consistent with membership, whereas false negatives are objects that are spectroscopically-confirmed cluster members with a photo-z that is inconsistent with cluster membership. Lastly, false positives are defined as objects that are not cluster members based on their spectroscopic redshift but have a photo-z consistent with the redshift of the cluster. Following the methodology of van der Burg et al. (2020), we compute the correction factor separately for star-forming and quiescent galaxies in order to account for the presumed color dependence of field contamination. Furthermore, for both populations we compute the correction factor in bins of stellar mass ranging from

$10^{10.0-11.4}$ $M_\odot$ and $R_{\rm proj}/R_{200}$ from $0-1$. As a function of galaxy color, we find a very modest variation in the completeness correction, with the correction factor as applied to the star-forming and quiescent populations differing by $\lesssim 2\%$. Finally, we apply the appropriate correction factor as a weight to each cluster member, which we find yields a modest change in the measured quenched fractions (at the level of $\sim 1-2.5\%$), such that the final results of our analysis and the conclusions therein drawn remain unchanged irrespective of the application of this completeness correction.

3.3 Simulated Cluster Sample

3.3.1 IllustrisTNG Cluster Sample

We utilize the TNG300-1 simulation from the IllustrisTNG project[3] (TNG, Nelson et al., 2018; Naiman et al., 2018b; Springel et al., 2018; Pillepich et al., 2018; Marinacci et al., 2018) to establish a simulated cluster population that is matched on redshift to our observed cluster sample. TNG300-1 is a large volume (~ 300 cMpc^3), high-resolution (2×2500^2 resolution elements), cosmological, gravo-magnetohydrodynamical simulation that utilizes the moving mesh `AREPO` code and solves for the coupled evolution of dark matter, cosmic gas, luminous stars, and supermassive black holes from a starting redshift of $z = 127$ to the present day, $z = 0$. TNG300-1 has a dark matter (gas) mass resolution of $m_{\rm DM} = 5.9 \times 10^7$ $M_\odot$ ($m_{\rm baryon} = 1.1 \times 10^7$ $M_\odot$), which corresponds to a halo mass (stellar mass) completeness of $\sim 10^{10}$ $M_\odot$ ($\sim 10^9$ $M_\odot$). As explained in §3.3 of Pillepich et al. (2018), we augment the stellar masses for TNG300-1 galaxies at $z \sim 1$ by a factor of $1.3\times$ to account for resolution limitations that systematically underestimate stellar masses within the simulations.

Our simulated cluster sample is drawn from the group catalogs and sublink merger trees

[3]https://www.tng-project.org

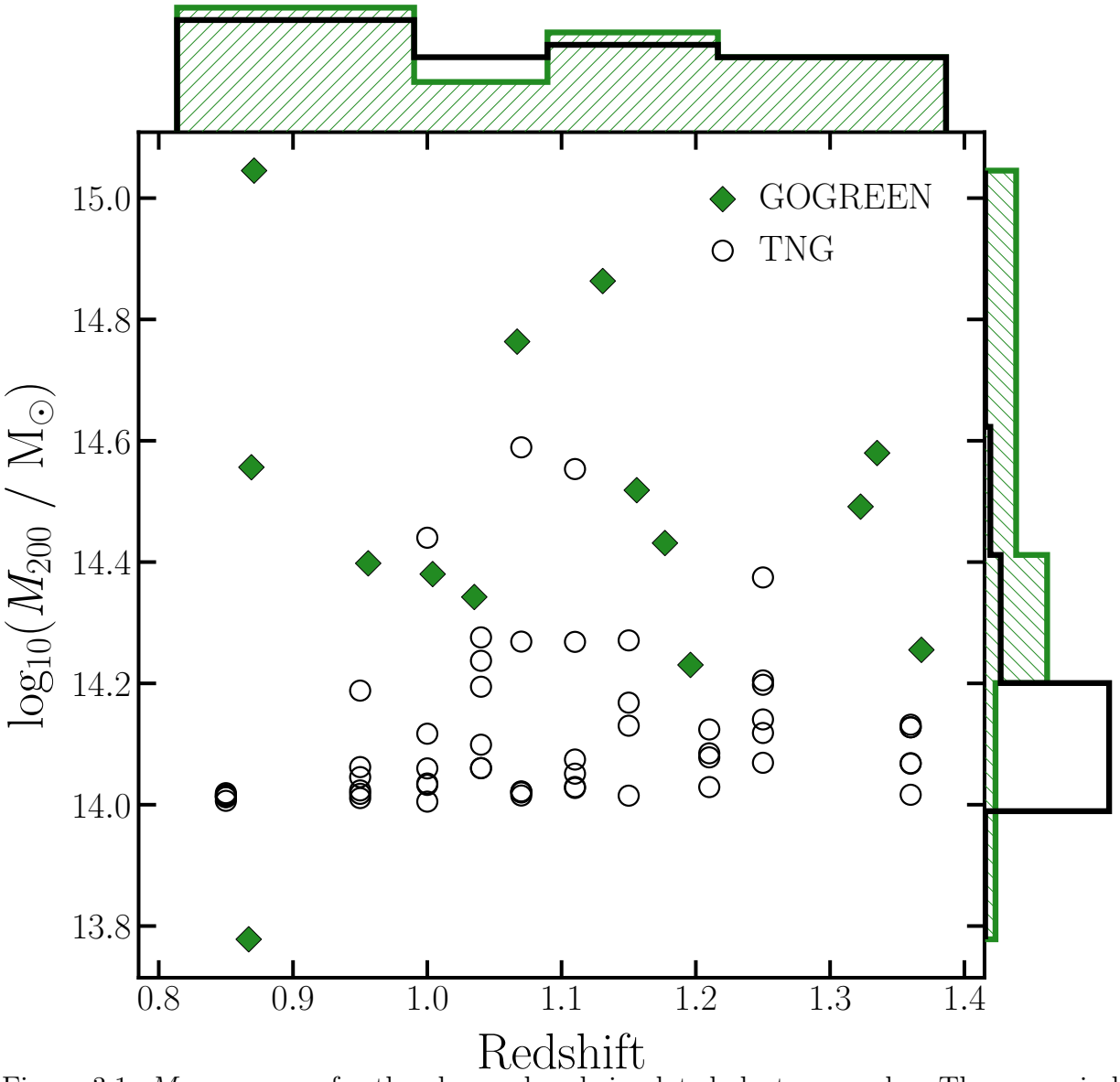

Figure 3.1: M_{200} versus z for the observed and simulated cluster samples. The open circles (filled diamonds) represent the TNG (GOGREEN) clusters. While matched on redshift, the simulated sample is biased towards less-massive systems relative to the observed sample, with the majority of the TNG clusters having halo masses less than $10^{14.3}$ $\mathrm{M}_\odot$. As discussed in §3.3.1, this bias towards low-mass hosts does not significantly impact our results, with a sample matched on M_{200} yielding qualitatively similar results.

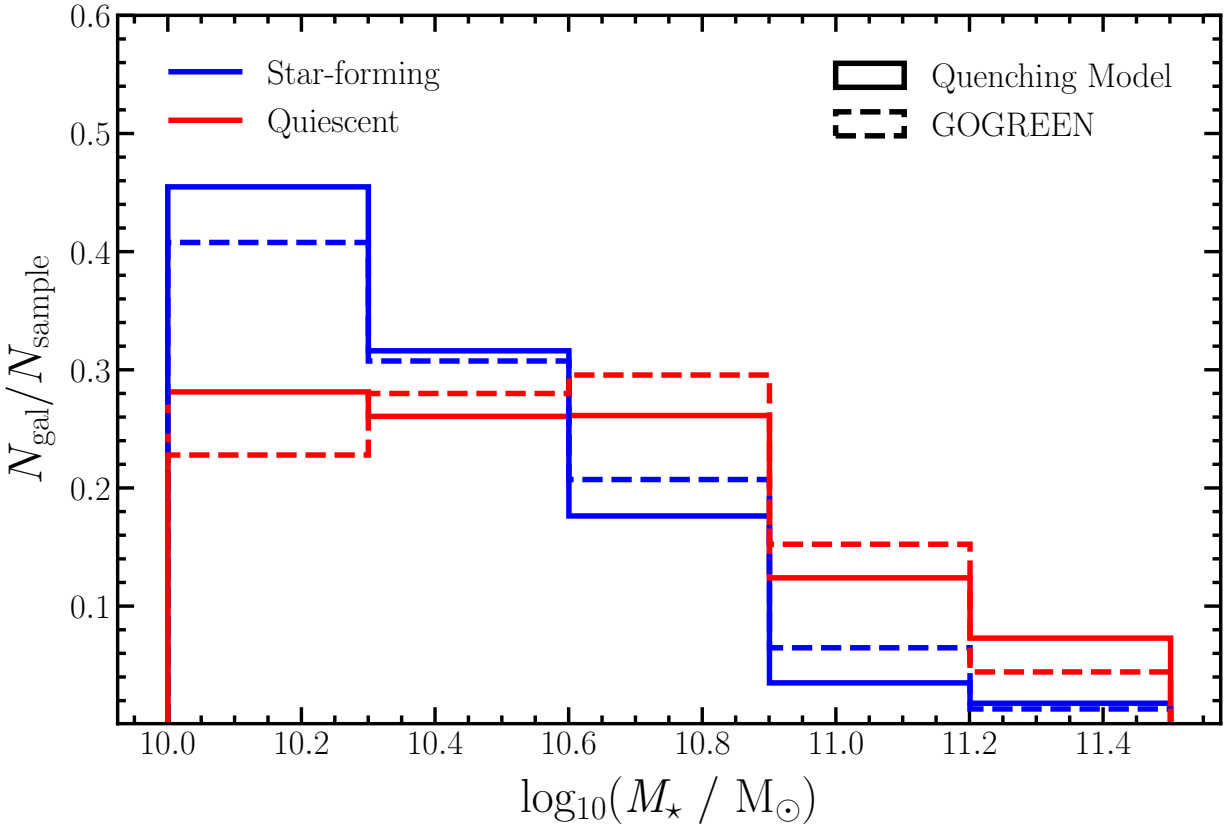

Figure 3.2: Comparison of the normalized stellar mass distributions for GOGREEN cluster members to that of our simulated satellite population. The blue and red solid (dashed) lines illustrate the simulated (observed) stellar mass distribution for star-forming and quenched galaxies, respectively. Note that the simulated cluster members are classified according to our quenching model that is designed to reproduce the observed $f_{\rm q}^{sat}(M_\star)$ results (see §3.4). While the TNG sample slightly underpredicts the total number of satellites due its bias towards lower host halo masses, the relative distribution of satellite masses is in excellent agreement.

associated with the TNG300-1 simulation. As a whole, TNG300-1 contains a total of 100 snapshots ranging from $z = 20.05$ to $z = 0$; however, our cluster sample is constructed using only 10 snapshots ranging from $z = 1.36$ to $z = 0.85$, so as to match the redshift distribution of the GOGREEN cluster sample. Each of these snapshots contains a unique group catalog that includes both friends-of-friends (FoF; Davis et al., 1985) and SUBFIND objects (Springel et al., 2001; Dolag et al., 2009). The FoF catalog contains the GroupFirstSub column that holds the indices into the SUBFIND catalog for the first/primary/most massive subhalo group within each FoF group, and we define these subhalos to be our centrals. With the total central population defined, we use the TNG300-1 Sublink merger trees to track the SUBFIND IDs of the sample from $z = 0.85$ to $z = 1.36$, which allows unique centrals to be identified across the 10 snapshots. Moreover, we combine this information with the redshift distribution of our observed cluster population to construct a sample of simulated clusters that is matched on redshift to the GOGREEN cluster sample. Given the relatively large volume of the TNG300-1 simulation box, we are able to select a total of 56 unique comparison cluster halos from snapshots that range from $z = 1.36$ to $z = 0.85$ with a median redshift of $z = 1.1$. The median redshift difference between a GOGREEN cluster and its simulated analog is $|\Delta z| \sim 0.03$. As illustrated in Fig. 3.1, our simulated host sample has a median halo mass of $M_{\rm halo} = 10^{14.12}$ $M_\odot$ and is, on average, less massive than the GOGREEN cluster sample, which has a median host mass of $10^{14.5}$ $M_\odot$. A consequence of this is that the number of simulated cluster members in our sample is generally less than their observed counterparts by a factor of ~ 3. With this in mind, we repeat our analysis using a more restricted sample of 12 clusters constructed to better match the observed GOGREEN cluster sample with respect to redshift, halo mass, and R_{200}. Utilizing this more-precisely matched sample, we find that our results are qualitatively similar to those based on the the larger and less-precisely matched sample. The robustness of our results is, in part, due to the fact that at fixed stellar mass the infall time distribution for satellites in the low-mass and high-mass clusters, a key ingredient in our modeling (see §3.4), is weakly dependent on host mass with differences in average

infall times on the order of $\sim 0.02 - 0.03$ Gyr. All things considered, we choose the larger host sample, matched solely on redshift, as our simulated cluster population in part due to its ability to better sample the distribution of infall times (and formation histories).

3.3.2 TNG Cluster Membership

For each of the simulated clusters, our sample of cluster members is drawn from the TNG300-1 group catalogs and sublink merger trees. In particular, we define potential cluster members as any object in the Subfind catalog that is not defined as the host within each FoF group. From here, we establish cluster membership for our simulated cluster sample using a procedure similar to that outlined in §3.2.2. Specifically, simulated cluster members are galaxies that satisfy the condition $d_{\rm host}(z_{\rm obs}) < R_{200}$, where $d_{\rm host}(z_{\rm obs})$ is the three-dimensional comoving radial cluster-centric distance at the redshift of observation. We note that this satellite selection criterion is distinct from how observational samples are selected, where projected separations are typically utilized given that three-dimensional separations are largely unattainable. For this reason, we repeat our analysis using a cluster member sample composed of galaxies that lie within a cylinder of radius R_{200} projected on an imaginary sky plane perpendicular to the z-direction of the simulation box, which we define as the line-of-sight direction. In general, we find that selecting satellites according to projected cluster-centric distance yields consistent, though slightly shorter quenching timescales, with the difference (relative to selecting in 3-D) being most pronounced at low satellite masses ($\Delta\tau_{\rm quench} \lesssim -0.1$ Gyr). We find that this remains true even if the satellite selection criterion is expanded to include a line-of-sight velocity threshold analogous to the Δz threshold used for the observed satellite sample. The weak bias towards shorter quenching timescales, when working in projected space, is primarily driven by the inclusion of star-forming interlopers from the field population (Donnari et al., 2021).

In addition to the separation criterion, we also restrict our simulated satellite sample to only include galaxies with resolution-corrected stellar mass of $M_\star > 10^{10}$ $M_\odot$, where the stellar masses are given by the total mass of all star particles associated with each galaxy (i.e. IllustrisTNG SubhaloMassType masses with Type=4). Our adopted stellar mass limit, selected to mirror that of the GOGREEN sample, is well above the stellar mass completeness limit for TNG300-1 of approximately $M_\star \sim 10^9$ $M_\odot$, which corresponds to ~ 100 star particles. Overall, these constraints yield a total of 1220 cluster members across the 56 simulated clusters. As illustrated in Figure 3.2, the TNG-based stellar masses reproduce the relative distribution of satellite stellar masses from the GOGREEN sample. The stellar masses for the simulated satellite sample are taken at $z_{\rm obs}$, such that we do not explicitly model the stellar mass growth of satellites prior to or following infall. The difference in mass due to subsequent star formation (or lack thereof) in comparison to the star formation histories defined by the TNG hydro-dynamical modeling is modest (typically $\Delta M_\star \lesssim 0.3$ dex). In lieu of using the stellar masses provided by TNG300-1, we discuss the implications of defining the stellar masses of our cluster satellites using the stellar mass-halo mass (SMHM) relation from Behroozi et al. (2013) in §3.6.4. Finally, after establishing the simulated galaxy sample we proceed to use the TNG300-1 sublink merger trees to track relevant properties (e.g. position, mass, R_{200}, etc.) of the clusters and their members along the main progenitor branch from $z = 20.05$ to $z_{\rm obs}$.

3.4 Quenching Model

Our quenching model utilizes the TNG simulations to detail the accretion history of the cluster population and complementary "field" observations to describe the properties of infalling galaxies. Together, these inputs allow the model to probabilistically characterize galaxies that quenched prior to infall onto the cluster using the coeval field quenched fraction.

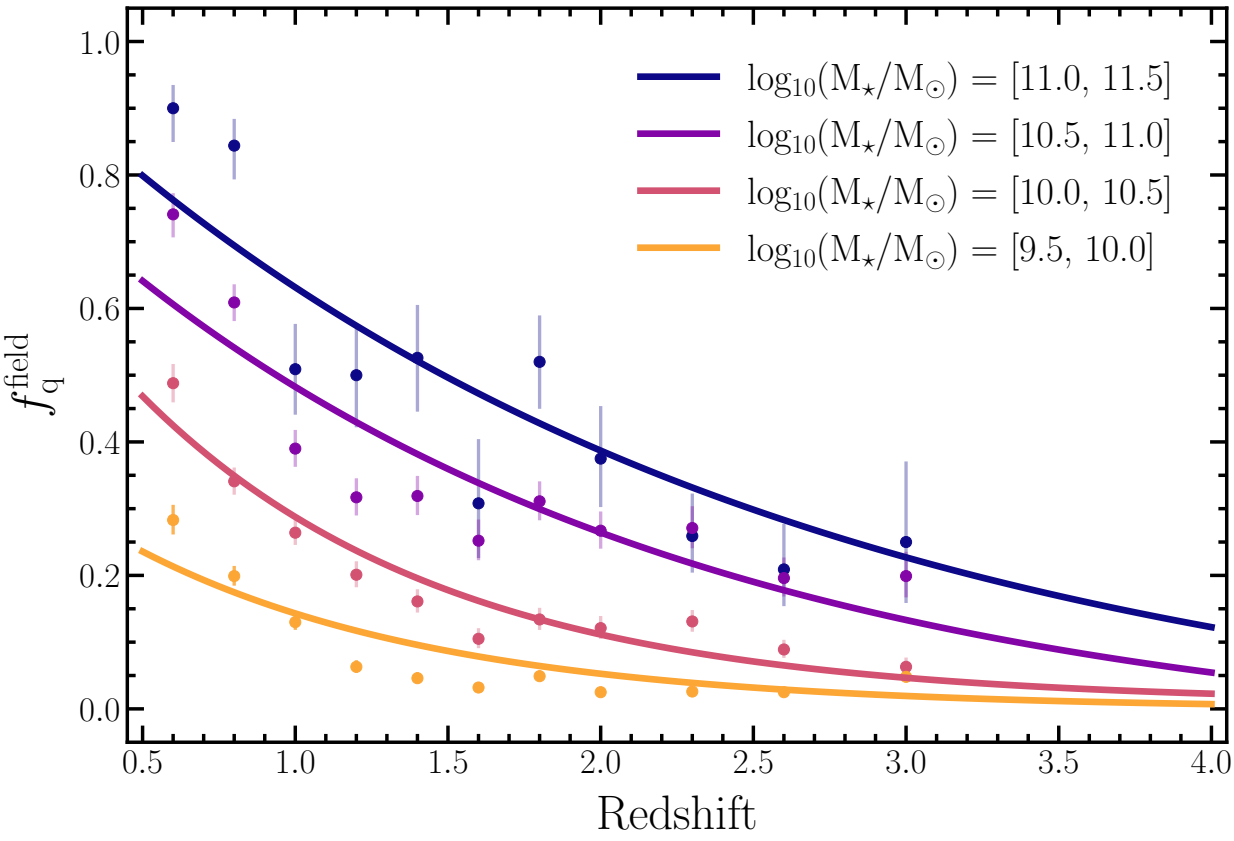

Figure 3.3: Field quenched fraction versus redshift in bins of stellar mass ranging from $10^{9.5}$ $M_\odot$ $< M_\star <$ $10^{11.5}$ $M_\odot$ as inferred from CANDELS observations. The colored circles represent the observed field quenched results in their respective stellar-mass bins, whereas the curves illustrate the corresponding fits to the observed results using an exponentially decaying function. The vertical error bars correspond to the 1-σ binomial uncertainties in the quenched fraction.

At its core, the model has one primary parameter, the satellite quenching timescale ($\tau_{\rm quench}$), which is defined as the time following infall before a star-forming satellite is quenched. This model parameter is tuned so as to reproduce the observed dependence of the satellite quenched fraction on stellar mass, $f_{\rm q}^{\rm sat}(M_\star)$, thereby yielding $\tau_{\rm quench}(M_\star)$.

3.4.1 Infall Times of Simulated Cluster Members

Our procedure for classifying the simulated cluster members that quenched prior to infall begins with computing the infall time ($t_{\rm infall}$) for each simulated satellite, which we define as the time at which a galaxy first crosses R_{200} of the cluster halo. For our simulated satellite population, less than 20% are backsplash systems that crossed R_{200} more than once, with $t_{\rm infall}$ defined as the time of the first crossing. As discussed in §3.6.1, we also investigate an alternative approach in which we classify simulated cluster members at the redshift of observation (versus at the time of infall) to account for the possibility of internal quenching after infall. To measure $t_{\rm infall}$, we use the TNG300-1 sublink merger trees (see §3.3.2) to track the separation between our simulated cluster and satellite samples across the 55 snapshots between $z = 20.05$ and $z = 0.85$. This corresponds to a median time resolution of approximately 100 Myr between each snapshot, which is not ideal for precisely measuring $t_{\rm infall}$ given that the radial cluster-centric separation can change on the order of a few hundred kpc between each snapshot. Therefore, with the objective of obtaining greater precision on $t_{\rm infall}$, we map the spatial position of each galaxy (relative to their host cluster halo) in 10 Myr intervals by spline interpolating the position of each galaxy and corresponding host from $z = 20.05$ to the redshift of the given snapshot. We find that the infall times procured using the spline-interpolated positions are typically ~ 60 Myr earlier when compared to the infall times obtained using the non-interpolated positions. In the following section, we explain how we use these infall times to probabilistically classify our simulated cluster members as star forming or quiescent.

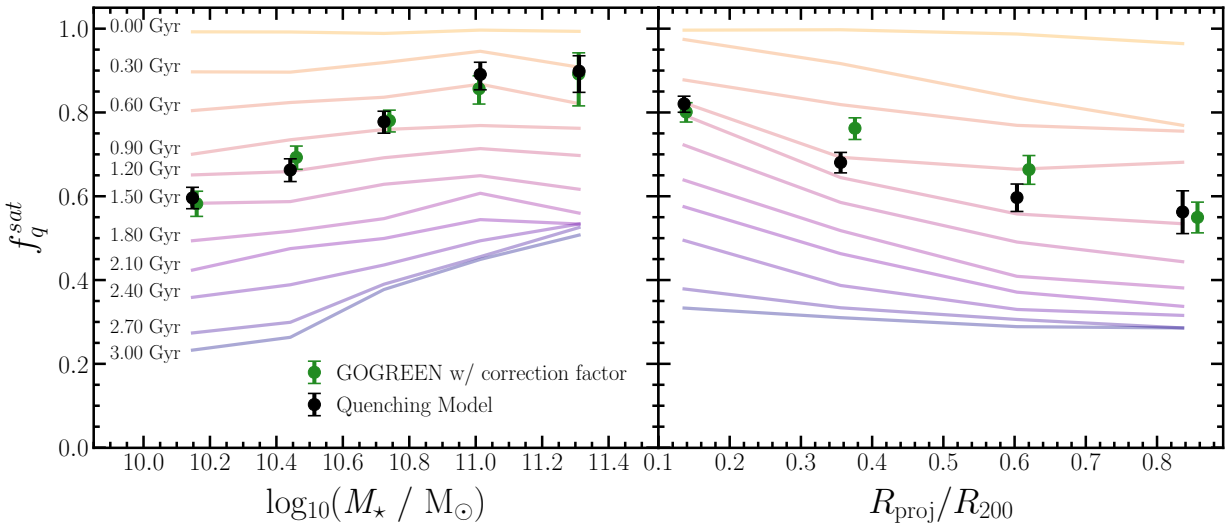

Figure 3.4: Satellite quenched fraction as a function of satellite stellar mass (*left*) and projected cluster-centric distance normalized by R_{200} (*right*). The green circles illustrate the GOGREEN quenched fraction results with the membership correction factor applied. The black circles represent the TNG results fit to the GOGREEN quenched fraction results. The colored profiles in the background represent the TNG quenched fraction results using a constant quenching timescale ranging from 0 to 3 Gyr. The constant quenching timescale model fails to reproduce the observed quenched fraction as a function of stellar mass and cluster-centric radius, however, these trends are reproduced by a model assuming a mass-dependent quenching timescale. All error bars correspond to the 1-sigma binomial uncertainties.

3.4.2 Classifying Simulated Cluster Members

Within our satellite quenching model, each infalling system is probabilistically classified as star forming or quenched according to the corresponding field quenched fraction at the time of infall. In Figure 3.3, we show the field quenched fraction as a function of redshift and stellar mass, $f_{\rm q}^{\rm field}(z, M_\star)$, computed using derived data products from the v1.1 internal data release of the Cosmic Assembly Near-infrared Deep Extragalactic Legacy Survey (CANDELS, Grogin et al., 2011; Koekemoer et al., 2011; Guo et al., 2013; Galametz et al., 2013; Santini et al., 2015; Stefanon et al., 2017; Nayyeri et al., 2017; Barro et al., 2019). To obtain the field quenched fraction, we first identified objects in the CANDELS catalogs with reliable photometry (PHOTFLAG==0) and identified the fraction in the quiescent region of the UVJ diagram following Whitaker et al. (2011). Our field sample totals $57,971$ galaxies, with each bin in redshift and mass including no fewer than 20 galaxies. In agreement with previous analyses, we find that the field quenched fraction depends strongly on stellar mass and redshift, with more massive galaxies more likely to be quenched and the prevalence of quenched systems decreasing at earlier cosmic time. We also find that corresponding measurements of the field quenched fraction, computed using a K_s-selected catalog drawn from the COSMOS/UltraVISTA field (Muzzin et al., 2013a,b; Marsan et al., 2022), yield results that are generally consistent with those derived from the CANDELS dataset.

As previously mentioned, we use $f_{\rm q}^{\rm field}(z, M_\star)$ to probabilistically classify the simulated cluster members that quenched prior to infall. We accomplish this by first fitting the measurements of the field quenched fraction in mass bins (see Fig. 3.3) using an exponentially decaying function to obtain functional forms for the four stellar mass bins between $10^{9.5-11.5}$ $\rm M_\odot$. We then use $z_{\rm infall}$ and $M_{\star,\rm infall}$ values of our simulated satellite population to obtain the expected field quenched fraction at the time of infall. Next, we randomly draw a number from a uniform distribution between zero and one and compare it with the corresponding field quenched fraction. If the randomly drawn number is greater (less) than the observed quenched fraction

then we classify the galaxy as star forming (quenched). This step is repeated 50 times in order to generate an ensemble of classified cluster members that capture the slight variations inherent to this probabilistic classification scheme. As such, the quenched fraction results discussed in §3.5.1 represent the median of the ensemble of classified cluster members.

3.4.3 Determining the Satellite Quenching Timescale

We characterize environmental quenching by employing a simple quenching model that assumes that star-forming satellites quench after some fixed amount of time ($\tau_{\rm quench}$) following infall onto their host cluster halo. The simplicity of this model is that it contains one primary parameter, $\tau_{\rm quench}(M_\star)$, which we allow to vary linearly with satellite stellar mass so as to reproduce the $f_{\rm q}^{\rm sat}(M_\star)$ measurements for our observed cluster sample. In other words, our model translates the observed $f_{\rm q}^{\rm sat}(M_\star)$ into typical quenching timescales by inferring $\tau_{\rm quench}$ in bins of stellar mass so as to minimize the difference between the model and the observations ($|f_{\rm q,obs}(M_\star) - f_{\rm q,model}(M_\star)|$). For an infinitely-long quenching timescale (i.e. no environmental quenching), the minimum satellite quenched fraction is defined by the portion of satellites quenched prior to infall. In §3.5, we present the results of our environmental quenching model and discuss the implications of the inferred quenching timescales.

3.5 Results

3.5.1 Quenched Fraction Results

In Figure 3.4, we compare the GOGREEN observed satellite quenched fraction as a function of stellar mass and projected cluster-centric distance with the corresponding quenched fraction results from our environmental quenching model. The green circles represent the

observed results with the membership correction factor applied. As noted in §3.2.3, the membership correction factor has a relatively small impact on the observed quenched fraction results. We find a strong dependence of the quenched fraction on both $M_\star$ and $R_{\rm proj}/R_{200}$, such that more massive and more centrally-located satellites are more likely to be quenched. These observed trends are in good agreement with similar results at low and intermediate redshift (e.g. Balogh et al., 1998; Christlein & Zabludoff, 2005; Patel et al., 2009; Vulcani et al., 2015; Cooke et al., 2016; Lee-Brown et al., 2017; Baxter et al., 2021). The faded colored lines in Fig. 3.4 show the simulated quenched fraction results when assuming a constant quenching timescale (independent of satellite stellar mass), ranging from $\tau_{\rm quench} = 0 - 3$ Gyr. As illustrated, a fixed quenching timescale fails to reproduce the observed satellite quenched fraction versus stellar mass trend. In contrast, the results of our fiducial quenching model, which assumes a mass-dependent satellite quenching timescale, are illustrated by the black circles in Fig. 3.4. While our model yields the observed $f_{\rm q,sat}(M_\star)$, by design, it also successfully reproduces the observed dependence of quenched fraction on projected cluster-centric distance within the GOGREEN cluster sample.

In Figure 3.5, we compare the observed satellite quenched fraction as a function of redshift to the results from our fiducial quenching model. Over the limited redshift range probed by the GOGREEN survey, the measured satellite quenched fraction is relatively constant (see also Nantais et al. 2017), with excellent agreement between the results for the observed and simulated cluster samples. Overall, our fiducial quenching model is extremely successful, reproducing the observed quenched fraction as a function of stellar mass (by construction), projected cluster-centric distance, *and* redshift.

3.5.2 Inferred Quenching Timescales

In Figure 3.6, we present the $\tau_{\rm quench}(M_\star)$ results that we infer from our fiducial environmental quenching model. Within the framework of our modeling approach, we find that a mass-dependent quenching timescale in which higher-mass galaxies quench more rapidly following infall onto their host halo is necessary to reproduce the measured quenched fraction as a function of satellite stellar mass. In particular, the quenching timescales that we infer steadily decrease with increasing satellite stellar mass, going from ~ 1.6 Gyr at 10^{10} $M_\odot$ to ~ 0.6 Gyr at 10^{11} $M_\odot$.

In general, the relatively short quenching timescale that we infer is consistent with previous studies at $z \sim 1$. For example, analyzing a sample of clusters from GCLASS, including some of the systems studied herein, Muzzin et al. (2014) utilize the location of post-starburst galaxies within the cluster to infer a satellite quenching timescale of ~ 1 Gyr for a sample of satellites with a median stellar mass of roughly a few $\times$ 10^{10} $M_\odot$. Likewise, using stellar population modeling to infer the rest-frame color evolution of satellites in 4 clusters at $z \sim 1.5$, Foltz et al. (2018) find a quenching timescale of $\tau_{\rm quench} \sim 1.1$ Gyr for satellites with $M_\star \gtrsim 10^{10.5}$ $M_\odot$. Finally, Balogh et al. (2016) utilize a method similar to that employed in our analysis and allow for a quenching timescale that depends on stellar mass within a sample of GCLASS clusters at $z \sim 1$. At satellite stellar masses of $> 10^{10}$ $M_\odot$, however, Balogh et al. (2016) find a remarkably constant quenching timescale as a function of satellite mass ($\tau_{\rm quench} \sim 2$ Gyr). While our estimates of the field quenched fraction are similar to those utilized by Balogh et al. (2016), the infall time distribution of our satellite population – as inferred from the TNG simulations – depends non-negligibly on satellite mass, such that lower-mass satellites are preferentially accreted earlier. Quantitatively, we find the median difference in infall times to be about 0.4 Gyr between galaxies with stellar masses of 10^{10} $M_\odot$ and 10^{11} $M_\odot$. In contrast, Balogh et al. (2016) adopt a model where the accretion history of their clusters depends only on host halo mass and not the mass of the satellite. In addition,

the infall times adopted by Balogh et al. (2016) are taken with respect to first infall onto any more massive halo (versus just the cluster halo, McGee et al. 2009). These differences may account for the lack of mass dependence inferred in that work.

As a low-z comparison, in Fig. 3.6, we show the quenching timescale inferred for the highest-mass clusters from the Wetzel et al. (2013) sample (i.e. $M_{\rm halo} = 10^{14-15}$ M$_\odot$), which should roughly correspond to the descendants of our $z \sim 1$ cluster sample.[4] Scaling our results at $z \sim 1$ according to the evolution in the dynamical time – i.e. $\tau_{\rm quench}(M_\star) \times (1+z)^{-1.5}$ – we find good agreement between our inferred mass-dependent satellite quenching timescale and that from Wetzel et al. (2013). In §3.6.2 and §3.6.3, we further examine our quenching timescale constraints with an eye towards the potential physical mechanisms at play.

3.6 Discussion

3.6.1 Internal Quenching after Infall

In contrast to some previous studies of satellite quenching (e.g. Balogh et al., 2016), a fundamental assumption of our fiducial model is that environmental and internal quenching mechanisms are separable, such that only environmental processes are at play once a galaxy becomes a satellite within the cluster halo. That is, we construct our model to account for the impact of internal quenching mechanisms by referencing the coeval field quenched fraction at the time of infall. This, however, inherently assumes that environmental quenching mechanisms dominate within the cluster. To test the validity of this assumption we adopt an alternative approach that allows internal quenching mechanisms to continue operating unabated after infall. We simulate this scenario by modifying our fiducial quenching model

[4]While the typical GOGREEN cluster will evolve into a system with $M_{\rm halo} \sim 10^{15}$ M$_\odot$ at $z \sim 0$, our simulated cluster population will evolve into slightly less massive systems ($M_{\rm halo} \sim 10^{14.5}$ M$_\odot$ at $z \sim 0$).

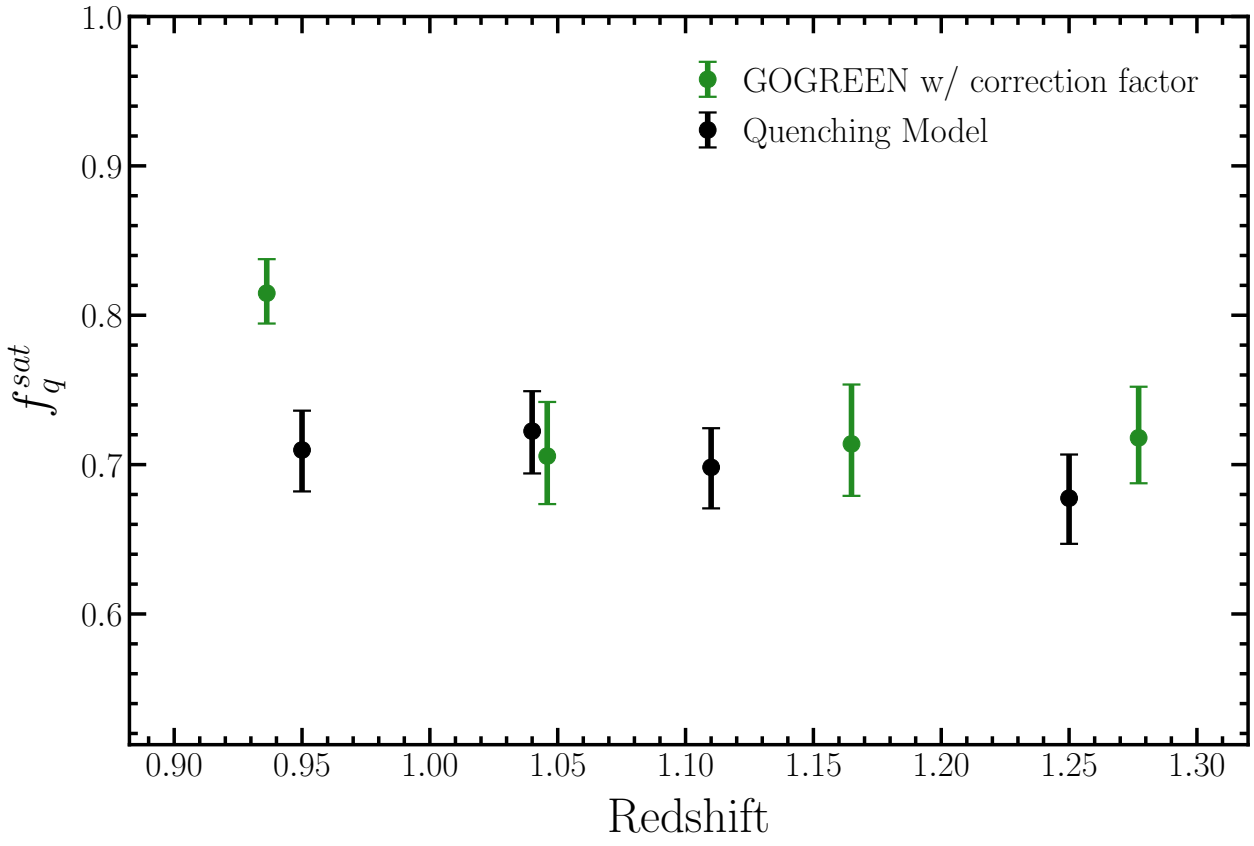

Figure 3.5: Satellite quenched fraction versus redshift. The green circles represent the observed results with the membership correction applied. The black circles shows the corresponding measurements for our fiducial model based on tuning $\tau_{\rm quench}(M_\star)$ to reproduce the observed satellite quenched fraction as a function of stellar mass. For both the observed and simulated samples, the uncertainties correspond to 1-σ binomial errors. Our fiducial quenching model is able to successfully reproduce the observed GOGREEN satellite quenched fraction as a function of stellar mass, projected cluster-centric radius, *and* redshift.

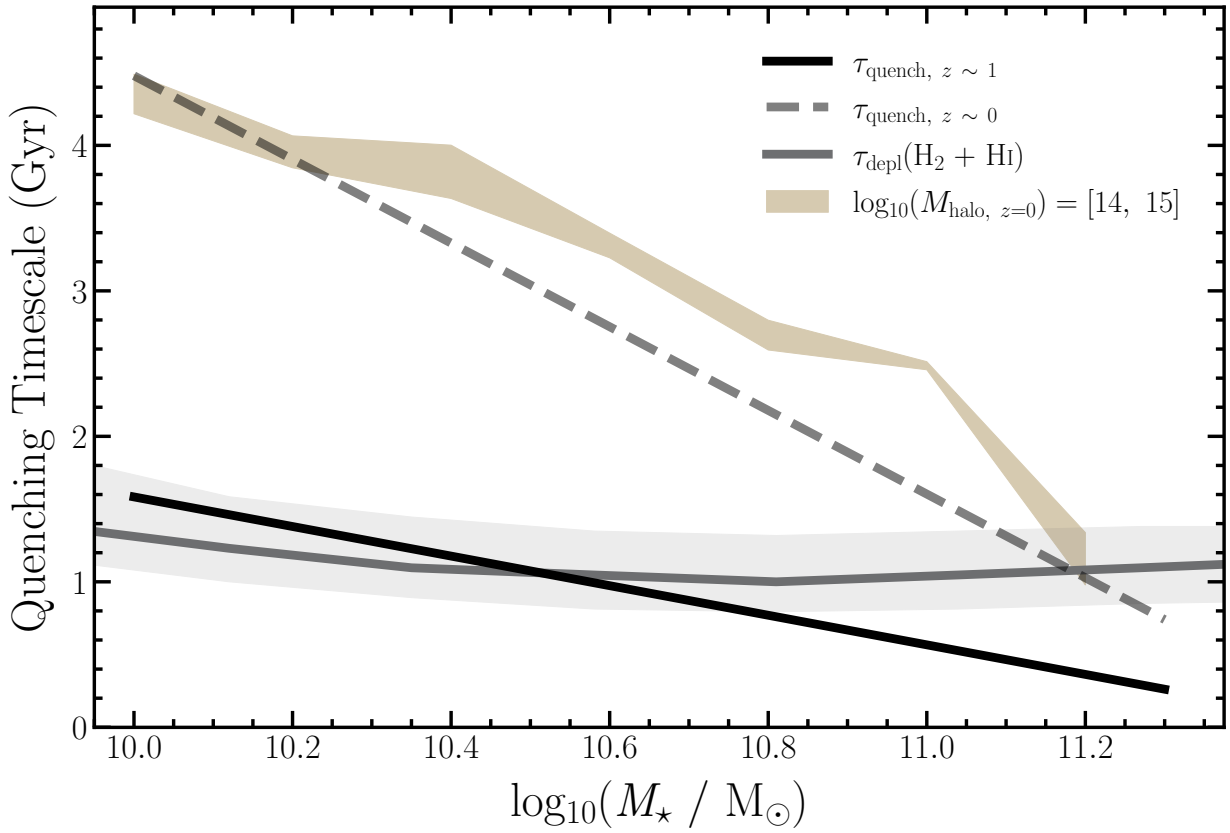

Figure 3.6: Satellite quenching timescale versus satellite stellar mass. The solid grey line illustrates the empirically-derived cold gas (HI + H_2) depletion timescale from Popping et al. (2015) at $z \sim 1.5$, with the corresponding grey shaded region spanning the variation in the depletion timescale over the redshift range $1 < z < 2$. The solid black line represents the results from our fiducial model as applied to the GOGREEN cluster sample at $z \sim 1$ ($M_{\rm halo} \sim 10^{14.5}$). The dashed grey line represents the estimated quenching timescale at $z \sim 0$ obtained by scaling the results from our fiducial model at $z \sim 1$ by $(1+z)^{-3/2}$. In our fiducial model, we find a mass-dependent quenching timescale, favoring more rapid suppression of star formation for more massive satellites. For comparison, the tan colored band shows the quenching timescale constraint from Wetzel et al. (2013) for satellites in clusters ($M_{\rm halo} \sim 10^{14-15}$ $\rm M_\odot$) at $z \sim 0$. For massive hosts, the evolution in the quenching timescale roughly follows the evolution in the dynamical time ($\times(1+z)^{-3/2}$), as shown by the dashed grey line.

such that we classify galaxies as star forming or quenched at the redshift of observation ($z_{\rm obs}$) instead of at $z_{\rm infall}$, then determine the satellite quenching timescale (still relative to infall) needed to achieve the measured satellite quenched fraction as a function of stellar mass. Interestingly, we find that this approach yields very similar results to the scenario in which galaxies are classified at $z_{\rm infall}$, with the resulting satellite quenching timescale ($\tau_{\rm quench}$) as a function of satellite stellar mass consistent within ± 0.02 Gyr for the two formulations of the quenching model.

The relative unimportance of internal quenching post infall for satellites at $z \sim 1$ is, in part, due to the short satellite quenching timescales at this epoch. In addition, the role of internal mechanisms after infall is minimized by the mass-dependent efficiency of internal quenching (see Fig. 3.3) combined with the stellar mass dependence of the infall time distribution, such that more massive galaxies are more likely to be quenched internally but also typically become satellites later than their low-mass counterparts. In other words, given the mass dependence of typical infall times and given that the field quenched fraction as a function of cosmic time increases more slowly (rapidly) for low-mass (high-mass) galaxies, we find that the typical quenched fraction inferred at $z_{\rm obs}$ and $z_{\rm infall}$ are quite similar, thus yielding relatively similar results for the satellite quenching timescale. Overall, the aforementioned modification to our fiducial model indicates that internal quenching mechanisms play at most a secondary role to the environmental quenching mechanism(s) operating within clusters at $z \sim 1$.

3.6.2 Physical Processes Driving Satellite Quenching

The relatively long satellite quenching timescales inferred at low z ($\tau_{\rm quench} \sim 4-7$ Gyr) favor a slowly-acting quenching mechanism. Among the possible mechanisms, the long timescales for satellites at $M_\star \gtrsim 10^9$ M$_\odot$ strongly favor the starvation scenario by which satellites quench

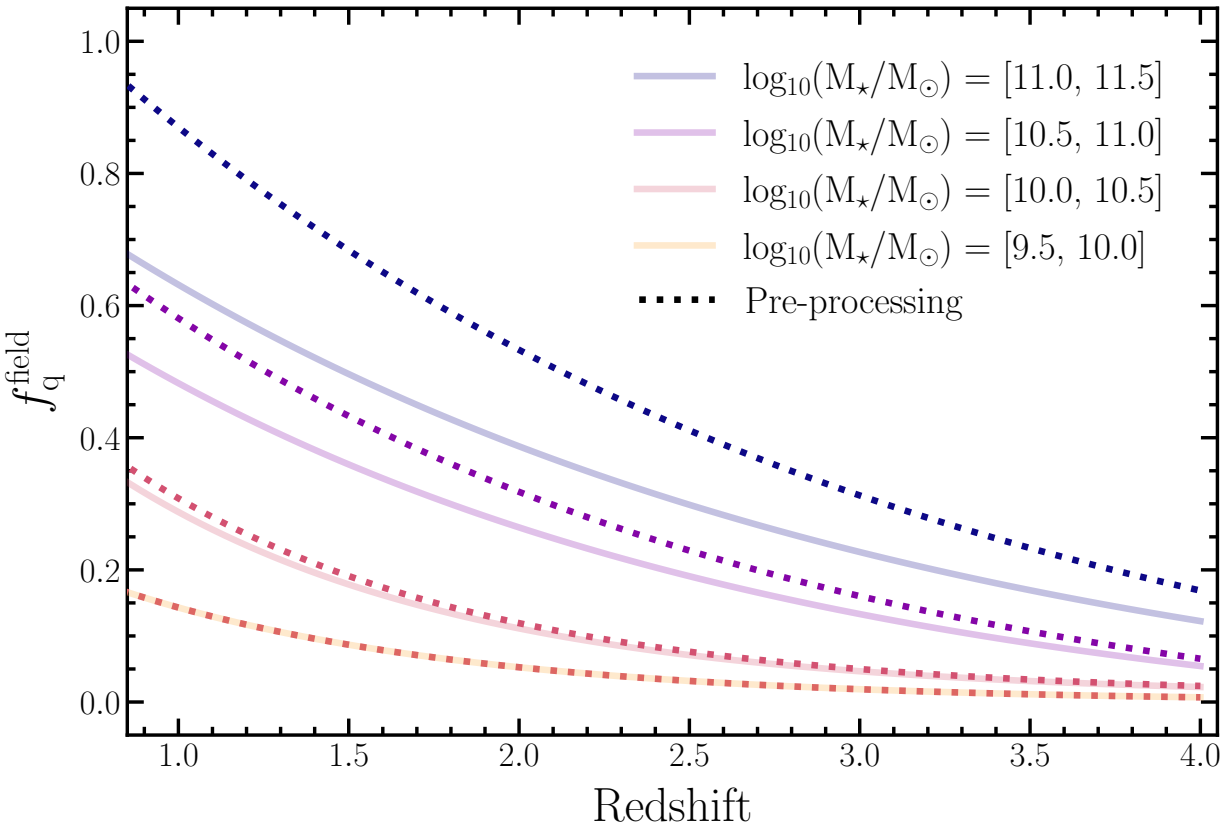

Figure 3.7: Field quenched fraction as a function of cosmic time and stellar mass. The faded lines represent our fits to the observed field quenched fraction from CANDELS (see Fig. 3.3). The dotted lines are the field quenched fraction results scaled to include the excess quenching due to additional satellite pre-processing in the infall regions of clusters. As discussed in §3.6.3, the scaling factor is derived from the measurement of the quenched fraction excess between the field and the infall region at $z \sim 1$ (Werner et al., 2022).

as a result of gas depletion in the absence of cosmological accretion following infall (Wheeler et al., 2014; Fillingham et al., 2015, 2016; Wetzel et al., 2015). As shown by Fillingham et al. (2015), the long satellite quenching timescales inferred for massive satellites in low-z groups and clusters ($M_{\rm halo} \sim 10^{12-15}$ M$_\odot$) significantly exceed the molecular gas depletion timescales for similar systems at $0 < z < 2$ (Bigiel et al., 2011; Saintonge et al., 2011; Tacconi et al., 2010, 2013, 2018; Freundlich et al., 2019). When factoring in the potential fuel supply associated with atomic gas, however, the dependence of $\tau_{\rm quench}$ on satellite stellar mass at $z \sim 0$ is shown to be in reasonably good agreement with the total cold gas (H_2 + HI) depletion timescale at $z \sim 0$ (Fillingham et al., 2015).

Measurements of the quenching timescale in lower-mass halos at $z \sim 1$ ($M_{\rm halo} \sim 10^{13-14}$ M$_\odot$) likewise yield timescales of $\sim 2-3$ Gyr at $M_\star \sim 10^{9.5-10.5}$ M$_\odot$ (Balogh et al., 2016; Fossati et al., 2017; Reeves et al., 2021, but see also Mok et al. 2013, 2014). This exceeds the timescale upon which mechanisms like ram-pressure stripping are expected to act (Tonnesen et al., 2007; Bekki, 2014) and also exceeds the molecular depletion timescale at the given mass scale and cosmic time (Genzel et al., 2010; Tacconi et al., 2018). Similarly, while our fiducial model yields rapid quenching at high satellite masses, the inferred quenching timescale at lower masses ($\sim 10^{10}$ M$_\odot$) is longer than the molecular depletion timescale ($t_{\rm depl} \sim 0.5-1$ Gyr) for field samples at $z \sim 1-2$. With that said, some measurements of CO-based molecular gas masses in $z > 1$ clusters do indicate that gas fractions (and depletion timescales) may be elevated in cluster populations (Noble et al., 2017, 2019; Hayashi et al., 2018). Other recent studies, however, find little variation in the molecular depletion timescale with environment (Rudnick et al., 2017; Williams et al., 2022) or argue for depressed gas levels and thus shorter depletion timescales in high-density environments (Alberts et al., 2022).

Including atomic gas as a potential fuel for star formation, our quenching model yields satellite quenching timescales in closer agreement to the total cold gas (H_2 + HI) depletion

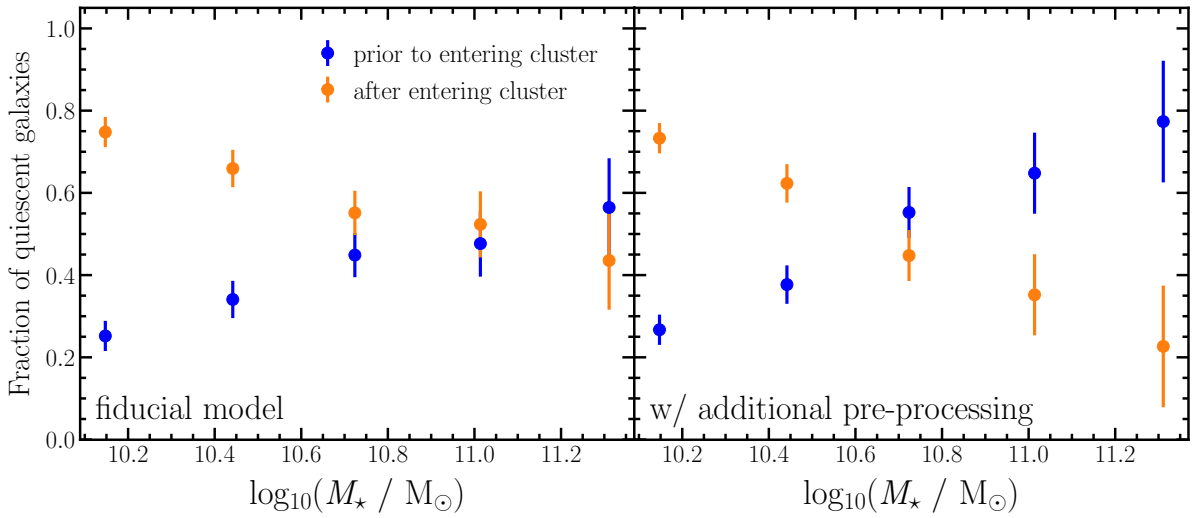

Figure 3.8: For the population of quiescent satellite galaxies in our model, we plot – as a function of stellar mass – the fraction of systems that were quenched prior to infall (blue points) versus quenched after infall (orange points) onto the cluster. The *left* panel shows results for our fiducial quenching model, while the *right* panel corresponds to results with additional pre-processing included (see §3.6.3). At the highest masses ($M_\star \gtrsim 10^{11}$ M$_\odot$), the majority of satellites are quenched prior to infall onto the cluster host halo, especially when accounting for pre-processing.

timescale at intermediate redshift. Given the typical infall time of our simulated sample, we include in Fig. 3.6 the atomic + molecular depletion timescale as a function of stellar mass from the semi-empirical modeling of the gas reservoirs of galaxies as a function of cosmic time (Popping et al., 2015). As found at $z \sim 0$, the relative agreement between the total cold gas depletion timescale and the satellite quenching timescale favors a scenario in which environmental quenching is driven by starvation. Moreover, similar to results at $z \sim 0$, where the satellite quenching timescale in groups and clusters shows little dependence on host halo mass for massive satellites (Wetzel et al., 2013), current measurements of $\tau_{\rm quench}$ at $z \sim 1$ point towards a relative lack of variation in satellite quenching efficiency with host halo mass (see §3.5.2; Balogh et al., 2016; Fossati et al., 2017). This further supports a picture in which satellite quenching is driven by starvation and follows a timescale dictated by the depletion of fuel for star formation following infall.

At high stellar masses, the cold gas (H_2 + HI) depletion timescale does exceed the quenching

timescale. However, it may be that the depletion timescales from Popping et al. (2015) overestimate the atomic fraction in these systems – as measurements of gas density in star-forming systems at intermediate redshift suggest a lower atomic component (e.g. Tacconi et al., 2013) and some simulations predict a decrease in the atomic fraction in high-mass galaxies at $z > 1$ (Davé et al., 2017). In addition, our model may underestimate the role of pre-processing that occurs prior to accretion, especially at high masses where increasing numbers of quenched ultra-massive galaxies have been identified in field surveys (e.g. Forrest et al., 2020a,b; Valentino et al., 2020; McConachie et al., 2021; Werner et al., 2022). As discussed in §3.6.3, including pre-processing within the infall regions surrounding our simulated clusters would lead to a corresponding lengthening of the satellite quenching timescale in Fig. 3.6, especially at $M_\star \gtrsim 10^{10.5}$ $M_\odot$. Another possibility is that complementary physical processes, such as ram-pressure stripping or feedback, are acting to decrease the reservoir of cold gas within satellites. Observations, both locally and at intermediate redshift ($z \lesssim 1$), find that stripping is clearly an active process in massive clusters (e.g. Poggianti et al., 2017; Vulcani et al., 2017; Boselli et al., 2019; Moretti et al., 2022). Alternatively, stripping can also lead to increases in the surface density of star formation activity in satellite systems (Merluzzi et al., 2013; Vulcani et al., 2018, 2020b), which could contribute to expediting starvation via feedback (McGee et al., 2014).

3.6.3 Role of Pre-Processing

Several studies of environmental quenching at low and intermediate z find that "pre-processing" plays an important role in the build up of quiescent galaxies (e.g. McGee et al., 2009; Cybulski et al., 2014; Hou et al., 2014; Just et al., 2019; Pallero et al., 2019; Sengupta et al., 2022). This occurs when a galaxy is subjected to environmental quenching as a consequence of becoming a satellite of a more massive galaxy prior to infall onto a group or cluster (or possibly via a filament, Sarron et al. 2019; Castignani et al. 2022). Our infalling satellite population is

modeled using the "field" quenched fraction from CANDELS (§3.4.2), such that our fiducial model includes some quenching due to pre-processing in lower-mass groups. This built-in level of pre-processing is most significant at lower satellites masses in our sample, where the fraction of satellite galaxies (relative to centrals) is greater.

Recent studies have attempted to quantify the role of pre-processing through measurements of the quenched fraction excess (QFE, van den Bosch et al. 2008), which is also referred to in the literature as the conversion factor or quenching efficiency and defined as

$$\mathrm{QFE}_{2-1} = \frac{f_{\mathrm{q},2} - f_{\mathrm{q},1}}{1 - f_{\mathrm{q},1}} \,, \tag{3.3}$$

where $f_{\mathrm{q},2}$ is the fraction of quenched galaxies in a given environment (e.g. the cluster regime) as compared to that in another environment (e.g. the field or infall region surrounding a cluster, $f_{\mathrm{q},1}$). In this context, a QFE of zero implies that there is no excess quenching between the two probed environments, while a QFE of one indicates that all star-forming galaxies in a given environment would be quenched were they to reside in the second (typically higher-density) environment.

Werner et al. (2022) presents a relevant and recent study of pre-processing for satellites of GOGREEN clusters at $0.8 < z < 1.4$ by computing the QFE between coeval cluster, infall (*inf*, $1 < R_{\mathrm{proj}}/R_{200} < 3$), and control (*con*) field samples. They find that $\mathrm{QFE}_{inf-con}$ strongly correlates with stellar mass, such that high-mass galaxies ($M_\star \sim 10^{11}$ $\mathrm{M}_\odot$) that are star forming in the field are more likely to be quenched in the infall regions relative to their lower-mass ($M_\star \sim 10^{10}$ $\mathrm{M}_\odot$) counterparts. To incorporate the impact of pre-processing in our quenching model, we scale our field quenched fraction as a function of redshift and stellar mass from Fig. 3.3 by the aforementioned $\mathrm{QFE}_{inf-con}(M_\star)$ results from Werner et al. (2022). As shown in Figure 3.7, this effectively augments the field quenched fraction of the most massive field galaxies (i.e. $M_\star = 10^{11-11.5}$ $\mathrm{M}_\odot$) as a function of redshift, such that a higher

fraction of high-mass galaxies are quenched prior to infall. At low-masses, the level of pre-processing is significantly less, with the field quenched fraction largely unchanged relative to that utilized in our fiducial model. As illustrated in Figure A.1 and A.2 in Appendix A.1, the quenching model is specifically tuned to reproduce the observed quenched fraction as a function of stellar mass, however, it also reproduces the correlation between the quenched fraction and projected cluster-centric radius and redshift within the GOGREEN survey.

As shown in Figure 3.8, including pre-processing increases the fraction of satellites that are quenched prior to infall onto the simulated clusters. This effect is most pronounced at higher stellar masses, with $\sim 65 - 80\%$ of simulated satellites quenched prior to infall at $M_\star > 10^{11}$ $M_\odot$ with the inclusion of pre-processing. In contrast to the results presented in Figure 8 from Werner et al. (2022), however, we do not find that $> 90\%$ of ultra-massive ($> 10^{11}$ $M_\odot$) galaxies are quenched prior to infall. In general, we find that the importance of pre-processing is likely weaker. In part, our results differ due to our more complete modeling of the accretion histories of satellite galaxies in our cluster sample. Comparing the quenched fractions of coeval populations via a measure of QFE partially ignores the evolution in those populations. Put simply, when compared to a sample of cluster members at $z \sim 1$, the coeval infall population does not represent the properties of the satellite population at the time of infall. Instead, a large fraction of the satellites in a cluster at $z \sim 1$ were accreted at $z \gtrsim 1.5 - 2$. Moreover, it is likely that our estimate of the quenched fraction for the "pre-processed" population of infalling satellites is slightly overestimated. Studies of the QFE within groups and clusters as a function of cosmic time suggest that QFE (at fixed stellar mass) decreases with increasing redshift (Lemaux et al., 2019; Sarron & Conselice, 2021). As such, by scaling our field quenched fractions by the $\mathrm{QFE}_{inf-con}$ at $z \sim 1$ from Werner et al. (2022), we likely overestimate the quenched fraction within infall regions at higher z. Similarly, a more complete analysis of the infall region would also factor in the contribution from quenched back-splash galaxies, which were quenched within the cluster but now reside within the infall regions (e.g. Balogh et al., 2000; Gill et al., 2005; Fillingham et al., 2018).

By accounting for pre-processing in our quenching model, we find that the best-fit quenching timescale is less strongly dependent upon stellar mass as shown in Fig. 3.9. At all masses, the inferred quenching timescale exceeds the typical depletion timescale for molecular gas. In Fig. 3.9, we illustrate the median molecular depletion timescale as a function of stellar mass for our simulated infalling satellite population based on the measured mass and redshift dependence of the depletion timescale for galaxies on the star-forming main sequence from Tacconi et al. (2018), adopting the relationship between star formation rate and stellar mass from Speagle et al. (2014). For comparison, we also include the empirically-derived H_2 + HI gas depletion timescale for galaxies at $z = 1.5$ from Popping et al. (2015). The predicted cold gas depletion timescale depends on redshift at $1 < z < 2$, decreasing with increasing z over the redshift range where a large fraction of our simulated satellite population is accreted. With pre-processing included in our model, the resulting satellite quenching timescale at $z \sim 1$ is in relatively good agreement with the cold gas (H_2 + HI) depletion timescale at intermediate redshift, similar to results at $z \sim 0$ (Fillingham et al., 2015) and consistent with starvation as the dominant mechanism for satellite quenching.

3.6.4 Impact of Stellar Mass Estimation

As discussed in §3.3.2, our fiducial model makes use of stellar masses from TNG that are defined to include the sum of all star+wind particles gravitationally bound to a given galaxy. A minor change would be to define stellar masses as the sum of all gravitationally bound star+wind particles within twice the stellar half-mass radius. We find that this change simply shifts the stellar masses lower by an average of ~ 0.1 dex, but it does not significantly modify the results from the fiducial model. As shown in Fig. 3.2, our fiducial model reproduces the relative distribution of satellite stellar masses for both the star-forming and quenched populations within GOGREEN.

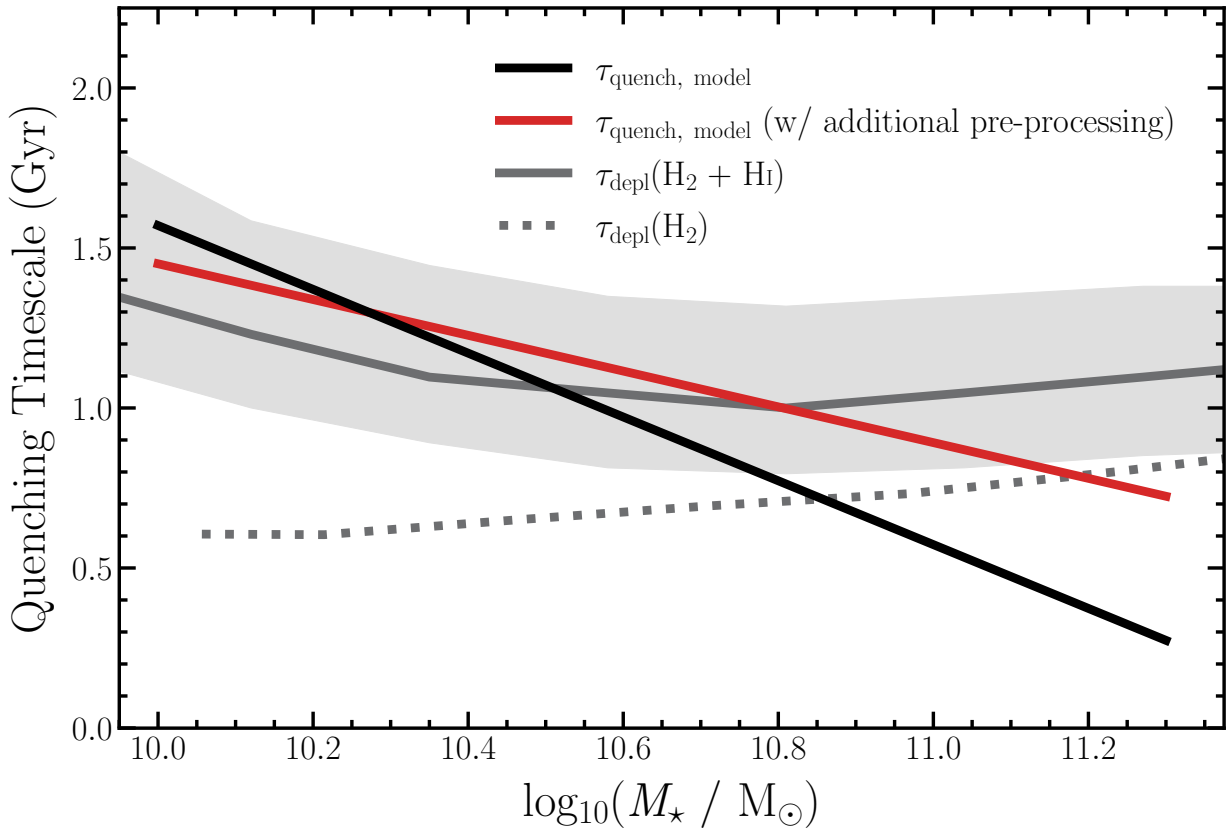

Figure 3.9: Quenching timescale versus stellar mass. The black solid line represents the quenching timescale results from our fiducial model, while the crimson line shows the results from our model including additional pre-processing (see §3.6.3). The solid grey line illustrates the empirically-derived cold gas (HI + H_2) depletion timescale from Popping et al. (2015) at $z \sim 1.5$, with the grey shaded region corresponding to the variation in the depletion timescale over the redshift range $1 < z < 2$. Finally, the dotted grey line denotes the median molecular depletion timescale for our simulated infalling satellite population based on the scaling relations of Tacconi et al. (2018). Including additional pre-processing, we find a quenching timescale that is less strongly dependent on satellite stellar mass and is roughly consistent with the estimated cold gas (H_2 + HI) depletion timescale at $z \sim 1 - 2$.

Another aspect of our model is that it effectively defines crude star formation histories (SFHs) for the simulated satellites (e.g. explicitly determining when particular systems quench); these SFHs may thereby differ from those within the TNG hydro-dynamical simulation, which are closely coupled to the stellar masses. Therefore, an alternative approach, which would more fully decouple our results from the prescriptions of baryonic physics utilized within TNG, is to define our simulated satellite stellar masses according to the assumption of a stellar mass-halo mass (SMHM) relation. We accomplish this using the Behroozi et al. (2013) SMHM relation which estimates the stellar masses of galaxies using their peak halo mass and corresponding redshift. Compared to the TNG masses utilized in our fiducial model, the stellar masses inferred from the Behroozi et al. (2013) SMHM relation are systematically less massive (by a few tenths of a dex). This bias towards lower masses is partially driven by a lack of ultra-massive galaxies ($> 10^{11}$ $M_{\odot}$) predicted via abundance matching. Consequently, the observed distribution of satellite stellar masses from GOGREEN is not reproduced when assuming the Behroozi et al. (2013) SMHM relation, in contrast to our fiducial model. However, when inferring stellar masses via abundance matching, we find that the resulting satellite quenching timescales – $\tau_{\rm quench}(M_{\star})$ – are only slightly shorter (by $\sim 0.1 - 0.2$ Gyr) relative to those of our fiducial model.

3.6.5 Success of Our Model

Overall, our satellite quenching model reproduces many of the major observables from the GOGREEN survey – the quenched fraction as a function of stellar mass (by construction), projected cluster-centric radius, and redshift. As a result, our model also reproduces the measured QFE as a function of stellar mass from van der Burg et al. (2020). Finally, our model likewise yields the observed stellar mass functions for both star-forming and quenched systems (van der Burg et al., 2020). As shown in Figure 3.2, our model reproduces the relative distribution of galaxy stellar masses for the quenched and star-forming populations

in comparison to the corresponding observed counts from GOGREEN. With respect to the normalization of the resulting mass functions, our model underpredicts the total number of satellites due to our simulated clusters being biased towards lower halo masses (see Fig. 3.1). As discussed in §3.3.1, however, the distribution of infall times for our simulated satellites is weakly dependent on host halo mass (at $z > 1$ and $10^{14} < M_{\rm halo}/{\rm M}_{\odot} < 10^{15}$), such that an increase in the number of satellites would not impact our measured satellite quenched fractions (i.e. the results of the model).

While a quantitative comparison is beyond the scope of this work, the relatively short satellite quenching timescales (thus efficient environmental quenching) inferred by our modeling would yield older stellar ages and less extended SFHs for the GOGREEN cluster population relative to field galaxies of the same stellar mass. This is in agreement with recent results from Webb et al. (2020), which find that satellites within the GOGREEN clusters are typically ~ 0.3 Gyr older than their field counterparts, with less extended SFHs. In addition, measurements of galaxy morphologies within the GOGREEN clusters find an excess of quiescent disks, particularly at low stellar masses (Chan et al., 2021), which is also consistent with our results. Suppressing star formation via starvation will preferentially yield disky systems relative to processes such as mergers or harassment (e.g. Mastropietro et al., 2005; Cortese et al., 2007). As found in the observations, within our model, the difference between the field and cluster morphologies should be most significant at lower satellite masses, where the environment plays a greater role in quenching (e.g. see Fig. 3.8).

Altogether, our model of satellite quenching is remarkably successful. In contrast, modern simulations of galaxy evolution tend to greatly overproduce the quenched satellite population at intermediate redshift, particularly at lower satellite masses (Donnari et al. 2021; Kukstas et al. in prep). This over-quenching problem is a long-standing one (e.g. Font et al., 2008; Kimm et al., 2009; Weinmann et al., 2012; Hirschmann et al., 2014; Wang et al., 2014; Bahé et al., 2017), though progress has been made recently in reproducing observations of groups

and clusters at $z \sim 0$ (e.g. De Lucia et al., 2019a; Xie et al., 2020; Donnari et al., 2021).

3.7 Summary and Conclusions

Using simulated cluster and satellite populations from TNG, we model the quenching of satellite galaxies at $z > 1$ in comparison to observations from the GOGREEN survey. The model includes one primary parameter, the satellite quenching timescale ($\tau_{\rm quench}$) that sets the time that a satellite remains star forming after infall onto the cluster. This timescale is tuned as a function of stellar mass to reproduce the observed satellite quenched fraction as a function of stellar mass. The main results from this modeling effort are as follows:

1. We measure the quenched fraction of GOGREEN cluster members as a function of stellar mass, projected cluster-centric radius, and redshift. We find that the satellite quenched fraction increases with stellar mass, decreases with projected radial cluster-centric separation, and remains relatively flat with redshift.

2. Our model reproduces the observed quenched fraction as a function of stellar mass (by construction), projected cluster-centric radius, and redshift as measured at $z \sim 1$ from the GOGREEN survey. In addition, our quenching model reproduces the relative galaxy stellar mass distribution (both in the field and in the cluster) as a function of galaxy type (star forming versus quenched).

3. In agreement with van der Burg et al. (2020), we find that satellite quenching is mass dependent at $z \sim 1$, in conflict with models that favor mass-independent environmental quenching (e.g. Peng et al., 2010). For our fiducial model, the quenching timescale depends on satellite stellar mass, such that galaxies at $M_\star = 10^{10}$ $\rm M_\odot$ typically quench

within $\sim$ 1.6 Gyr following infall, while galaxies at $M_\star = 10^{11}$ $M_\odot$ quench much more rapidly (within $\sim$ 0.6 Gyr). Including pre-processing within the infall regions of clusters, the dependence of $\tau_{\rm quench}$ on satellite stellar mass weakens slightly, with satellites typically quenching on timescales of $\sim 1 - 1.5$ Gyr post infall, depending on mass.

4. In comparison to similar analyses at low redshift, we find that the satellite quenching timescale evolves roughly like the dynamical time ($\propto (1+z)^{-3/2}$), as noted by several previous studies (Tinker & Wetzel, 2010; Balogh et al., 2016; Foltz et al., 2018).

5. When including pre-processing within the cluster infall regions, we find that the vast majority ($\sim 65 - 80\%$) of massive satellites ($> 10^{11}$ $M_\odot$) in clusters are quenched at $z \sim 1$ clusters prior to infall. In contrast, the majority of lower-mass satellites ($\lesssim 10^{10.5}$ $M_\odot$) quenched within the cluster.

6. Our satellite quenching model yields quenching timescales that are longer than the observed molecular depletion timescales at intermediate redshift. Instead, the inferred quenching timescales are roughly consistent with the predicted total cold gas depletion timescale (HI+ H_2) at $1 < z < 2$. Similar to the results of modeling satellite populations in the local Universe, this may indicate that environmental quenching at $z > 1$ is primarily driven by starvation, where galaxies exhaust their fuel supply for star formation after being cut off from cosmological accretion.

Chapter 4

When the Well Runs Dry: Modeling Environmental Quenching in Massive Clusters at $z \gtrsim 1$

Your assumptions are your windows on the world. Scrub them off every once in a while, or the light won't come in.

– Alan Alda

4.1 Introduction

Environmental studies in the local Universe and extending out to $z \sim 2$ have found that galaxies that are members of massive galaxy groups and clusters – i.e. satellites – are more likely to be passive (or quenched) relative to their counterparts of similar mass in the low-density field (Oemler, 1974; Dressler, 1980; Balogh et al., 1997; Gómez et al., 2003; Baldry

et al., 2006; Cooper et al., 2006, 2007, 2010a; Guo et al., 2017; Lee-Brown et al., 2017; Ji et al., 2018; Lemaux et al., 2019; Pintos-Castro et al., 2019; Shi et al., 2021; McConachie et al., 2021). It has long been understood that satellite galaxies – by virtue of their environment – are uniquely subject to a variety of environmental quenching mechanisms (e.g. Baldry et al., 2006; Peng et al., 2010, 2012) that suppress star formation by way of (*i*) gas depletion without replenishment or (*ii*) stripping and removal of cold gas (i.e. the fuel for star formation). Two of the leading environmental quenching candidates that satisfy these conditions include "starvation" (Larson et al., 1980; Bekki et al., 2002; Kawata & Mulchaey, 2008) – the *slow* depletion of cold gas in the absence of cosmological accretion after a galaxy becomes a satellite of a massive host – and "ram-pressure stripping" (RPS; Gunn & Gott, 1972; Abadi et al., 1999; Poggianti et al., 2017) – the *rapid* removal of cold gas from the interstellar medium of a satellite as it moves through the dense intra-group or intracluster medium permeating the host halo. Other potential environmental quenching mechanisms include gravitationally-driven processes such as tidal stripping (Merritt, 1983; Moore et al., 1999; Gnedin, 2003), mergers (Lavery & Henry, 1988; Makino & Hut, 1997; Gottlöber et al., 2001), and galaxy harassment via high-speed impulsive encounters (Farouki & Shapiro, 1981; Moore et al., 1996, 1998) – as well as "outflow-based" processes such as overconsumption (McGee et al., 2014; Balogh et al., 2016).

Although these mechanisms primarily impact fully accreted satellites, several studies have shown that galaxies can undergo "group pre-processing" (Fujita, 2004; De Lucia et al., 2012; Wetzel et al., 2015; Bianconi et al., 2018; Sarron et al., 2019; Werner et al., 2022), wherein they quench within a more massive halo prior to becoming a satellite of the final group or cluster. Thus, understanding the dominant driver of environmental quenching is challenging, as it entails making assumptions regarding the relative contributions of pre-processed satellite galaxies to the observed quiescent fraction. Moreover, an additional challenge is that environment-independent quenching processes (often referred to as "mass quenching" or "self-quenching", Peng et al., 2010) may be dominant, particularly for massive galaxies

(e.g. Tacchella et al., 2015; Reeves et al., 2021; Werner et al., 2022). Such mechanisms, including feedback from star formation (Oppenheimer & Davé, 2006; Ceverino & Klypin, 2009), supernovae (Springel et al., 2005; Lagos et al., 2013), and active galactic nuclei (Di Matteo et al., 2005; Croton et al., 2006; Hopkins et al., 2006), are capable of quenching galaxies prior to them becoming fully incorporated into a galaxy group or cluster.

At present, our current understanding of the dominant quenching mechanism driving environmental quenching in galaxy groups and clusters is largely limited to the very local ($z < 0.1$) Universe (e.g. De Lucia et al., 2012; Wetzel et al., 2013; Hirschmann et al., 2014; Wheeler et al., 2014; Fillingham et al., 2015, 2016, 2018; Davies et al., 2016; Pallero et al., 2019; Rodriguez Wimberly et al., 2019b; Baxter et al., 2021). In fact, our best cosmological models routinely fail to reproduce the observed fraction of quenched satellites as a function of stellar mass beyond the local Universe, signaling that our current prescriptions for environmental quenching are incomplete at intermediate and high redshift (e.g. Guo et al., 2010; Hirschmann et al., 2014; De Lucia et al., 2019b; Xie et al., 2020; Donnari et al., 2021; Kukstas et al., 2023).

In our recent work (Baxter et al., 2022, hereafter B22), we built upon previous efforts to constrain the dominant quenching mechanism in massive clusters at $z \sim 1$ (e.g. Muzzin et al., 2014; Balogh et al., 2016; Foltz et al., 2018) by constraining the timescale ($\tau_{\rm quench}$) upon which satellite quenching proceeds following infall. Given that different mechanisms operate on distinct timescales, knowledge of $\tau_{\rm quench}$ at a given epoch can aid in distinguishing the underlying quenching mechanism at play (e.g. Wetzel et al., 2014; Fillingham et al., 2015; Wright et al., 2019; Park et al., 2022). In B22, we accomplish this by developing an infall-based environmental quenching model – with prescriptions for "field quenching" (i.e. self-quenching in the field) and "pre-processing" – that infers the quenching timescale consistent with the observed satellite quiescent fraction as a function of stellar mass as measured in 14 massive clusters ($M_{\rm halo} = 10^{14-15}$ M$_\odot$) from the GOGREEN survey (Balogh et al., 2021) –

the hitherto largest and most comprehensive spectroscopic and multi-passband photometric cluster and group survey at $z \gtrsim 1$. Many of the conclusions drawn in B22 are consistent with results from previous GOGREEN studies (Webb et al., 2020; Reeves et al., 2021; McNab et al., 2021), including that (*i*) the majority of massive galaxies ($M_\star \gtrsim 10^{10.5}$ $M_\odot$) quench before they become cluster members and (*ii*) low-mass galaxies are preferentially quenched after infall. In addition, the analysis presented in B22 finds that the satellite quenching timescale at $z \sim 1$ is in good agreement with the estimated cold gas (HI+H_2) depletion timescale, suggesting that starvation may be the dominant quenching mechanism within GOGREEN clusters.

While the modeling from B22 suggests that the inferred satellite quenching timescale in massive clusters is consistent with starvation being the dominant driver of environmental quenching at $z < 2$, there is a wealth of literature showing that RPS is an active process in cluster environments in the nearby Universe (Yagi et al., 2007; Boselli et al., 2016b; Gavazzi et al., 2018; Moretti et al., 2018; Vulcani et al., 2018; Poggianti et al., 2019; Gullieuszik et al., 2020; Luber et al., 2022). Moreover, recent observational studies find direct evidence of satellites in clusters at $z \sim 0.7 - 1.6$ suffering from RPS (Boselli et al., 2019; Noble et al., 2019; Matharu et al., 2021; Cramer et al., 2022), while simulations find that RPS should be effective in cluster environments up to $z \sim 2$ (see review from Boselli et al., 2022). Given that the efficiency of RPS depends directly on the density of the intracluster medium (ICM) – i.e. higher near the core of a cluster – we generalize the environmental quenching model developed in B22 to include the radius at which quenching begins ($R_{\rm quench}$) as a free parameter. In addition, we explore model results regarding where within the cluster and with what velocity satellites quench. These modifications permit the exploration of potentially distinct quenching pathways, by no longer assuming that environmental quenching begins immediately after crossing R_{200}, allowing us to test whether or not the main conclusion drawn in B22 – i.e. whether starvation is the dominant quenching pathway at $z < 2$ – is robust to changes in our modeling regarding where in a cluster environmental quenching

becomes effective.

In §4.2 and §4.3 of this work, we describe our observed galaxy cluster sample and our simulated satellite population, respectively – leaving details regarding cluster membership criteria to B22. In §4.4, we describe our updated environmental quenching model, with the results from our MCMC analysis and comparison of model predictions with observed properties of transition galaxies presented in §4.5. In §4.6, we discuss our procedure for isolating distinct quenching pathways and contextualize our results with respect to previous studies at $z \sim 1$. Finally, in §4.7 we summarize our investigation and present our conclusions. When necessary, we adopt a flat ΛCDM cosmology with $H_0 = 70$ km s^{-1} Mpc^{-1} and $\Omega_m = 0.3$ as well as a Chabrier (2003) initial mass function. All magnitudes are on the AB system (Oke & Gunn, 1983).

4.2 Observed Cluster Sample

4.2.1 GOGREEN and GCLASS Cluster Sample

We select our cluster sample from the Gemini CLuster Astrophysics Spectroscopic Survey (GCLASS) and the Gemini Observations of Galaxies in Rich Early ENvironments (GOGREEN) surveys (Muzzin et al., 2012; Balogh et al., 2017, 2021).[1] The main focus of these surveys is to study galaxy evolution in high-density environments by combining deep, multi-wavelength photometry with extensive Gemini/GMOS (Hook et al., 2004) spectroscopy of galaxies in 26 overdense systems over a redshift range of $0.867 < z < 1.461$. For the purposes of our investigation, we select 14 massive clusters with halo masses in the range $10^{13.8-15}$ M$_\odot$ and spectroscopic redshifts of $0.867 < z < 1.368$. Eleven of these clusters were selected from the Spitzer Adaptation of the Red-sequence Cluster Survey (SpARCS, Wilson

[1] http://gogreensurvey.ca/data-releases/data-packages/gogreen-and-gclass-first-data-release/

Name	M_{200} [10^{14} $M_\odot$]	R_{200} [cMpc]	σ [km s^{-1}]	z	$N_{\rm members}$ [$> 10^{10}$ $M_\odot$]
SpARCS0034	0.6	1.08	700 ± 150	0.867	23
SpARCS0035	3.8	2.17	840 ± 50	1.335	18
SpARCS0036	3.6	2.09	750 ± 90	0.869	45
SpARCS0215	2.4	1.70	640 ± 130	1.004	34
SpARCS0335	1.8	1.59	540 ± 30	1.368	7
SpARCS1047	2.5	1.78	660 ± 120	0.956	26
SpARCS1051	2.2	1.80	690 ± 40	1.035	26
SpARCS1613	11.1	2.97	1350 ± 100	0.871	68
SpARCS1616	3.3	1.98	780 ± 40	1.156	39
SpARCS1634	2.7	1.85	715 ± 40	1.177	34
SpARCS1638	1.7	1.56	565 ± 30	1.196	20
SPT0205	3.1	1.77	680 ± 60	1.323	19
SPT0546	5.8	2.42	980 ± 70	1.067	27
SPT2106	7.3	2.62	1055 ± 85	1.131	30

Table 4.1: Properties of our GOGREEN cluster sample, including M_{200}, R_{200}, velocity dispersion, cluster redshift, and the number of spectroscopic members (with $M_\star > 10^{10}$ $M_\odot$). The values in the R_{200} and M_{200} columns were obtained using the MAMPOSSt method (Mamon et al., 2013) as outlined in Biviano et al. (2021). Details regarding the cluster membership criteria are discussed in §4.2.2. Details regarding the total number of members used to measure the velocity dispersion is provided in Table 1 of Balogh et al. (2021).

et al., 2009; Muzzin et al., 2009; Demarco et al., 2010), where they were detected in shallow z' and *Spitzer*/IRAC 3.6μm images due to their overdensity of red-sequence galaxies (Gladders & Yee, 2000). The remaining three clusters were drawn from the South Pole Telescope (SPT) survey (Brodwin et al., 2010; Foley et al., 2011; Stalder et al., 2013) and were initially detected via their Sunyaev-Zeldovich (Sunyaev & Zeldovich, 1970) signature and later spectroscopically confirmed. Table 4.1 lists the properties of our cluster sample including halo mass (M_{200}) and radial scale (R_{200}) – which are both obtained using the MAMPOSSt method (Mamon et al., 2013) as outlined in Biviano et al. (2021).

4.2.2 Cluster Membership and Classification

We define our initial satellite population to consists of all objects – excluding the central – within R_{200} (projected) of a given cluster and with a stellar mass $M_\star > 10^{10}$ M$_\odot$ – i.e. the $\sim 80\%$ stellar mass completeness limit for the photometric sample (van der Burg et al., 2020). In addition, for objects with a secure spectroscopic redshift (Redshift_Quality[2] = 3,4), we limit our satellite population to those systems with $|z_{\rm spec} - z_{\rm cluster}| \leq 0.02(1 + z_{\rm spec})$. Meanwhile, for sources without a secure spectroscopic redshift, we define the members of the satellite population as those systems with STAR $\neq 1$ and $|z_{\rm phot} - z_{\rm cluster}| \leq 0.08(1 + z_{\rm phot})$, where the STAR flag is the GOGREEN star/galaxy classification based on color selection as described in van der Burg et al. (2020). As discussed in B22, the photometric redshift selection was informed by our knowledge that the $z_{\rm phot}$ uncertainty for galaxies more massive than 10^{10} M$_\odot$ is $0.048(1 + z)$. Nevertheless, we find that if we subsequently characterize and account for interlopers and incompleteness, as described in §4.2.3, the results of our analysis do not depend on the Δz threshold adopted as part of this particular membership criterion. Altogether, these membership selection criteria yield a total of 1072 cluster members (416 spectroscopic/656 photometric). Lastly, we classify the quiescent members of our cluster

[2]Please refer to Balogh et al. (2021) for a description of the redshift quality flags and the assignment process.

population using the following rest-frame UVJ color-color cuts defined by Whitaker et al. (2011, see also Williams et al. 2009):

$$\begin{aligned}(U-V) > 1.3 \ \cap \ (V-J) < 1.6 \ \cap \\ (U-V) > 0.88 \times (V-J) + 0.59 \ .\end{aligned} \tag{4.1}$$

4.2.3 Completeness Correction

Following the methodology utilized in van der Burg et al. (2013, 2020), we apply a completeness correction to account for incompleteness and interlopers that contaminate our photometric sample. To accomplish this, we compute a membership correction factor based on the subset of galaxies that have both multi-band photometry and spectroscopic redshift measurements, and subsequently apply this factor to the photometric sample. The membership correction factor (Eqn. 4.2) is defined as the sum of the number of galaxies that are either secure cluster members and false negatives divided by the sum of the number of secure cluster members and false positives,

$$C_{\text{factor}} = \frac{N(\text{secure cluster}) + N(\text{false negative})}{N(\text{secure cluster}) + N(\text{false positive})} \ . \tag{4.2}$$

Secure cluster members are objects with spectroscopic *and* photometric redshifts that are consistent with cluster membership. False negatives, on the other hand, refer to objects that are spectroscopically confirmed as cluster members but have photometric redshifts inconsistent with cluster membership. Conversely, false positives are objects that are not cluster members based on their spectroscopic redshift, yet exhibit photometric redshifts consistent with the redshift of the cluster.

To account for the presumed color dependence of field contamination, we separately compute

the correction factor for star-forming and quiescent galaxies. Moreover, we compute the correction factor within bins of stellar mass (ranging from $10^{10.0-11.4}$ $M_\odot$) and $R_{\rm proj}/R_{200}$ (ranging from 0 to 1) for both galaxy populations. Notably, we observe a negligible variation in the completeness correction with respect to galaxy color, as the correction factor applied to star-forming and quiescent populations differs by less than 2%.

Lastly, we apply the appropriate correction factor as a weight to each cluster member. This adjustment leads to a modest change in the measured quenched fractions ($\sim 1 - 2.5\%$). Importantly, this completeness correction has no bearing on the final results of our analysis or the conclusions drawn, as they remain consistent irrespective of its application.

4.3 Simulated Cluster Sample

4.3.1 IllustrisTNG Cluster Sample

As in B22, we once again construct our simulated cluster population – which is matched on redshift to our observed cluster sample – using the TNG300-1 simulation from the IllustrisTNG project[3] (TNG, Nelson et al., 2018; Naiman et al., 2018b; Springel et al., 2018; Pillepich et al., 2018; Marinacci et al., 2018). TNG300-1 is a large volume (~ 300 cMpc^3), high-resolution (2×2500^2 resolution elements), cosmological, gravo-magnetohydrodynamical simulation that utilizes the moving mesh `AREPO` code and solves for the coupled evolution of dark matter, cosmic gas, luminous stars, and supermassive black holes from a starting redshift of $z = 127$ to the present day, $z = 0$. TNG300-1 has a dark matter (gas) mass resolution of $m_{\rm DM} = 5.9 \times 10^7$ $M_\odot$ ($m_{\rm baryon} = 1.1 \times 10^7$ $M_\odot$), which corresponds to a halo mass (stellar mass) completeness of $\sim 10^{10}$ $M_\odot$ ($\sim 10^9$ $M_\odot$). As explained in §3.3 of Pillepich et al. (2018), we augment the stellar masses for TNG300-1 galaxies at $z \sim 1$ by a factor of

[3]https://www.tng-project.org

1.3× to account for resolution limitations that systematically underestimate stellar masses within the simulations.

Our simulated cluster population consists of 56 unique clusters drawn from snapshots that range from $z = 1.36$ to $z = 0.85$ with a median redshift of $z = 1.1$, where the median redshift difference between an observed cluster and its simulated analog is $|\Delta z| \sim 0.03$. In an effort to avoid repetition, please refer to §3.1 of B22 for specific details on how the simulated clusters are selected to match the redshift distribution of our observed cluster sample.

4.3.2 Satellite Membership in Simulated Cluster Population

We apply the exact cluster membership criteria as described in section §3.2 of B22; please refer to this work for a more detailed description of our membership selection procedure. In short, our simulated satellite population consists of objects that satisfy the following conditions: (*i*) located within R_{200} of a given cluster as measured at the redshift of observation ($z_{\rm obs}$) and (*ii*) objects with resolution-corrected stellar mass of $M_\star > 10^{10}$ $\rm M_\odot$ measured at $z_{\rm obs}$ – where the stellar masses are given by the total mass of all star particles associated with each galaxy (i.e. IllustrisTNG Subhalo-MassType masses with Type=4). Our final simulated cluster population includes 1220 cluster members across the 56 simulated clusters. Though our simulated cluster sample is comprised of more hosts than the observed cluster sample, the former is biased towards less-massive systems ($M_{\rm halo} < 10^{14.3}$ $\rm M_\odot$) – see figure 1 of B22. However, as discussed in §3.1 of B22, this bias towards low-mass hosts has a negligible impact on our results due to there being a weak dependence between the distribution of satellite infall times (at fixed stellar mass) and host halo mass.

4.4 Modeling Environmental Quenching

4.4.1 Updated Environmental Quenching Model

In our previous work B22, we developed an infall-based environmental quenching model to constrain the quenching timescale required to reproduce the satellite quiescent fraction versus satellite stellar mass trend as measured in our aforementioned observed cluster sample. The updated environmental quenching model developed in this investigation shares many similarities with the original model in that it (*i*) accounts for the contribution from "field quenching" in the simulated cluster population using the coeval field quenched fraction measurements derived from the Cosmic Assembly Near-Infrared Deep Extragalactic Legacy Survey (CANDELS, Grogin et al., 2011; Koekemoer et al., 2011; Guo et al., 2013; Galametz et al., 2013; Santini et al., 2015; Stefanon et al., 2017; Nayyeri et al., 2017; Barro et al., 2019) – for more details, see §4.2 of B22; (*ii*) incorporates the contributions from satellite pre-processing (Fujita, 2004; De Lucia et al., 2012; Werner et al., 2022; Salerno et al., 2022) in the infall region ($1 - 3\ R_{200}$) of the clusters – for more details, see §6.3 of B22; and (*iii*) implements an infall-based environmental quenching model in which quenching of the simulated satellites occurs some time $\tau_{\rm quench}$ after the first crossing of R_{200} – for more details, see §4.3 of B22. The model proved to be highly successful, reproducing the observed satellite stellar mass function and satellite quenched fraction trends – i.e. the satellite quenched fraction as a function of stellar mass, projected host-centric radius, and redshift – associated with our observed cluster population at $z \gtrsim 1$. The inferred satellite quenching timescale was found to be mass-dependent and consistent with the empirically-derived cold gas (HI + H_2) depletion timescale at intermediate z from Popping et al. (2015), suggesting that starvation is the dominant quenching mechanism at $z < 2$.

The objective of the investigation herein is to test the validity of the aforementioned conclusion by developing a generalized model for environmental quenching that allows $R_{\rm quench}$ – i.e.

the radius at which quenching, and therefore the clock measuring $\tau_{\rm quench}$, is assumed to begin – to vary as a free parameter. While some environmental quenching studies use estimates of the virial radius of the host halo (e.g. R_{200}) as the physical location at which environmental quenching begins (e.g. Balogh et al., 2000; Fillingham et al., 2018), it has been found that both cold gas stripping and the removal of diffuse gas from the circumgalactic medium of a galaxy can begin to occur beyond R_{200} (Bahé et al., 2013; Cen et al., 2014; Zhang et al., 2019; Ayromlou et al., 2021). As mentioned above, our original model accounts for this scenario by allowing quenching to occur in the infall regions (1–3 R_{200}) of our clusters – see §6.3 of B22 for a description of how this is implemented in our model. Furthermore, certain environmental quenching mechanisms are simply more efficient at smaller host-centric radii – e.g. RPS is most efficient near pericenter (Cortese et al., 2021; Boselli et al., 2022). Therefore, by imposing the condition that $R_{\rm quench} = 1.0\ R_{200}$, the environmental quenching model developed in B22 neglects potentially important regions of parameter space, thereby potentially overlooking alternative quenching pathways. The impact of including $R_{\rm quench}$ as a free model parameter is that, under the assumption that satellite orbits are *not* exclusively radial, it allows the model to potentially explore quenching pathways distinct from the "special case" assumed in B22. Should the aforementioned assumption be invalid, our model would suffer from a severe degeneracy between $R_{\rm quench}$ and $\tau_{\rm quench}$, limiting the amount of new information that could be gained from adding the quenching radius as a free parameter. Additionally, distinguishing between a slow quenching process and a long delay time followed by rapid quenching would be challenging. However, if the satellite galaxies exhibit a mix of orbital anisotropies, which perhaps depend on mass and redshift, this degeneracy can be partially broken.

Another modification is the inclusion of the condition that environmental quenching can only occur at $z < 2.5$, so as to allow for the formation of a hot halo or dense ICM whereby mechanisms such as starvation and RPS can thereby effectively act to quench cluster members. In other words, it is difficult to explain how potential environmental quenching mechanisms

could effectively operate prior to the emergence of massive, virialized halos with a hot or dense ICM. In practice, this constraint potentially allows for a small fraction of satellites ($\lesssim 7\%$) that are accreted prior to $z = 2.5$ to quench almost immediately after this condition is satisfied.

Finally, we now also perform a comprehensive Monte Carlo Markov Chain (MCMC) analysis using the `emcee` ensemble sampler package (Foreman-Mackey et al., 2013). This step is included to ensure that the parameter space associated with the updated environmental quenching model is thoroughly explored, with the primary parameters being the radius at which environmental quenching begins ($R_{\rm quench}$) along with the slope (m) and y-intercept (b) of the satellite quenching timescale ($\tau_{\rm quench}$) that we allow to vary linearly with satellite stellar mass, as defined below:

$$\tau_{\rm quench} = m * \log_{10}(M_\star/{\rm M}_\odot) + b. \tag{4.3}$$

Given that our model inherently accounts for quenching in the infall region ($1 - 3\ R_{200}$), we limit $R_{\rm quench} < 1.0\ R_{200}$. Furthermore, we apply uniform priors to all model parameters and define the log likelihood function as

$$\begin{aligned} &\ln\, p(y \,|\, R_{\rm quench}, m, b, f) = \\ &\quad -\frac{1}{2}\sum_{i=1}^{N}\left[\frac{(y_{i,\rm obs} - y_{i,\rm model})^2}{s_i^2} + \ln\left(2\pi\, s_i^2\right)\right], \end{aligned} \tag{4.4}$$

where

$$s_i^2 = \sigma_i^2 + f^2 y_{i,\rm model}^2\,.$$

Thus, our chosen likelihood function is a Gaussian where the observed variance (σ_i^2) is assumed to be underestimated by a fractional amount f in order to account for the possibility

that the uncertainties *are not* Gaussian[4] and uncorrelated. Lastly, $y_{\rm obs}$ and $y_{\rm model}$ are 1D vectors that contain, respectively, the observed and predicted satellite quenched fractions binned as a function of satellite stellar mass, host-centric radius, and redshift. In the following section, we discuss the results from our Bayesian inference analysis.

4.5 Results

4.5.1 MCMC Analysis & Competing Solutions

As a reminder, the two primary parameters of our environmental quenching model are the host-centric radius where quenching begins ($R_{\rm quench}$) and the time – as measured from $R_{\rm quench}$ – required for satellites to environmentally quench ($\tau_{\rm quench}$). The utility of this model is that by using the infall histories of our simulated satellite population we are able to predict the quiescent fraction as a function of satellite stellar mass, host-centric radius, and redshift. Thus, the goal of this Bayesian inference analysis is to determine the model parameters that are most consistent with observed data by comparing model results with the quiescent fraction measurements derived from our observed cluster sample. Although several initial configurations were tested – all yielding similar conclusions – the MCMC results that we discuss herein were acquired using 100 walkers initialized in a tiny Gaussian ball centered on $R_{\rm quench} = 1.0\ R_{200}$, $m = -0.6$, and $b = 0.80$. For this particular configuration, it took 45,800 steps for the model to converge, where the condition for convergence is defined such that the number of steps taken is greater than 100 times the average auto-correlation time. We find that the highest likelihood model occurs when $R_{\rm quench} = 0.90\ R_{200}$, $m = -0.68$, and $b = 8.23$, whereas the $16^{\rm th}$, $50^{\rm th}$, and $84^{\rm th}$ percentiles of the model parameters are given by $R_{\rm quench} = 0.84^{+0.11}_{-0.21}\ R_{200}$, $m = -0.58^{+0.40}_{-0.26}$, and $b = 7.19^{+2.74}_{-4.20}$.

[4]In fact, the uncertainties that correspond to our observed quiescent fractions are binomial, however, we find that in general $\sigma_{\rm lower} \approx \sigma_{\rm upper}$. For this reason, we simply define $\sigma = \sigma_{lower}$.

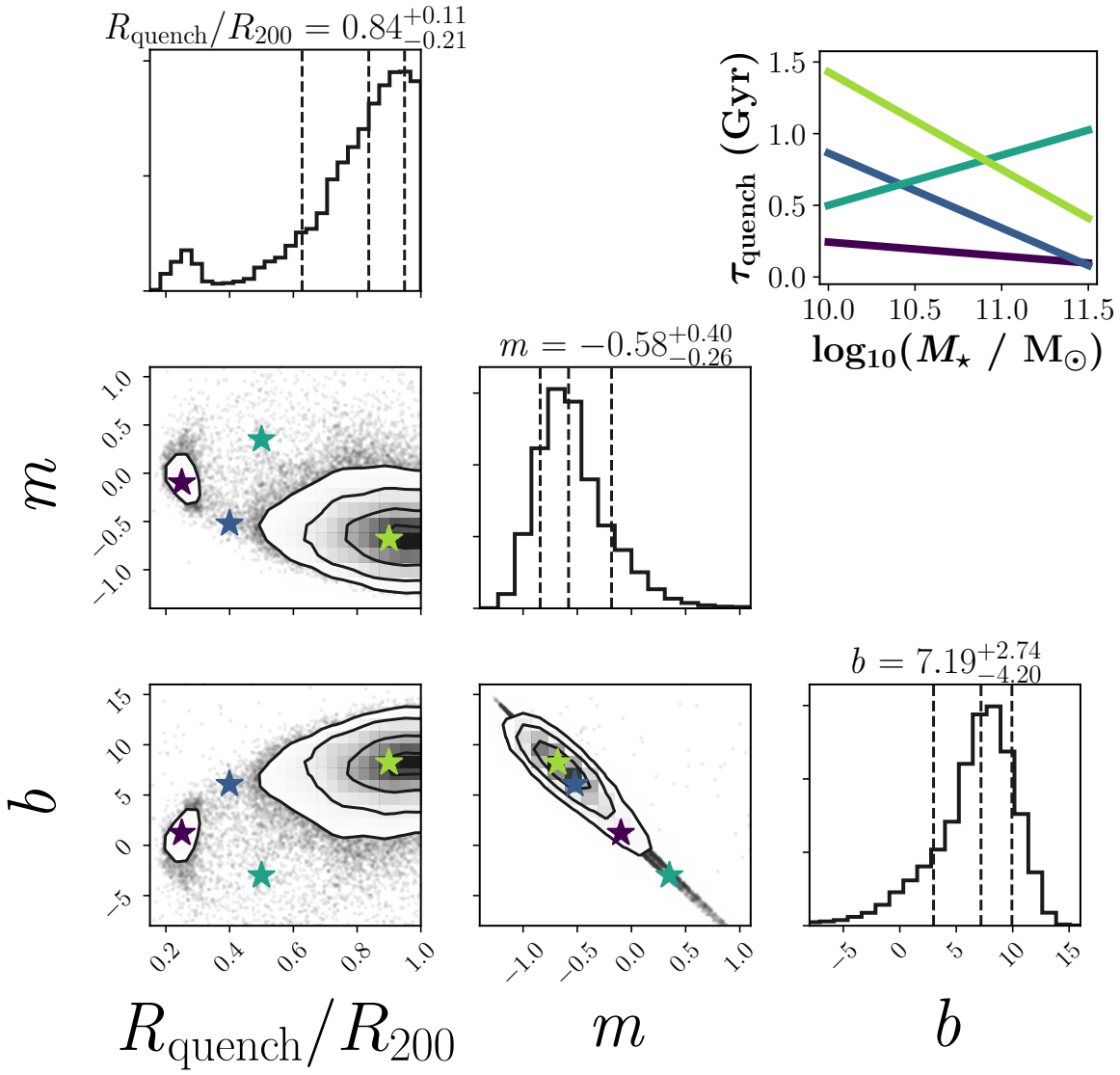

Figure 4.1: Corner plot showing the one- and two-dimensional projections of the posterior probability distributions of the environmental quenching model parameters. The 16$^{\rm th}$, 50$^{\rm th}$, and 84$^{\rm th}$ percentiles associated with the model parameters are shown by the dashed vertical lines. The contours are drawn from the 0.5σ to 2σ level in increments of 0.5σ. The model parameters associated with the highest likelihood model are $R_{\rm quench} = 0.90\ R_{200}$, $m = -0.68$, and $b = 8.23$, where these values are consistent with those found in B22. Nevertheless, we observe that the 1D posterior probability distribution of $R_{\rm quench}$ has an additional local maxima located at $R_{\rm quench} \sim 0.25\ R_{200}$, suggesting that there is another region – albeit relatively small – in this parameter space with solutions that are potentially consistent with the observed satellite quenched fraction trends at $z \gtrsim 1$. We test this by isolating four solutions at $0.25, 0.40, 0.50$, and $0.90\ R_{200}$ – depicted by the filled stars – and performing a more in-depth analysis of how each reproduces the observations. Lastly, the inset in the top right-hand corner illustrates the quenching timescale associated with each of the aforementioned solutions.

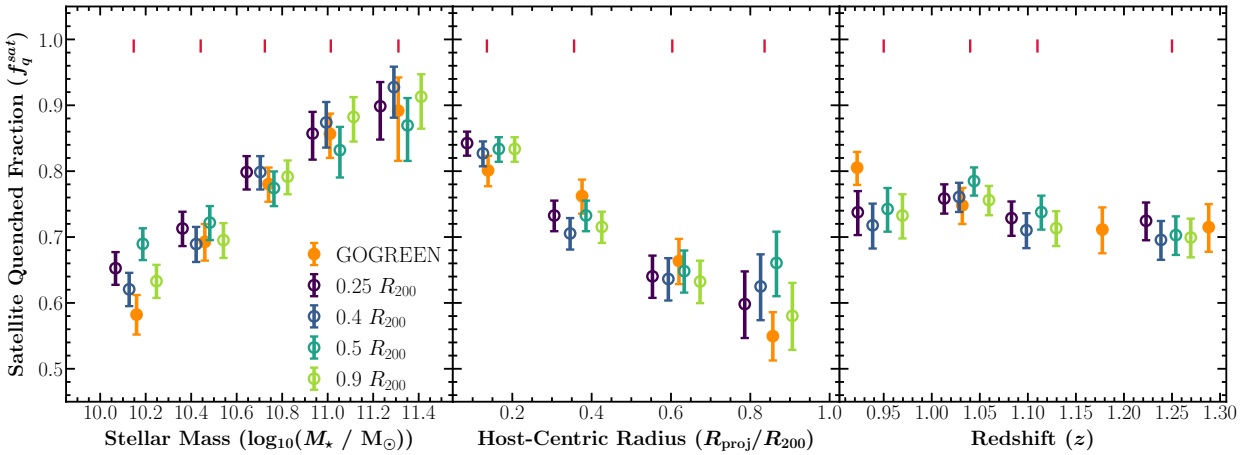

Figure 4.2: Satellite quenched fraction as a function of satellite stellar mass (left panel), projected host-centric radius (middle panel), and redshift (right panel). The orange circles are the measurements associated with our observed cluster sample. The remaining circles are the measurements associated with the four solutions highlighted in Fig. 4.1, which, for simplicity, are labeled according to their associated $R_{\rm quench}$ values. To enhance clarity, we introduce a slight horizontal offset to visually differentiate between the different models, while also including vertical red lines at the top of each panel to indicate the position of the unaltered values. We note that the median redshift bins between the simulated and observed data are inherently offset, likely due to the former being based on discrete snapshots instead of continuous values. With the exception of the model with $R_{\rm quench} = 0.50\ R_{200}$, which overproduces the satellite quenched fraction at low masses and large host-centric radius, these results suggest that there exists a broad range of solutions in the $R_{\rm quench}$-$\tau_{\rm quench}(M_\star)$ parameter space that yield models able to reproduce the observed satellite quiescent fraction as a function of stellar mass, host-centric radius, and redshift as probed by the GOGREEN data set.

The results from our Bayesian inference analysis are summarized in Fig. 4.1, displaying a corner plot that depicts the 1D and joint 2D posterior probability distributions of our model parameters. The first notable observation is that there exist two local maxima in the marginalized distribution of $R_{\rm quench}$ (top-left panel of Fig. 4.1) at ~ 0.25 and 1.0 R_{200}, respectively. This suggests that there are non-unique solutions in the parameter space of our environmental quenching model that are potentially consistent with observations. However, the relative importance of these two local maxima implies that the potential solutions associated with the less prominent peak are confined to a more limited region within the model parameter space. The second notable observation is that there is a well-defined "ridge" of quenching timescales, as illustrated by the strong covariance between the slope and y-intercept of the linear satellite quenching timescale (bottom row, middle column of Fig. 4.1). Specifically, this ridge shows that there are three classes of quenching timescales that are potentially permissible according to our environmental quenching model (see the inset in the top-right corner of Fig. 4.1). The first class consists of quenching timescales that decrease with increasing satellite stellar mass – i.e. the region with $m < 0$. The second class consists of short quenching timescales that are largely independent of satellite stellar mass – i.e. the region around $m \sim 0$. The third class consists of quenching timescales that increase with increasing satellite stellar mass – i.e. the region with $m > 0$. Interestingly, despite the highest likelihood model being found at $R_{\rm quench} = 0.90\ R_{200}$, the aforementioned observations suggest that the $R_{\rm quench}$-$\tau_{\rm quench}$ parameter space is potentially degenerate with a range of possible solutions that are consistent with observations. This observation aligns with the recent findings from Tacchella et al. (2022), which indicate that galaxies likely undergo quenching over a diverse range of timescales. Moreover, recent studies have also highlighted a similar degeneracy between the onset of quenching and the quenching timescale at $z \sim 0$ (Oman et al., 2021; Reeves et al., 2023), signaling the need for additional observable(s) beyond the quiescent fraction to constrain these parameters.

To investigate whether this degeneracy is present in our environmental quenching model, we

select four solutions in our model parameter space – illustrated by the four colored stars in Fig. 4.1 – and directly compare their estimated quiescent fractions with observations. These solutions are selected to probe specific regions of our model's parameter space – i.e. the two local maxima (purple, light-green), the "saddle" between the local maxima (blue), and the outskirts of the covariance relationship between the slope and y-intercept of the linear quenching timescale (green). Furthermore, these four solutions, henceforth denoted by their respective $R_{\rm quench}$ values, are purposely selected to run the gamut of potentially permissible classes of quenching timescales (see top-right inset in Fig. 4.1). As shown in Fig. 4.2, nearly all of these solutions are *roughly* consistent with the observed satellite quenched fraction trends as a function of satellite stellar mass, host-centric radius, and redshift. The only exception occurs for the solution that probes the outskirts of the covariance between the slope and the y-intercept of the linear quenching timescale, given that it overpredicts the quiescent fraction at both low satellite stellar mass and large host-centric radius by more than 2σ. This suggest that quenching timescales that increase towards higher satellite stellar mass are inconsistent with observations, and as such, we will no longer consider the $m > 0$ family of solutions.

In summary, we find that our results are degenerate given that there exists a region in the multi-dimensional parameter space in which seemingly distinct solutions return quiescent fraction trends that are consistent with observations. Nevertheless, two additional questions naturally arise from this observation with the first one being: (*i*) is it possible to rule out solutions by comparing their results with additional measurements derived from our observed cluster population?; and (*ii*) are these seemingly disparate solutions truly distinct *or* do they represent the same underlying quenching pathway? Regarding the first question, we address it immediately in the following subsection, however, we save discussion of the second question for §4.6.2.

4.5.2 Comparison of the Observed and Estimated Properties of Transition Galaxies

One feasible approach to break the aforementioned degeneracy would be to use information from the environmental quenching model – e.g. the time at which satellites environmentally quench – to isolate a population of "transition galaxies" and compare their properties with observations. By transition galaxies, we refer to a class of galaxies that exhibit properties – e.g. intermediate colors and moderate levels of star formation activity – that suggests that they are in a transitional phase between actively star-forming and passive galaxies. They can divided into different types, such as "post-starbursts" (PSB, Dressler & Gunn, 1983, 1992; Couch & Sharples, 1987) and "green valley" (GV, Schiminovich et al., 2007; Schawinski et al., 2014; Vulcani et al., 2015), each with its own distinct evolutionary pathway. PSB galaxies, also known as "E+A" or "K+A" galaxies, are a class of galaxies that have recently undergone a sudden and dramatic cessation of star formation, typically within the last few hundred million years, resulting in strong Balmer absorption lines (EW(Hδ) ≥ 4Å) in their spectra due to the presence of young and hot A-type stars. The "green valley" was initially defined as the region between the "red sequence" and "blue cloud" in color-color or color-stellar mass diagrams. However, many studies have found this definition to be problematic, particularly at high stellar masses and high redshifts, as it is inadvertently includes dusty, star-forming galaxies (DSFGs) (Brammer et al., 2009; Salim et al., 2009). Nevertheless, this issue of contamination from DSFGs can be ameliorated by using rest-frame color-color diagrams, such as $(NUV - V)$ vs $(V - J)$, to define the green valley as the intermediate region between the quiescent and star-forming populations (Mendez et al., 2011; Mok et al., 2014; McNab et al., 2021).

Our approach to isolate the population of transition galaxies associated with our environmental quenching models is to assume that these galaxies are only visible for a limited time window, $t_{\rm window}$, relative to the redshift of observation of our simulated cluster sample. This

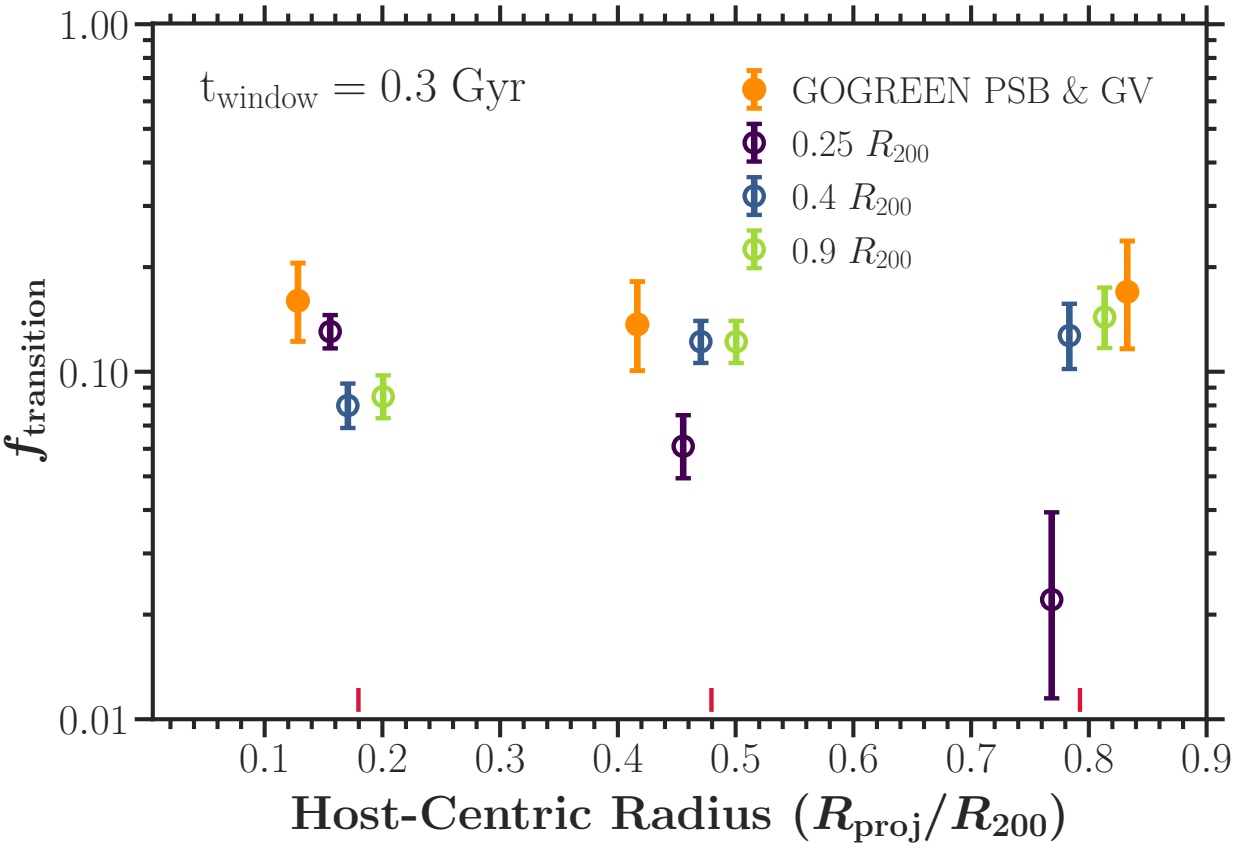

Figure 4.3: The relative abundance of transition galaxies as a function of host-centric radius. The orange circles show the relative abundance of PSB and GV galaxies from the GOGREEN cluster sample (McNab et al., 2021). The remaining circles depict the model results under the assumption that the transition population consists of galaxies that quenched within a fixed time window relative to z_{obs}. In particular, for a given model we define the transition population as satellites that either quench < 0.30 Gyr before z_{obs} *or* star-forming satellites that will quench < 0.30 Gyr after z_{obs}. To improve clarity, a small horizontal offset is applied to distinguish between the various models, while red vertical lines are included slightly above the horizontal axis to mark the position of the unaltered values. We find that all models – with the exception of those at $R_{quench} = 0.25\ R_{200}$ – are generally consistent with observations.

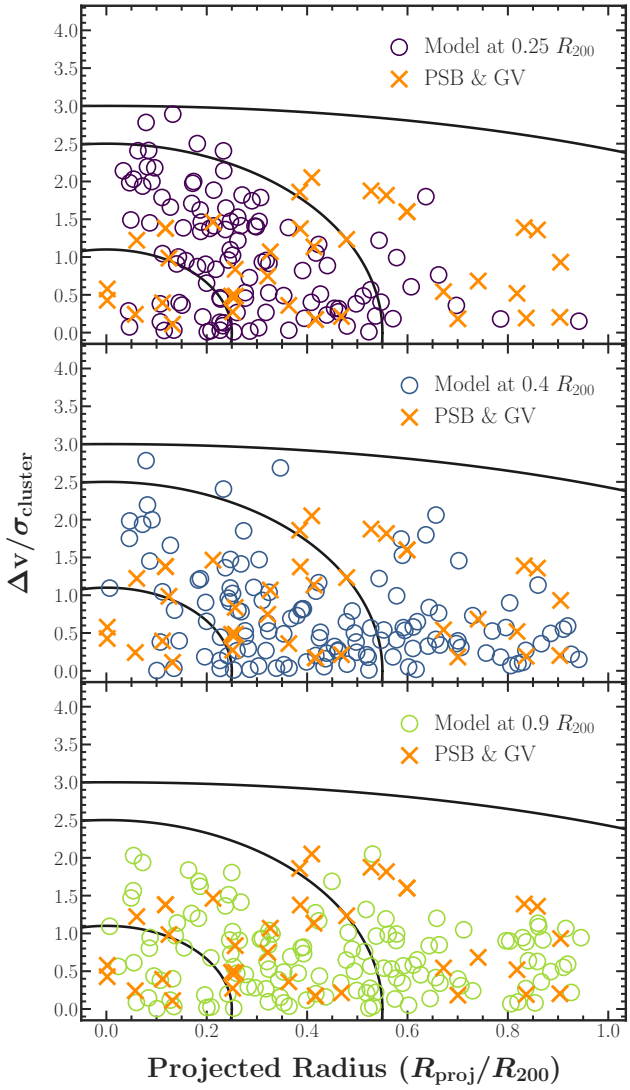

Figure 4.4: The "folded" projected phase-space distribution for transition galaxies selected at the redshift of observation. Each panel compares the projected phase-space distribution associated with the transition galaxies selected from one of the three solution drawn from our environmental quenching model at $R_{\rm quench} = 0.25$, 0.4, and 0.9 R_{200} with the corresponding distribution of PSB and GV galaxies identified in the GOGREEN cluster sample. The solid contours illustrate the phase-space bins adopted by Muzzin et al. (2014). We observe that the solution at $R_{\rm quench} = 0.25$ R_{200} has a relative dearth of transition galaxies in the outer regions of the cluster. Moreover, within the inner $\lesssim 0.30 - 0.35$ R_{200}, the $R_{\rm quench} = 0.25$ R_{200} solution yields transition galaxies with much higher line-of-sight velocities relative to the observed transition galaxy population. A similar argument could also be made for the $R_{\rm quench} = 0.40$ R_{200} solution, such that only the $R_{\rm quench} = 0.90$ R_{200} solution yields line-of-sight velocities in the inner regions of the cluster that are roughly consistent with observations.

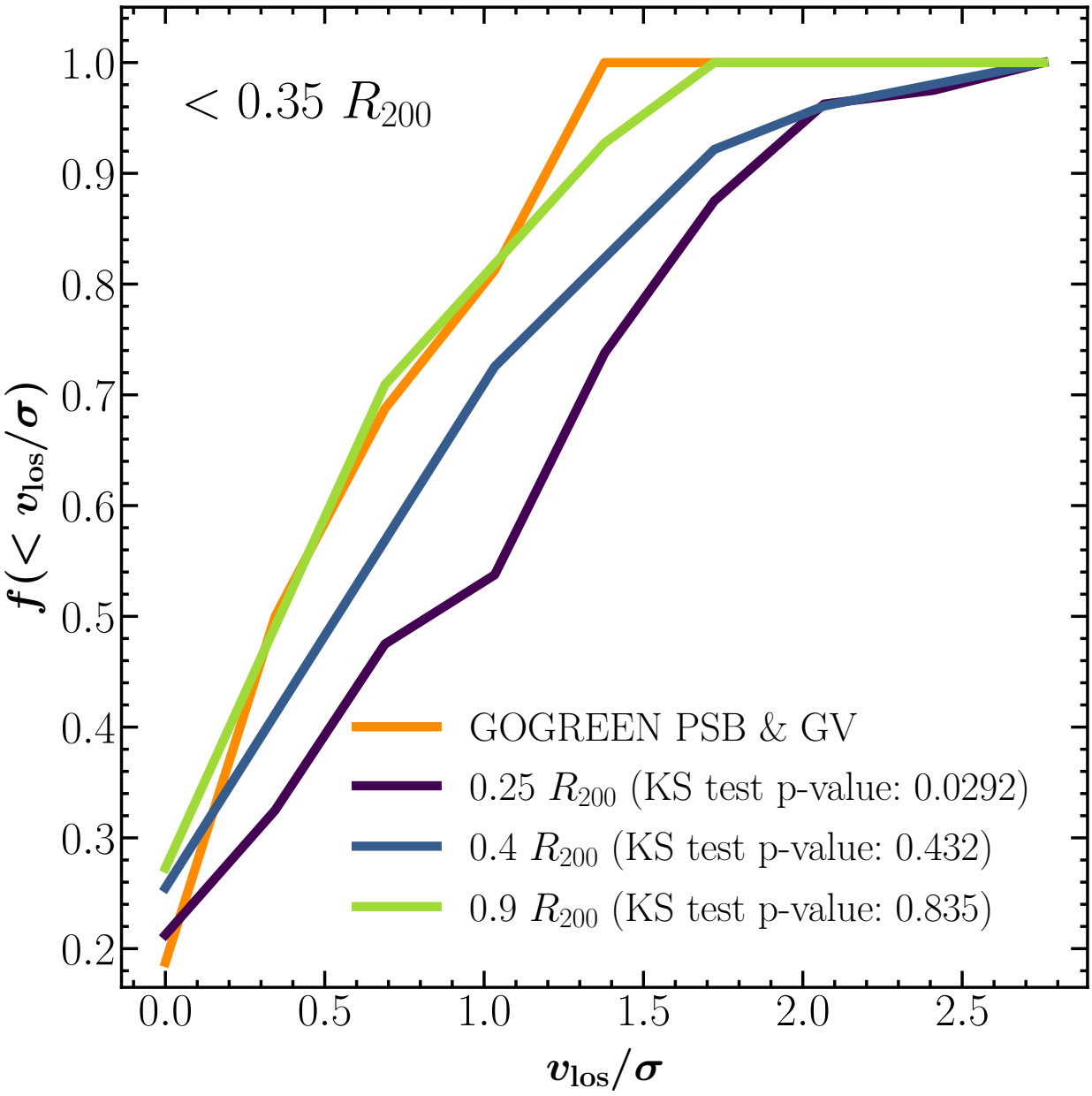

Figure 4.5: The cumulative distribution of the line-of-sight velocities for transition galaxies located within the inner projected 0.35 R_{200} of their host. The orange line represents the observed distribution, whereas all of the other lines correspond to the distributions predicted by the competing environmental quenching models. The legend includes the KS two-sided p-values derived from comparing the observed and predicted line-of-sight velocity distributions. This analysis shows that the null hypothesis can only be rejected for the model with $R_{\rm quench} = 0.25\ R_{200}$.

definition is inspired by the concept of the "visibility time" of transition galaxies, which refers to the limited period during which the defining features of transition galaxies, such as intermediate colors and strong Balmer absorption lines, can be observed. In the framework of our model, we identify the transition galaxy population as galaxies that are within ± 0.30 Gyr of quenching, as measured relative to the redshift of observation. As will be discussed in §4.6.1, this is consistent with the timescales associated with various classes of observationally-identified transition galaxies — e.g. PSB and GV galaxies. In Fig. 4.3, we compare the relative abundance of transition galaxies for each quenching model relative to the abundance of GV and PSB galaxies identified in the GOGREEN cluster sample from McNab et al. (2021). We find that the quenching model with $R_{\rm quench} = 0.25\ R_{200}$ underproduces the observed relative abundance of transition galaxies beyond the very inner regions of the cluster (mainly due to relatively rapid quenching timescale and small quenching radius). Meanwhile, the other two models (with $R_{\rm quench} = 0.4\ R_{200}$ and $R_{\rm quench} = 0.9\ R_{200}$) are generally consistent with the observed abundance of transition galaxies as a function of host-centric distance.

In Fig. 4.4, we also compare the projected phase-space distribution of the simulated transition galaxies with the observed distribution of transition galaxies, as constrained by PSB and GV galaxies in the GOGREEN sample. The first notable observation, in line with the results from Fig. 4.3, is that the solution at $R_{\rm quench} = 0.25\ R_{200}$ yields very few transition galaxies in the outer regions of the cluster. Additionally, within the inner $\lesssim 0.30 - 0.35\ R_{200}$, the $R_{\rm quench} = 0.25\ R_{200}$ solution yields transition galaxies with much higher line-of-sight velocities relative to the observed transition galaxy population. On the surface, it appears that only the $R_{\rm quench} = 0.90\ R_{200}$ solution yields line-of-sight velocities in the inner regions of the cluster that are roughly consistent with observations. To test this, we compute the cumulative line-of-sight velocity normalized by the cluster velocity dispersion ($v_{\rm los}/\sigma$) distributions of the inferred transition galaxies, limited to the inner $0.35\ R_{200}$ of the cluster, and compare the results with the corresponding distribution for the observed sample of transition galaxies from

GOGREEN. This information is shown in Fig. 4.5 along with the Kolmogorov-Smirnov (KS) two-sided p-values. The first major takeaway is that, in addition to failing to reproduce the observed relative abundance of transition galaxies, the model at $R_{\rm quench} = 0.25\ R_{200}$ yields a p-value less than 0.05, indicating that the null hypothesis can be rejected – i.e. the transition population predicted by this model is not drawn from the same parent distribution as the observed sample. Consequently, we consider the solution at $R_{\rm quench} = 0.25\ R_{200}$ to be less viable as it does not adequately reproduce the observed relative abundance of transition galaxies and results in an overabundance of high-velocity satellites in the inner regions of the cluster. Lastly, these results imply that only the solutions with relatively long and mass dependent timescales are unable to be rejected based on the KS test. This, in turn, brings us back to the second question posed at the end of §4.5.1 – i.e. do these solutions represent the same quenching pathway with apparent differences driven by a covariance between $\tau_{\rm quench}$ and $R_{\rm quench}$? In addition to addressing this question, in the following section §4.6, we explore how the aforementioned conclusion depends on our definition of transition galaxies as well as how our results compare with previous environmental quenching studies at $z \sim 1$.

4.6 Discussion

4.6.1 Transition Galaxies and Visibility Times

As mentioned in §4.5.2, our approach for isolating the population of transition galaxies within the framework of our environmental quenching model assumes that these galaxies are visible for a limited time window, $\rm t_{window}$, relative to the redshift of observation in our simulated cluster sample. For PSB galaxies, the visibility times typically indicates the time required for the galaxy's Balmer absorption lines to weaken to the level of a quiescent galaxy, often inferred from the equivalent width measurement of the Hδ absorption line

in the galaxy's spectrum. In contrast, for green valley (GV) galaxies, the visibility time (referred to as the "crossing time") signifies the time required to cross the green valley and is typically inferred using statistical analyses of galaxy properties in the GV region of the color-magnitude diagram.

Studies have indicated that PSB galaxies have a relatively short visibility time, with estimates ranging from $0.1 - 1$ Gyr (Wild et al., 2009; Muzzin et al., 2014; Wild et al., 2016; French et al., 2018; Rowlands et al., 2018; Belli et al., 2019; Wild et al., 2020). On the other hand, GV galaxies have a more extended visibility time, with some studies suggesting that the transition phase can last up to $1 - 2$ Gyr (Bremer et al., 2018; Forrest et al., 2018; Smethurst et al., 2018; Noirot et al., 2022). However, an investigation by Schawinski et al. (2014) found that this timescale depends on morphology, with early-type galaxies crossing the green valley in timescales of less than 0.25 Gyr, and late-type galaxies crossing it in less than 1.0 Gyr. Nevertheless, the exact duration of the visibility time for transition galaxies depends on various factors, including the methodology for identifying them, the specific diagnostic used to estimate transition timescales, the spectral resolution, the signal-to-noise ratio of the observations, and other observables such as the host environment (Paccagnella et al., 2017, 2019; Socolovsky et al., 2019; Mao et al., 2022) and galaxy mass (McNab et al., 2021). Therefore, the exact visibility of PSB and GV galaxies remains uncertain and depends on multiple factors.

The selection of transition galaxies in this analysis, namely satellites within ± 0.30 Gyr of quenching, aligns with the aforementioned estimates of the visibility time for PSB and GV galaxies. While this choice is consistent with observations, widening the visibility window, for example, to ± 0.60 Gyr, would result in the $R_{\rm quench} = 0.25\ R_{200}$ solution predicting a relative abundance of transition galaxies consistent with observations. However, the second conclusion regarding the $R_{\rm quench} = 0.25\ R_{200}$ solution, namely an overabundance of transition galaxies with high line-of-sight velocities in the inner region of the cluster, remains true

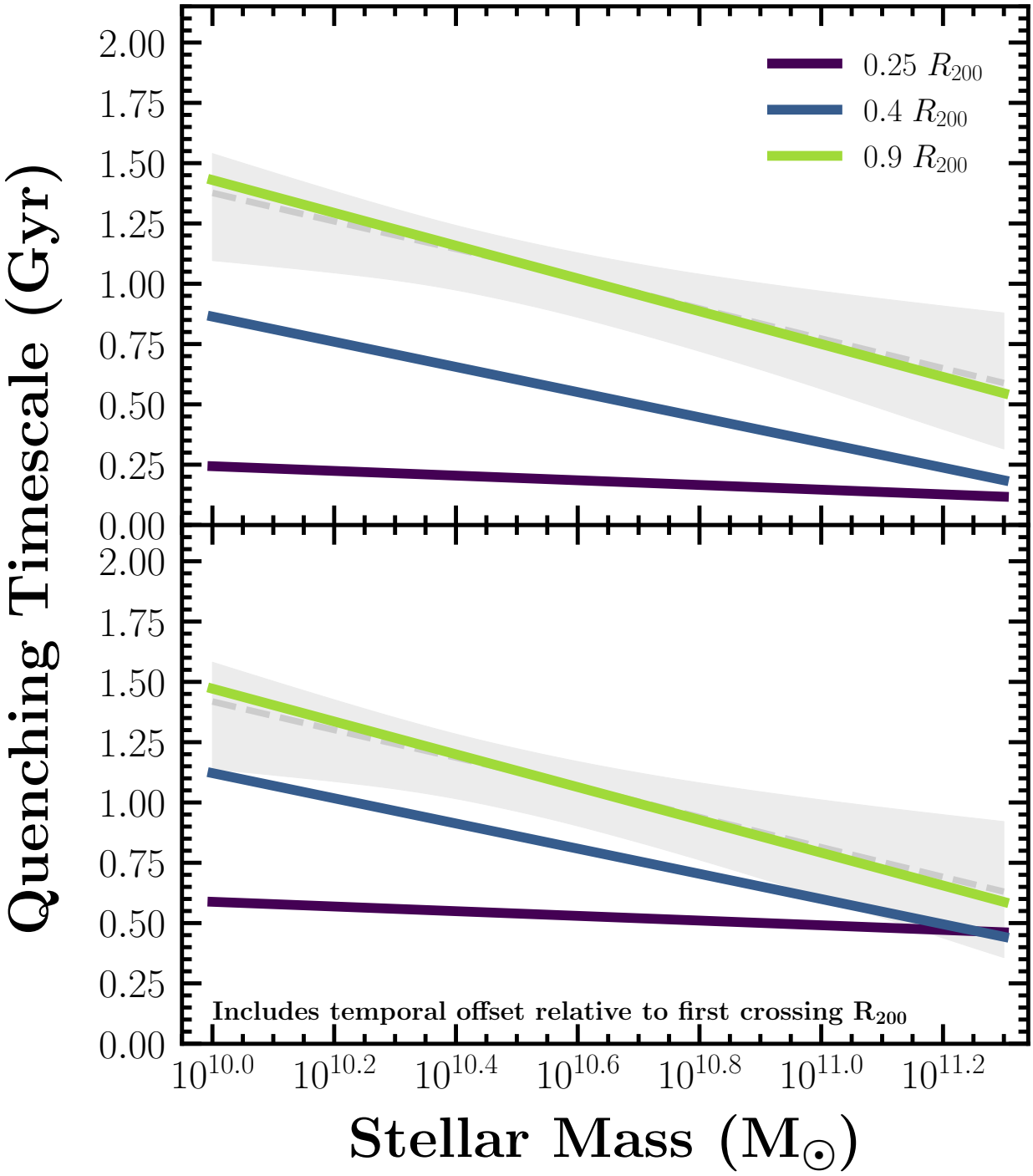

Figure 4.6: Quenching timescales versus satellite stellar mass. The colored lines correspond to the three observationally consistent solutions to our environmental quenching model isolated in Fig. 4.1. The dashed grey line and shaded band represent the results associated with the median and corresponding 1-sigma error of the model parameters derived from our MCMC analysis. The upper panel shows the quenching as measured from the time of crossing $R_{\rm quench}$, whereas the lower panel augments these timescales by adding the median time required for the satellites in a given model to travel from 1.0 R_{200} to $R_{\rm quench}$. These results, namely that the timescales associated with the various solutions do not overlap after taking into consideration the delay time between first crossing 1.0 R_{200} and reaching $R_{\rm quench}$, suggest that our satellite orbits are not exclusively radial.

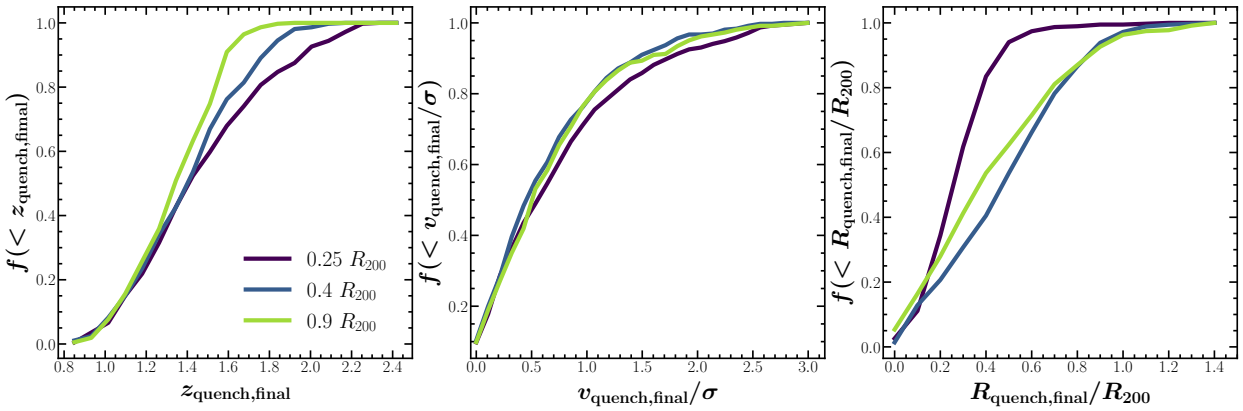

Figure 4.7: The cumulative distribution for the redshift (left panel), velocity (middle panel) and host-centric radius (left panel) corresponding to the time at which the competing models fully quenched their satellite population. With the exception of the models with $R_{\rm quench} \leq 0.25\ R_{200}$, all of the models have strongly overlapping cumulative distributions for the radius *and* line-of-sight velocity at which their satellite populations were environmentally quenched. However, for redshifts above $z \sim 1.3$, there is a clear stratification of the models such that the fraction of galaxies that quench at relatively earlier times increases as $R_{\rm quench}$ decreases. These results suggest that the models with $R_{\rm quench} \leq 0.25\ R_{200}$ experience a distinct quenching pathway from the other models given that they environmentally quench the bulk of their galaxies at earlier times, smaller host-centric radii and with relatively higher line-of-sight velocities.

and even worsens if the visibility window is expanded. Likewise, we find that the general conclusion drawn in §4.5.2 remains true, namely that only solutions with long quenching timescales ($\tau_{\rm quench} \gtrsim 1$ Gyr) and large quenching radius ($R_{\rm quench} \gtrsim 0.4\ R_{200}$), are capable of reproducing the observed abundance *and* phase-space distribution of transition galaxies in clusters at $z \sim 1$. This holds even if we modify our definition of observed transition galaxies to include only PSB or GV galaxies.

4.6.2 Distinct Quenching Pathways?

As stated in §4.5.1, it is important to determine if the various observationally consistent solutions truly represent distinct environmental quenching mechanisms *or* if instead they represent the same quenching mechanism with the differences in quenching timescales being directly tied to changes in the host-centric radius at which quenching begins. A simple

method to test this is to compare the quenching timescale results associated with each of the solutions, which we show in Fig. 4.6. The top panel depicts the quenching timescales relative to crossing $R_{\rm quench}$, whereas the bottom panel augments this timescale by adding the median time required for a satellite to travel from 1.0 R_{200} to $R_{\rm quench}$. The results from Fig. 4.6 suggest that despite having different assumptions for where quenching begins, the solutions at 0.40 and 0.90 R_{200} yield fairly consistent quenching timescales when measured relative to 1.0 R_{200}. Moreover, as illustrated in Fig. 9 from B22, the timescales associated with these two solutions are roughly consistent with the empirically-derived cold gas (HI + H_2) depletion timescale at intermediate z from Popping et al. (2015). Following the logic presented in that analysis, we interpret these solutions to potentially be associated with starvation as the dominant quenching pathway. Nevertheless, additional information is required to determine if the solution at $R_{\rm quench} = 0.25\ R_{200}$ represents a distinct quenching pathway.

A more detailed method of testing if these solutions represent distinct quenching pathways is to compare the properties of their satellite populations – e.g. positions and velocities – at the time in which the quenching process ends. Thus, we compare the cumulative distributions of the host-centric radius at the time in which the three solutions fully environmentally quench their satellite population ($R_{\rm quench,final}$) along with the corresponding line-of-sight velocity and redshift ($v_{\rm quench,final}/\sigma$ and $z_{\rm quench,final}$, respectively). Together with the quenching timescale information, these additional constraints allow us to answer the following questions: (*i*) how long does the satellite quenching process last? (*ii*) where in the cluster does satellite quenching begin and end?; (*iii*) what is the velocity distribution of satellites at the moment at which quenching ends?

The left, middle, and right panels in Fig. 4.7, respectively, compare the cumulative distributions of $z_{\rm quench,final}$, $R_{\rm quench,final}$, and $v_{\rm quench,final}/\sigma$ associated with each of the solutions. The first notable observation is that $z_{\rm quench,final}$ depends on $R_{\rm quench}$ such that the solutions for which quenching begins at larger (smaller) radii finish quenching at later (earlier) times. In

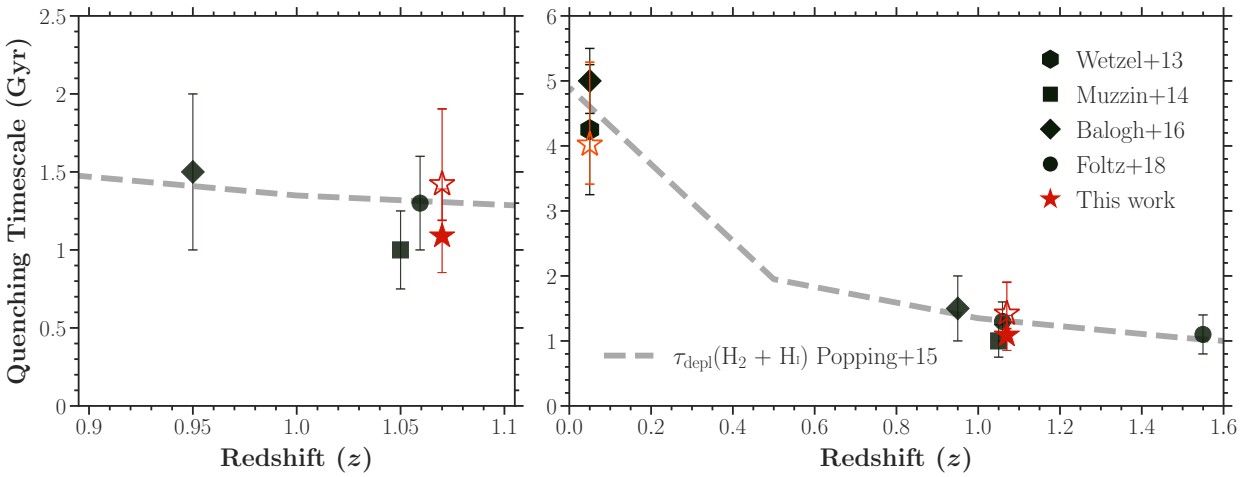

Figure 4.8: Quenching timescale versus redshift for satellites of massive clusters ($M_{\rm halo} \sim 10^{14-15}$ M$_\odot$). The filled (unfilled) red star represents the quenching timescale measured at $M_\star = 10^{10.5}$ M$_\odot$ ($M_\star = 10^{10}$ M$_\odot$) derived from our MCMC analysis (i.e. the dashed grey line in Fig. 4.6). Likewise, the orange unfilled star represents the quenching timescale measured at $M_\star = 10^{10}$ M$_\odot$ scaled according to the evolution of the dynamical time – $\tau_{\rm quench}(M_\star) \times (1+z)^{-1.5}$. The black points show the quenching timescales obtained from comparable studies of environmental quenching in clusters at $z \sim 1$ (left panel) and $0 < z < 1.6$ (right panel) as measured by Wetzel et al. (2013), Muzzin et al. (2014), Balogh et al. (2016), and Foltz et al. (2018). With the exception of the point from Wetzel et al. (2013) – which is evaluated at $M_\star = 10^{10.0}$ M$_\odot$ – all of the results from separate studies are evaluated for satellites with $M_\star > 10^{10.5}$ M$_\odot$. The dashed gray line depicts the empirically-derived cold gas (HI + H_2) depletion timescale from Popping et al. (2015) evaluated at $M_\star = 10^{10.5}$ M$_\odot$.

line with the results shown in the bottom panel of Fig. 4.6, this indicates that for models with a small $R_{\rm quench}$, the time interval between becoming a satellite (i.e., first crossing R_{200}) and reaching $R_{\rm quench}$ is *shorter* than the time required to quench satellites for the models with a large $R_{\rm quench}$. Additionally, we observe that the solutions at 0.40 and 0.90 R_{200} have consistent cumulative distribution of $R_{\rm quench,final}$ and $v_{\rm quench,final}/\sigma$. This suggests that these solutions are agnostic towards where quenching begins given that they quench their satellite populations at similar host-centric radii and with overlapping line-of-sight velocities distributions. By the same token, we observe that the quiescent satellites associated with the solution at $R_{\rm quench} = 0.25$ R_{200} predominantly quench in the core of the cluster (80% quenched at < 0.40 R_{200}) with relatively high line-of-sight velocities.

We interpret the results from Figs. 4.6 and 4.7 as evidence of two distinct quenching path-

ways, which we define as "starvation" and "core-quenching". The former, which applies to the solutions with $R_{\rm quench} = 0.40$ and 0.90 R_{200}, is characterized by relatively long (> 1.0 Gyr) mass-dependent quenching timescales that are roughly consistent with the total cold gas (HI+H_2) depletion timescale at intermediate z. Meanwhile, the latter is characterized by satellites with relatively high line-of-sight velocities that quench on short timescales (~ 0.25 Gyr) after reaching the inner region of the cluster (< 0.25 R_{200}). It is interesting to note that the "core-quenching" pathway and RPS exhibit similar characteristics: both tend to quench high-velocity satellites located at small distances from their host galaxy's center, and the quenching occurs relatively quickly ($\lesssim 1$ Gyr) (Boselli et al., 2022). These similarities raise the possibility that the "core-quenching" pathway could be similar to the RPS mechanism responsible for forming "jellyfish galaxies" (Poggianti et al., 2017; Vulcani et al., 2020a), especially since many of these galaxies are also observed in the inner regions of clusters (< 0.40 R_{200}) (Gullieuszik et al., 2020). Nevertheless, while the idea is captivating, we assert that it is beyond the scope of this study to establish a direct equivalence between the "core-quenching" pathway and RPS.

4.6.3 Comparison with Previous Studies

In the left panel of Fig. 4.8, we compare the quenching timescale inferred from this investigation with results from previous environmental quenching studies of cluster populations ($M_{\rm halo} > 10^{14}$ $M_\odot$) at $z \sim 1$ for satellites with $M_\star > 10^{10.5}$ $M_\odot$. These studies include Muzzin et al. (2014), Balogh et al. (2016), and Foltz et al. (2018), and they were selected given that they utilize a compatible definition of $\tau_{\rm quench}$ – i.e. defined as the timescale upon which satellites quench as measured relative to first infall. Nevertheless, we acknowledge that these studies utilize distinct methodologies for inferring the quenching timescale. For example, Balogh et al. (2016) inferred quenching timescales of 1.5 ± 0.5 Gyr by relating the passive fraction in 10 galaxy clusters from the GCLASS survey to infall histories estimated

from semi-analytic simulations. Meanwhile, Muzzin et al. (2014) used galaxy spectral features to identify PSB galaxies in the GCLASS cluster sample and related the distribution of this population in phase space to the phase-space distribution of infalling subhalos in dark-matter-only zoom-in simulations to obtain a quenching timescale of 1.0 ± 0.25 Gyr. Lastly, Foltz et al. (2018) inferred a total quenching timescale of 1.3 ± 0.3 by relating the observed numbers of star-forming, quiescent, and green valley galaxies in 10 galaxy clusters to a simulated cluster mass accretion rate using a "delayed-then-rapid" quenching model (Wetzel et al., 2013; McGee et al., 2014; Mok et al., 2014; Balogh et al., 2016; Fossati et al., 2017).

Despite the different methodologies utilized in these studies, the inferred timescales broadly agree that satellite quenching at $z \gtrsim 1$ proceeds on timescales between $1 - 1.5$ Gyr following accretion onto an established cluster. As shown in Fig. 4.8, these timescales are all roughly consistent with the total cold gas depletion timescale at this epoch, suggesting that the consumption of cold gas in absence of cosmological accretion – i.e. starvation – could be the dominant quenching mechanism at this epoch. Nevertheless, it is important to acknowledge the findings of Muzzin et al. (2014), whose PSB-focused quenching study concludes that RPS is the dominant mechanism in massive clusters. Likewise, the results of Foltz et al. (2018) suggest that quenching takes place on the dynamical timescale of the cluster, although they cannot dismiss the possibility of quenching due to gas depletion in the absence of cosmological accretion.

In the left panel of Fig. 4.8, we explore the redshift dependence of the satellite quenching timescale by including results from Wetzel et al. (2013) at $z \sim 0$ – evaluated at $M_\star = 10^{10}$ $\mathrm{M}_\odot$ for $M_{\mathrm{halo}} = 10^{14-15}$ $\mathrm{M}_\odot$ – and results at $z \sim 1.6$ from Foltz et al. (2018). We also include the quenching timescale estimate at $z \sim 0$ from Balogh et al. (2016), obtained by scaling τ_{quench} according to the dynamical time – i.e. $\tau_{\mathrm{quench}} \times (1+z)^{-1.5}$. We perform a similar scaling using our inferred quenching timescale evaluated at $M_\star = 10^{10}$ $\mathrm{M}_\odot$ to obtain an estimate of the

quenching timescale at $z \sim 0$. As noted in several previous studies, we find that the satellite quenching timescale evolves roughly like the dynamical time (Tinker & Wetzel, 2010; Balogh et al., 2016; Foltz et al., 2018; Baxter et al., 2022). Although the catalyst behind the redshift evolution of the quenching timescale remains unknown, one possible interpretation of the aforementioned observation is that the environmental quenching mechanism(s) responsible for producing the observed quenched fraction results in clusters at $z \sim 1$ are potentially equivalent to those at play in their low-z descendants, where the differences in timescales between the separate epochs is due to the evolution of the host system properties (e.g. halo masses, velocity dispersion, etc.), but not the quenching mechanism itself.

In comparing our investigation to previous studies, it is important to highlight that the transition galaxy phase space analysis detailed in §4.5.2 shares similarities with the approach used in Muzzin et al. (2014) to constrain $R_{\rm quench}$ and $\tau_{\rm quench}$ at $z \sim 1$. Specifically, in Muzzin et al. (2014) they compare the projected phase space distribution of PSB galaxies from the GCLASS cluster sample with that of simulated PSB galaxies, which they infer by isolating galaxies in time-steps of 0.2 Gyr after first passage of 0.25, 0.50, and 1.0 R_{200}. Moreover, by using a 2D KS test to compare these distributions, they rule out all scenarios in which quenching begins after the first passage of 1.0 R_{200} and lasts between $0.5 - 1.1$ Gyr. Additionally, they find that the combination of $R_{\rm quench} = 0.50\ R_{200}$ and $\tau_{\rm quench} = 1.0$ Gyr is most consistent with the data. In essence, despite the fact that the clusters explored in Muzzin et al. (2014) constitute a subset of our sample, we arrive at contrasting conclusions regarding where within the cluster - and for how long - quenching takes place.

Nevertheless, comparing these two investigations objectively presents challenges due to several key differences. Firstly, the studies employ different populations of transition galaxies and clusters. For instance, in the study by Muzzin et al. (2014), the transition galaxies are exclusively limited to spectroscopically selected PSB galaxies primarily sourced from two massive clusters at a redshift of $z = 0.87$. In contrast, our study includes both photo-

metrically selected GV galaxies and spectroscopically selected PSB galaxies as part of the transition galaxy population, predominantly obtained from higher-redshift clusters. Considering that Muzzin et al. (2014) attributes quenching to RPS, one possible interpretation is that the influence of RPS becomes more pronounced with increasing halo mass and decreasing redshift. Additionally, besides utilizing distinct infall histories to select our simulated transition galaxy populations, both studies employ unique methodologies. For example, in contrast to their analysis, we investigate the stellar mass dependence of environmental quenching and track the self-quenching of the infalling field population. The consideration of stellar mass dependence is important since, as demonstrated in figure 4 of B22, the observed quiescent fraction trends cannot be replicated under the assumption that the quenching timescale, measured since first passage of 1.0 R_{200}, is independent of satellite stellar mass. Moreover, incorporating a self-quenching prescription based on measurements of the observed field quenched fraction introduces an additional stellar mass dependence to the satellite quenching process, indicating that more massive satellites, on average, would be expected to undergo quenching in the field or infall region compared to their less massive counterparts. Considering all these factors, it is highly likely that the discrepancies between our analyses stem from a combination of disparate methodologies and variations in cluster and transition galaxy populations.

4.7 Summary and Conclusions

In our recent paper, B22, we investigated the dominant quenching mechanism in massive clusters at $z \gtrsim 1$, using a simple infall-based environmental quenching model parameterized by the quenching timescale $\tau_{\rm quench}$. The success of this model was that it: (i) improved upon previous studies by implementing a prescription for field quenching and pre-processing in the infall region; (ii) is fairly simple in that it involves one primary parameter - i.e. the

satellite quenching timescale $\tau_{\rm quench}$; (*iii*) roughly reproduces the observed satellite stellar mass function as well as the satellite quenched fraction as a function of stellar mass (by construction), host-centric radius, and redshift; and (*iv*) yields quenching timescales that are consistent with the total cold gas depletion time at intermediate z, suggesting that "starvation" - i.e. the depletion of cold gas in the absence of cosmological accretion - is the dominant driver of environmental quenching at $z < 2$.

Thus, the motivation for this follow-up investigation was to further test the validity of this conclusion by developing a more generalized environmental quenching model that allows for potentially distinct quenching pathways through the introduction of the parameter $R_{\rm quench}$ – i.e. the host-centric radius corresponding to the onset of environmental quenching. To this end, we performed a comprehensive MCMC analysis to fully explore the parameter space of our updated environmental quenching model, and ultimately discovered two local maxima at approximately 0.25 and 1.0 R_{200} in the 1D posterior probability distribution of $R_{\rm quench}$. From here, we isolated four distinct solutions in the $R_{\rm quench} - \tau_{\rm quench}$ parameter space - i.e. two near the aforementioned local maxima, one in the "saddle" between the local maxima, and one in the outskirts of the covariance relationship between the slope and y-intercept of the linear quenching timescale. We discovered that, with the exception of the solution in the outskirts of the aforementioned covariance relation, all solutions reproduce the satellite quenched fraction trends associated with our GOGREEN cluster population.

In an effort to determine if these solutions represent distinct quenching pathways, we compared their quenching timescales (relative to first crossing R_{200}) as well as their positions and velocities at the time of quenching. Based on this information, we separated the solutions between those driven by "starvation" and "core-quenching". The former quenching pathway corresponds to model solutions that exhibit quenching timescales that are aligned reasonably well with the total cold gas (HI+H_2) depletion timescale at intermediate z. On the other hand, the latter pathway, which bears resemblance to ram-pressure stripping, is characterized

by satellites with relatively high line-of-sight velocities, experiencing rapid quenching within a short timescale (~ 0.25 Gyr) after entering the inner region of the cluster ($< 0.30\ R_{200}$). To break the degeneracy among these solutions, we compared our model results with observed properties of transition galaxies in massive clusters at $z \gtrsim 1$ from the GOGREEN survey. From this analysis, we found that only the solutions associated with the starvation quenching pathway are consistent with both the observed quiescent fraction trends *and* the phase-space distribution and relative abundance of transition galaxies at $z \gtrsim 1$.

In conclusion, this investigation provides further insight into the dominant quenching mechanisms in massive clusters at $z \gtrsim 1$, and shows that results from a simple environmental quenching model can be used to isolate distinct quenching pathways. By comparing model results with observations, we found that the "core-quenching" pathway is not consistent with the observed transition galaxy trends. Conversely, our results are consistent with the scenario in which galaxies quench on relatively long timescale between $1.0 - 1.5$ Gyr after accretion, thus supporting the idea that starvation may be the dominant quenching mechanism at $z < 2$. Nonetheless, despite the concordance between the inferred quenching timescales and the total gas depletion time during this epoch, this study provides evidence supporting the importance of group pre-processing in shaping the observed quiescent fraction, as well as the notion that RPS contributes as a secondary mechanism for quenching in massive clusters at $z \gtrsim 1$, in line with recent environmental quenching reviews (Cortese et al., 2021; Alberts et al., 2022).

Chapter 5

Summary and Conclusion

Qu'est-ce qu'un scientifique après tout? C'est un homme curieux qui regarde à travers un trou de serrure, le trou de serrure de la nature, essayant de savoir ce qui se passe.

– Jacques-Yves Cousteau

This dissertation represents the culmination of approximately 6 years of dedicated research, professional development as a scientist, and the invaluable guidance and support from an extensive network of scientists and mentors. The focus of this chapter is to showcase the outcomes and conclusions derived from my graduate work.

5.1 Dwarf Satellite Quenching with Machine Learning

In this chapter, we develop a supervised machine learning and statistical background subtraction technique to study the poorly understood regime of low-mass satellite quenching. The primary findings and conclusions from this investigation are as follows:

- We successfully reproduce the measured satellite quenched fraction at $M_\star \gtrsim 10^{10}$ $M_\odot$,

as derived from spectroscopic studies in the local Universe. We find that the satellite quenched fraction increases with increasing satellite mass at $M_\star \gtrsim 10^{10}$ $M_\odot$.

- We measure the satellite quenched fraction down to $M_\star \sim 10^7$ $M_\odot$, pushing measurements of satellite quenching in $\sim 10^{13-14}$ h^{-1} $M_\odot$ halos to a new regime that is not readily probed outside of the Local Group.

- We find that the satellite quenched fraction increases towards lower satellite masses below $\sim 10^9$ $M_\odot$.

- The increase in satellite quenching at low masses potentially indicates a change in the dominant quenching mechanism at $\sim 10^9$ $M_\odot$, where ram-pressure stripping begins to become increasingly effective.

5.2 Quenching Timescales of Cluster Satellites at $z \gtrsim 1$

In this chapter, we address the uncertainty on the dominant quenching mechanism at play in massive clusters at $z \sim 1$, as evidence by modern cosmological models inability to reproduce observed trends of satellite quenched fractions at this epoch. Our focus is to constrain the crucial timescale of satellite quenching ($\tau_{\rm quench}$), which characterizes the efficiency of star formation shutdown and sheds light on dominant environmental quenching mechanisms. Using a similar approach employed in low-z environmental quenching studies, we model satellite quenching to place constraints on $\tau_{\rm quench}$. To achieve this, we combine observations of 14 massive clusters ($M_{\rm halo} = 10^{14-15}$ $M_\odot$) at $z \gtrsim 1$ from the GOGREEN and GCLASS surveys with the accretion and orbital histories of analogous cluster populations extracted

from N-body simulations. The following are the key findings of our investigation:

- Our infall-based environmental quenching model successfully reproduces the observed satellite quenched fraction as a function of stellar mass, projected cluster-centric radius, and redshift.

- We find that satellite quenching is mass dependent at $z \sim 1$, such that the efficiency of environmental quenching increases with satellite stellar mass.

- In comparison to similar analyses at low redshift, we find that the satellite quenching timescale evolves roughly like the dynamical time ($\propto (1+z)^{-3/2}$).

- When including pre-processing within the cluster infall regions, we find that the vast majority ($\sim 65-80\%$) of massive satellites ($> 10^{11}$ $M_{\odot}$) in clusters are quenched at $z \sim 1$ clusters prior to infall. In contrast, the majority of lower-mass satellites ($\lesssim 10^{10.5}$ $M_{\odot}$) quenched within the cluster.

- Our satellite quenching model yields quenching timescales that are longer than the observed molecular depletion timescales at intermediate redshift. Instead, the inferred quenching timescales are roughly consistent with the predicted total cold gas depletion timescale (HI+ H_2) at $1 < z < 2$.

5.3 Environmental Quenching in Clusters at $z \gtrsim 1$

In this chapter, we explore models of satellite quenching in massive clusters at $z \gtrsim 1$ using an MCMC framework, focusing on two primary parameters: $R_{\rm quench}$ (the host-centric radius

at which quenching begins) and $\tau_{\rm quench}$ (the timescale upon which a satellite quenches after crossing $R_{\rm quench}$). The primary findings and conclusions from this investigation are as follows:

- A comprehensive MCMC analysis revealed two local maxima in the 1D posterior probability distribution of $R_{\rm quench}$ at approximately 0.25 and 1.0 R_{200}.

- Four distinct solutions were identified in the $R_{\rm quench} - \tau_{\rm quench}$ parameter space, including those near the local maxima, in the saddle between them, and in the outskirts of the covariance relationship between the slope and y-intercept of the linear quenching timescale.

- The solutions were classified into two quenching pathways based on quenching timescales relative to first crossing R_{200}, positions, and velocities at the time of quenching.

    1. Starvation Pathway: Solutions aligned with the total cold gas depletion timescale and indicated gradual quenching over $1.0 - 1.5$ Gyr after accretion.
    2. Core-Quenching Pathway: Solutions resembling ram-pressure stripping, with rapid quenching within a short timescale after entering the inner region of the cluster.

- Comparing model results with observed properties of transition galaxies in massive clusters at $z \gtrsim 1$ from the GOGREEN survey, only solutions associated with the starvation quenching pathway were consistent with observed trends in quiescent fraction, phase-space distribution, and relative abundance of transition galaxies.

- The study supports the idea that starvation is the dominant quenching mechanism at $z < 2$. However, it also highlights the importance of group pre-processing and suggests that ram-pressure stripping contributes as a secondary mechanism for quenching in massive clusters at $z \gtrsim 1$.

Bibliography

Abadi M. G., Moore B., Bower R. G., 1999, MNRAS, 308, 947

Aihara H., et al., 2011, ApJS, 193, 29

Akins H. B., Christensen C. R., Brooks A. M., Munshi F., Applebaum E., Angelhardt A., Chamberland L., 2020, arXiv e-prints, p. arXiv:2008.02805

Alberts S., Adams J., Gregg B., Pope A., Williams C. C., Eisenhardt P. R. M., 2022, arXiv e-prints, p. arXiv:2201.01307

Annis J., et al., 2014, ApJ, 794, 120

Annunziatella M., et al., 2016, A&A, 585, A160

Astropy Collaboration et al., 2013, A&A, 558, A33

Astropy Collaboration et al., 2018, AJ, 156, 123

Ayromlou M., Kauffmann G., Yates R. M., Nelson D., White S. D. M., 2021, MNRAS, 505, 492

Bahé Y. M., McCarthy I. G., Balogh M. L., Font A. S., 2013, MNRAS, 430, 3017

Bahé Y. M., et al., 2017, MNRAS, 470, 4186

Baldry I. K., Balogh M. L., Bower R. G., Glazebrook K., Nichol R. C., Bamford S. P., Budavari T., 2006, MNRAS, 373, 469

Balogh M. L., Morris S. L., Yee H. K. C., Carlberg R. G., Ellingson E., 1997, ApJ, 488, L75

Balogh M. L., Schade D., Morris S. L., Yee H. K. C., Carlberg R. G., Ellingson E., 1998, ApJ, 504, L75

Balogh M. L., Navarro J. F., Morris S. L., 2000, ApJ, 540, 113

Balogh M. L., et al., 2016, MNRAS, 456, 4364

Balogh M. L., et al., 2017, MNRAS, 470, 4168

Balogh M. L., et al., 2021, MNRAS, 500, 358

Barro G., et al., 2019, ApJS, 243, 22

Baxter D. C., Cooper M. C., Fillingham S. P., 2021, MNRAS, 503, 1636

Baxter D. C., et al., 2022, MNRAS, 515, 5479

Behroozi P. S., Wechsler R. H., Conroy C., 2013, ApJ, 770, 57

Bekki K., 2014, MNRAS, 438, 444

Bekki K., Couch W. J., Shioya Y., 2002, ApJ, 577, 651

Bell E. F., et al., 2004, ApJ, 608, 752

Belli S., Newman A. B., Ellis R. S., 2019, ApJ, 874, 17

Bianconi M., Smith G. P., Haines C. P., McGee S. L., Finoguenov A., Egami E., 2018, MNRAS, 473, L79

Bigiel F., et al., 2011, ApJ, 730, L13

Biviano A., et al., 2021, A&A, 650, A105

Blanton M. R., et al., 2005, AJ, 129, 2562

Boselli A., et al., 2016a, A&A, 585, A2

Boselli A., et al., 2016b, A&A, 587, A68

Boselli A., et al., 2019, A&A, 631, A114

Boselli A., Fossati M., Sun M., 2022, A&ARv, 30, 3

Boylan-Kolchin M., Springel V., White S. D. M., Jenkins A., 2010, MNRAS, 406, 896

Brammer G. B., van Dokkum P. G., Coppi P., 2008, ApJ, 686, 1503

Brammer G. B., et al., 2009, ApJ, 706, L173

Bremer M. N., et al., 2018, MNRAS, 476, 12

Brinchmann J., Charlot S., White S. D. M., Tremonti C., Kauffmann G., Heckman T., Brinkmann J., 2004, MNRAS, 351, 1151

Brodwin M., et al., 2010, ApJ, 721, 90

Bruzual G., Charlot S., 2003, MNRAS, 344, 1000

Bruzual A. G., 1983, ApJ, 273, 105

Bundy K., et al., 2006, ApJ, 651, 120

Bundy K., et al., 2015, ApJS, 221, 15

Busha M. T., Wechsler R. H., Behroozi P. S., Gerke B. F., Klypin A. A., Primack J. R., 2011, ApJ, 743, 117

Calzetti D., Armus L., Bohlin R. C., Kinney A. L., Koornneef J., Storchi-Bergmann T., 2000, ApJ, 533, 682

Castignani G., et al., 2022, A&A, 657, A9

Cen R., Pop A. R., Bahcall N. A., 2014, Proceedings of the National Academy of Science, 111, 7914

Ceverino D., Klypin A., 2009, ApJ, 695, 292

Chabrier G., 2003, PASP, 115, 763

Chan J. C. C., et al., 2021, ApJ, 920, 32

Chollet F., et al., 2015, Keras, `https://keras.io`

Christlein D., Zabludoff A. I., 2005, ApJ, 621, 201

Cooke E. A., et al., 2016, ApJ, 816, 83

Cooper M. C., et al., 2006, MNRAS, 370, 198

Cooper M. C., et al., 2007, MNRAS, 376, 1445

Cooper M. C., Gallazzi A., Newman J. A., Yan R., 2010a, MNRAS, 402, 1942

Cooper M. C., et al., 2010b, MNRAS, 409, 337

Cortese L., et al., 2007, MNRAS, 376, 157

Cortese L., Catinella B., Smith R., 2021, Publ. Astron. Soc. Australia, 38, e035

Couch W. J., Sharples R. M., 1987, MNRAS, 229, 423

Cramer W. J., et al., 2022, arXiv e-prints, p. arXiv:2209.06929

Croton D. J., et al., 2006, MNRAS, 365, 11

Cybulski R., Yun M. S., Fazio G. G., Gutermuth R. A., 2014, MNRAS, 439, 3564

Darvish B., Mobasher B., Sobral D., Rettura A., Scoville N., Faisst A., Capak P., 2016, ApJ, 825, 113

Davé R., Rafieferantsoa M. H., Thompson R. J., Hopkins P. F., 2017, MNRAS, 467, 115

Davies L. J. M., et al., 2016, MNRAS, 455, 4013

Davis M., Efstathiou G., Frenk C. S., White S. D. M., 1985, ApJ, 292, 371

De Lucia G., Weinmann S., Poggianti B. M., Aragón-Salamanca A., Zaritsky D., 2012, MNRAS, 423, 1277

De Lucia G., Hirschmann M., Fontanot F., 2019a, MNRAS, 482, 5041

De Lucia G., Hirschmann M., Fontanot F., 2019b, MNRAS, 482, 5041

Demarco R., et al., 2010, ApJ, 711, 1185

Di Matteo T., Springel V., Hernquist L., 2005, Nature, 433, 604

Dolag K., Borgani S., Murante G., Springel V., 2009, MNRAS, 399, 497

Donnari M., Pillepich A., Nelson D., Marinacci F., Vogelsberger M., Hernquist L., 2021, MNRAS, 506, 4760

Dressler A., 1980, ApJ, 236, 351

Dressler A., 1984, ARA&A, 22, 185

Dressler A., Gunn J. E., 1983, ApJ, 270, 7

Dressler A., Gunn J. E., 1992, ApJS, 78, 1

Driver S. P., et al., 2009, Astronomy and Geophysics, 50, 5.12

Driver S. P., et al., 2011, MNRAS, 413, 971

Faber S. M., et al., 2007, ApJ, 665, 265

Farouki R., Shapiro S. L., 1981, ApJ, 243, 32

Fillingham S. P., Cooper M. C., Wheeler C., Garrison-Kimmel S., Boylan-Kolchin M., Bullock J. S., 2015, MNRAS, 454, 2039

Fillingham S. P., Cooper M. C., Pace A. B., Boylan-Kolchin M., Bullock J. S., Garrison-Kimmel S., Wheeler C., 2016, MNRAS, 463, 1916

Fillingham S. P., Cooper M. C., Boylan-Kolchin M., Bullock J. S., Garrison-Kimmel S., Wheeler C., 2018, MNRAS, 477, 4491

Fioc M., Rocca-Volmerange B., 1997, A&A, 500, 507

Foley R. J., et al., 2011, ApJ, 731, 86

Foltz R., et al., 2018, ApJ, 866, 136

Font A. S., et al., 2008, MNRAS, 389, 1619

Foreman-Mackey D., Hogg D. W., Lang D., Goodman J., 2013, PASP, 125, 306

Forrest B., et al., 2018, ApJ, 863, 131

Forrest B., et al., 2020a, ApJ, 890, L1

Forrest B., et al., 2020b, ApJ, 903, 47

Fossati M., et al., 2017, ApJ, 835, 153

French K. D., Yang Y., Zabludoff A. I., Tremonti C. A., 2018, ApJ, 862, 2

Freundlich J., et al., 2019, A&A, 622, A105

Fujita Y., 2004, PASJ, 56, 29

Galametz A., et al., 2013, ApJS, 206, 10

Gavazzi G., Consolandi G., Gutierrez M. L., Boselli A., Yoshida M., 2018, A&A, 618, A130

Geha M., Blanton M. R., Yan R., Tinker J. L., 2012, ApJ, 757, 85

Geha M., et al., 2017, ApJ, 847, 4

Genzel R., et al., 2010, MNRAS, 407, 2091

Gill S. P. D., Knebe A., Gibson B. K., 2005, MNRAS, 356, 1327

Gladders M. D., Yee H. K. C., 2000, AJ, 120, 2148

Gnedin O. Y., 2003, ApJ, 582, 141

Gómez P. L., et al., 2003, ApJ, 584, 210

Gottlöber S., Klypin A., Kravtsov A. V., 2001, ApJ, 546, 223

Grcevich J., Putman M. E., 2009, ApJ, 696, 385

Grogin N. A., et al., 2011, ApJS, 197, 35

Gullieuszik M., et al., 2020, ApJ, 899, 13

Gunn J. E., Gott J. Richard I., 1972, ApJ, 176, 1

Guo Q., White S., Li C., Boylan-Kolchin M., 2010, MNRAS, 404, 1111

Guo Y., et al., 2013, ApJS, 207, 24

Guo Y., et al., 2017, ApJ, 841, L22

Haines C. P., Gargiulo A., Merluzzi P., 2008, MNRAS, 385, 1201

Hamilton D., 1985, ApJ, 297, 371

Hayashi M., et al., 2018, ApJ, 856, 118

Henriques B. M. B., White S. D. M., Thomas P. A., Angulo R. E., Guo Q., Lemson G., Wang W., 2017, MNRAS, 469, 2626

Hirschmann M., De Lucia G., Wilman D., Weinmann S., Iovino A., Cucciati O., Zibetti S., Villalobos Á., 2014, MNRAS, 444, 2938

Hook I. M., Jørgensen I., Allington-Smith J. R., Davies R. L., Metcalfe N., Murowinski R. G., Crampton D., 2004, PASP, 116, 425

Hopkins P. F., Hernquist L., Cox T. J., Di Matteo T., Martini P., Robertson B., Springel V., 2005, ApJ, 630, 705

Hopkins P. F., Hernquist L., Cox T. J., Di Matteo T., Robertson B., Springel V., 2006, ApJS, 163, 1

Hou A., Parker L. C., Harris W. E., 2014, MNRAS, 442, 406

Hunter J. D., 2007, Computing in Science & Engineering, 9, 90

Ibata R. A., et al., 2013, Nature, 493, 62

Ji Z., Giavalisco M., Williams C. C., Faber S. M., Ferguson H. C., Guo Y., Liu T., Lee B., 2018, ApJ, 862, 135

Just D. W., et al., 2019, ApJ, 885, 6

Kaisin S. S., Karachentsev I. D., 2013, Astrophysics, 56, 305

Karachentsev I. D., Makarov D. I., Kaisina E. I., 2013, AJ, 145, 101

Kauffmann G., et al., 2003, MNRAS, 341, 33

Kawata D., Mulchaey J. S., 2008, ApJ, 672, L103

Kawinwanichakij L., et al., 2014, ApJ, 792, 103

Kimm T., et al., 2009, MNRAS, 394, 1131

Koekemoer A. M., et al., 2011, ApJS, 197, 36

Kriek M., van Dokkum P. G., Labbé I., Franx M., Illingworth G. D., Marchesini D., Quadri R. F., 2009, ApJ, 700, 221

Kukstas E., et al., 2023, MNRAS, 518, 4782

Lagos C. d. P., Lacey C. G., Baugh C. M., 2013, MNRAS, 436, 1787

Larson R. B., Tinsley B. M., Caldwell C. N., 1980, ApJ, 237, 692

Lavery R. J., Henry J. P., 1988, ApJ, 330, 596

Lee-Brown D. B., et al., 2017, ApJ, 844, 43

Lemaux B. C., et al., 2019, MNRAS, 490, 1231

Luber N., et al., 2022, ApJ, 927, 39

Makino J., Hut P., 1997, ApJ, 481, 83

Maller A. H., Berlind A. A., Blanton M. R., Hogg D. W., 2009, ApJ, 691, 394

Mamon G. A., Biviano A., Boué G., 2013, MNRAS, 429, 3079

Mao Y.-Y., Geha M., Wechsler R. H., Weiner B., Tollerud E. J., Nadler E. O., Kallivayalil N., 2020, arXiv e-prints, p. arXiv:2008.12783

Mao Z., Kodama T., Pérez-Martínez J. M., Suzuki T. L., Yamamoto N., Adachi K., 2022, A&A, 666, A141

Maraston C., 2005, MNRAS, 362, 799

Marinacci F., et al., 2018, MNRAS, 480, 5113

Marsan Z. C., et al., 2022, ApJ, 924, 25

Mastropietro C., Moore B., Mayer L., Debattista V. P., Piffaretti R., Stadel J., 2005, MNRAS, 364, 607

Matharu J., et al., 2021, ApJ, 923, 222

Mayer L., Kazantzidis S., Mastropietro C., Wadsley J., 2007, Nature, 445, 738

McConachie I., et al., 2021, arXiv e-prints, p. arXiv:2109.07696

McGee S. L., Balogh M. L., Bower R. G., Font A. S., McCarthy I. G., 2009, MNRAS, 400, 937

McGee S. L., Bower R. G., Balogh M. L., 2014, MNRAS, 442, L105

McNab K., et al., 2021, MNRAS, 508, 157

Mendez A. J., Coil A. L., Lotz J., Salim S., Moustakas J., Simard L., 2011, ApJ, 736, 110

Merluzzi P., et al., 2013, MNRAS, 429, 1747

Merritt D., 1983, ApJ, 264, 24

Mok A., et al., 2013, MNRAS, 431, 1090

Mok A., et al., 2014, MNRAS, 438, 3070

Moore B., Katz N., Lake G., Dressler A., Oemler A., 1996, Nature, 379, 613

Moore B., Lake G., Katz N., 1998, ApJ, 495, 139

Moore B., Lake G., Quinn T., Stadel J., 1999, MNRAS, 304, 465

Moretti A., et al., 2018, MNRAS, 475, 4055

Moretti A., et al., 2022, ApJ, 925, 4

Muzzin A., et al., 2009, ApJ, 698, 1934

Muzzin A., et al., 2012, ApJ, 746, 188

Muzzin A., et al., 2013a, ApJS, 206, 8

Muzzin A., et al., 2013b, ApJ, 777, 18

Muzzin A., et al., 2014, ApJ, 796, 65

Naiman J. P., et al., 2018a, MNRAS, 477, 1206

Naiman J. P., et al., 2018b, MNRAS, 477, 1206

Nantais J. B., et al., 2017, MNRAS, 465, L104

Nayyeri H., et al., 2017, ApJS, 228, 7

Nelson D., et al., 2018, MNRAS, 475, 624

Nelson D., et al., 2019, Computational Astrophysics and Cosmology, 6, 2

Nierenberg A. M., Auger M. W., Treu T., Marshall P. J., Fassnacht C. D., 2011, ApJ, 731, 44

Nierenberg A. M., Auger M. W., Treu T., Marshall P. J., Fassnacht C. D., Busha M. T., 2012, ApJ, 752, 99

Noble A. G., et al., 2017, ApJ, 842, L21

Noble A. G., et al., 2019, ApJ, 870, 56

Noirot G., et al., 2022, MNRAS, 512, 3566

Oemler Augustus J., 1974, ApJ, 194, 1

Oke J. B., Gunn J. E., 1983, ApJ, 266, 713

Oman K. A., Bahé Y. M., Healy J., Hess K. M., Hudson M. J., Verheijen M. A. W., 2021, MNRAS, 501, 5073

Omand C. M. B., Balogh M. L., Poggianti B. M., 2014, MNRAS, 440, 843

Oppenheimer B. D., Davé R., 2006, MNRAS, 373, 1265

Paccagnella A., et al., 2017, ApJ, 838, 148

Paccagnella A., Vulcani B., Poggianti B. M., Moretti A., Fritz J., Gullieuszik M., Fasano G., 2019, MNRAS, 482, 881

Pallero D., Gómez F. A., Padilla N. D., Torres-Flores S., Demarco R., Cerulo P., Olave-Rojas D., 2019, MNRAS, 488, 847

Park M., et al., 2022, MNRAS, 515, 213

Patel S. G., Holden B. P., Kelson D. D., Illingworth G. D., Franx M., 2009, ApJ, 705, L67

Pawlowski M. S., Kroupa P., 2020, MNRAS, 491, 3042

Pedregosa F., et al., 2011, Journal of Machine Learning Research, 12, 2825

Peng Y.-j., et al., 2010, ApJ, 721, 193

Peng Y.-j., Lilly S. J., Renzini A., Carollo M., 2012, ApJ, 757, 4

Pérez F., Granger B. E., 2007, Computing in Science and Engineering, 9, 21

Pillepich A., et al., 2018, MNRAS, 475, 648

Pintos-Castro I., Yee H. K. C., Muzzin A., Old L., Wilson G., 2019, ApJ, 876, 40

Poggianti B. M., et al., 2017, ApJ, 844, 48

Poggianti B. M., et al., 2019, MNRAS, 482, 4466

Popping G., Behroozi P. S., Peeples M. S., 2015, MNRAS, 449, 477

Reeves A. M. M., et al., 2021, MNRAS, 506, 3364

Reeves A. M. M., Hudson M. J., Oman K. A., 2023, MNRAS, 522, 1779

Rodriguez Wimberly M. K., Cooper M. C., Fillingham S. P., Boylan-Kolchin M., Bullock J. S., Garrison-Kimmel S., 2019a, MNRAS, 483, 4031

Rodriguez Wimberly M. K., Cooper M. C., Fillingham S. P., Boylan-Kolchin M., Bullock J. S., Garrison-Kimmel S., 2019b, MNRAS, 483, 4031

Rowlands K., et al., 2018, MNRAS, 473, 1168

Rudnick G., et al., 2017, ApJ, 849, 27

Saintonge A., et al., 2011, MNRAS, 415, 61

Salerno J. M., Muriel H., Coenda V., Cora S. A., Pereyra L., Ruiz A. N., Vega-Martínez C. A., 2022, MNRAS, 517, 4515

Salim S., et al., 2009, ApJ, 700, 161

Santini P., et al., 2015, ApJ, 801, 97

Sarron F., Conselice C. J., 2021, MNRAS, 506, 2136

Sarron F., Adami C., Durret F., Laigle C., 2019, A&A, 632, A49

Schawinski K., et al., 2014, MNRAS, 440, 889

Schiminovich D., et al., 2007, ApJS, 173, 315

Schlegel D. J., Finkbeiner D. P., Davis M., 1998, ApJ, 500, 525

Sengupta A., Keel W. C., Morrison G., Windhorst R. A., Miller N., Smith B., 2022, ApJS, 258, 32

Shi K., Toshikawa J., Lee K.-S., Wang T., Cai Z., Fang T., 2021, ApJ, 911, 46

Simpson C. M., Grand R. J. J., Gómez F. A., Marinacci F., Pakmor R., Springel V., Campbell D. J. R., Frenk C. S., 2018, MNRAS, 478, 548

Smethurst R. J., et al., 2018, MNRAS, 473, 2679

Socolovsky M., Maltby D. T., Hatch N. A., Almaini O., Wild V., Hartley W. G., Simpson C., Rowlands K., 2019, MNRAS, 482, 1640

Speagle J. S., Steinhardt C. L., Capak P. L., Silverman J. D., 2014, ApJS, 214, 15

Spekkens K., Urbancic N., Mason B. S., Willman B., Aguirre J. E., 2014, ApJ, 795, L5

Springel V., White S. D. M., Tormen G., Kauffmann G., 2001, MNRAS, 328, 726

Springel V., Di Matteo T., Hernquist L., 2005, MNRAS, 361, 776

Springel V., et al., 2018, MNRAS, 475, 676

Stalder B., et al., 2013, ApJ, 763, 93

Stefanon M., et al., 2017, ApJS, 229, 32

Sunyaev R. A., Zeldovich Y. B., 1970, Ap&SS, 7, 3

Tacchella S., et al., 2015, Science, 348, 314

Tacchella S., et al., 2022, ApJ, 926, 134

Tacconi L. J., et al., 2010, Nature, 463, 781

Tacconi L. J., et al., 2013, ApJ, 768, 74

Tacconi L. J., et al., 2018, ApJ, 853, 179

Tal T., van Dokkum P. G., Franx M., Leja J., Wake D. A., Whitaker K. E., 2013, ApJ, 769, 31

Tinker J. L., Wetzel A. R., 2010, ApJ, 719, 88

Tollerud E. J., Boylan-Kolchin M., Barton E. J., Bullock J. S., Trinh C. Q., 2011, ApJ, 738, 102

Tonnesen S., Bryan G. L., van Gorkom J. H., 2007, ApJ, 671, 1434

Valentino F., et al., 2020, ApJ, 889, 93

Van Der Walt S., Colbert S. C., Varoquaux G., 2011, Computing in Science & Engineering, 13, 22

Vázquez-Mata J. A., et al., 2020, MNRAS, 499, 631

Virtanen P., et al., 2020, Nature Methods, 17, 261

Vulcani B., Poggianti B. M., Fritz J., Fasano G., Moretti A., Calvi R., Paccagnella A., 2015, ApJ, 798, 52

Vulcani B., et al., 2017, ApJ, 837, 126

Vulcani B., et al., 2018, ApJ, 866, L25

Vulcani B., et al., 2020a, ApJ, 892, 146

Vulcani B., et al., 2020b, ApJ, 899, 98

Wang W., Sales L. V., Henriques B. M. B., White S. D. M., 2014, MNRAS, 442, 1363

Webb K., et al., 2020, MNRAS, 498, 5317

Weinmann S. M., Lisker T., Guo Q., Meyer H. T., Janz J., 2011, MNRAS, 416, 1197

Weinmann S. M., Pasquali A., Oppenheimer B. D., Finlator K., Mendel J. T., Crain R. A., Macciò A. V., 2012, MNRAS, 426, 2797

Weisz D. R., Dolphin A. E., Skillman E. D., Holtzman J., Gilbert K. M., Dalcanton J. J., Williams B. F., 2014a, ApJ, 789, 147

Weisz D. R., Dolphin A. E., Skillman E. D., Holtzman J., Gilbert K. M., Dalcanton J. J., Williams B. F., 2014b, ApJ, 789, 148

Weisz D. R., Dolphin A. E., Skillman E. D., Holtzman J., Gilbert K. M., Dalcanton J. J., Williams B. F., 2015, ApJ, 804, 136

Werner S. V., Hatch N. A., Muzzin A., van der Burg R. F. J., Balogh M. L., Rudnick G., Wilson G., 2022, MNRAS, 510, 674

Wetzel A. R., Tinker J. L., Conroy C., van den Bosch F. C., 2013, MNRAS, 432, 336

Wetzel A. R., Tinker J. L., Conroy C., van den Bosch F. C., 2014, MNRAS, 439, 2687

Wetzel A. R., Tollerud E. J., Weisz D. R., 2015, ApJ, 808, L27

Wheeler C., Phillips J. I., Cooper M. C., Boylan-Kolchin M., Bullock J. S., 2014, MNRAS, 442, 1396

Whitaker K. E., et al., 2011, ApJ, 735, 86

Wild V., Walcher C. J., Johansson P. H., Tresse L., Charlot S., Pollo A., Le Fèvre O., de Ravel L., 2009, MNRAS, 395, 144

Wild V., Almaini O., Dunlop J., Simpson C., Rowlands K., Bowler R., Maltby D., McLure R., 2016, MNRAS, 463, 832

Wild V., et al., 2020, MNRAS, 494, 529

Williams R. J., Quadri R. F., Franx M., van Dokkum P., Labbé I., 2009, ApJ, 691, 1879

Williams C. C., et al., 2022, arXiv e-prints, p. arXiv:2201.01304

Wilson G., et al., 2009, ApJ, 698, 1943

Woo J., et al., 2013, MNRAS, 428, 3306

Wright R. J., Lagos C. d. P., Davies L. J. M., Power C., Trayford J. W., Wong O. I., 2019, MNRAS, 487, 3740

Xie L., De Lucia G., Hirschmann M., Fontanot F., 2020, MNRAS, 498, 4327

Yagi M., Komiyama Y., Yoshida M., Furusawa H., Kashikawa N., Koyama Y., Okamura S., 2007, ApJ, 660, 1209

Yan R., Newman J. A., Faber S. M., Konidaris N., Koo D., Davis M., 2006, ApJ, 648, 281

Yang X., Mo H. J., van den Bosch F. C., Pasquali A., Li C., Barden M., 2007, ApJ, 671, 153

Yang X., Mo H. J., van den Bosch F. C., 2008, ApJ, 676, 248

Yang X., Mo H. J., van den Bosch F. C., 2009, ApJ, 695, 900

York D. G., et al., 2000, AJ, 120, 1579

Zhang H., Zaritsky D., Behroozi P., Werk J., 2019, ApJ, 880, 28

van den Bosch F. C., Aquino D., Yang X., Mo H. J., Pasquali A., McIntosh D. H., Weinmann S. M., Kang X., 2008, MNRAS, 387, 79

van der Burg R. F. J., et al., 2013, A&A, 557, A15

van der Burg R. F. J., et al., 2020, A&A, 638, A112

Appendix A

Appendix Title

A.1 Quenched Fractions including Additional Pre-Processing

In Fig. A.1 and Fig. A.2, we illustrate the results from our modified quenching model that incorporates additional pre-processing.

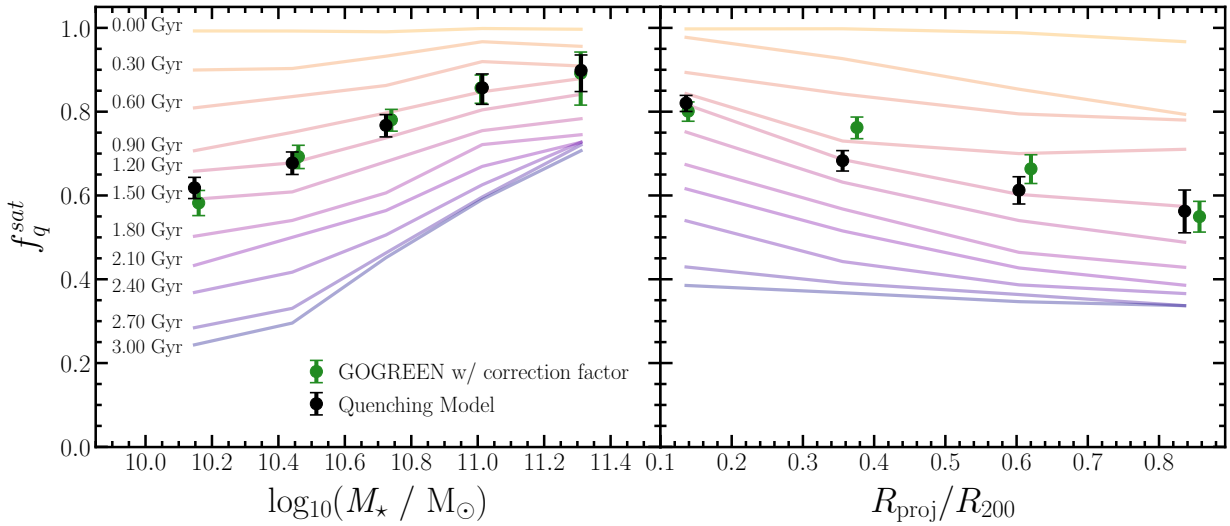

Figure A.1: Satellite quenched fraction as a function of satellite stellar mass (*left*) and projected cluster-centric distance normalized by R_{200} (*right*). Unlike Fig. 3.4, the results illustrated here are obtained using a modification to our fiducial quenching model designed to incorporate the effects of additional pre-processing. As before, the green circles illustrate the GOGREEN quenched fraction results with the membership correction factor applied. The colored translucent profiles in the background represent the TNG quenched fraction results using a constant quenching timescale ranging from 0 to 3 Gyr. The black circles represent the TNG results fit to the GOGREEN quenched fraction results. The observed quenched fraction as a function of stellar mass and cluster-centric radius are reproduced by a model assuming a mass-dependent quenching timescale, however, unlike the fiducial model it is clear that this modified model can reproduce both results by simply assuming a constant quenching timescale. All error bars represent 1-σ binomial uncertainties.

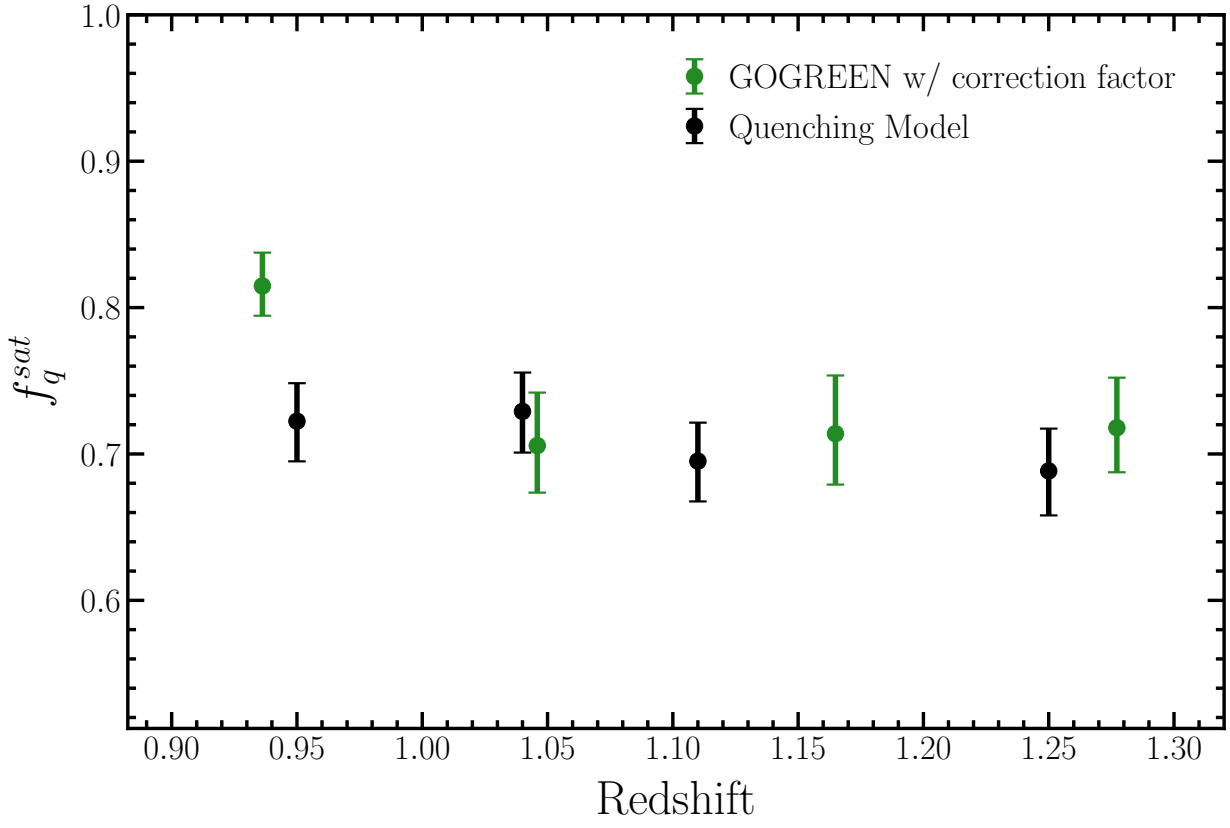

Figure A.2: Satellite quenched fraction versus redshift. Unlike Fig. 3.5, the results illustrated here are obtained using a modification to our fiducial quenching model designed to incorporate the effects of additional pre-processing. The green circles represent the observed results with the membership correction applied. The black circles shows the corresponding measurements for our modified fiducial model based on tuning $\tau_{\rm quench}(M_\star)$ to reproduce the observed satellite quenched fraction as a function of stellar mass. For both the observed and simulated samples, the uncertainties correspond to 1-σ binomial errors. Our modified quenching model that incorporates additional pre-processing is also able to successfully reproduce the observed GOGREEN satellite quenched fraction as a function of stellar mass, projected cluster-centric radius, and redshift.